UNIVERSITY OF READING

Department of Meteorology

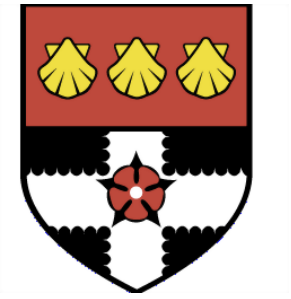

Atlantic transports from free model runs, reanalyses and coupled simulations

Davi Mignac

A thesis submitted for the degree of Doctor of Philosophy

November 2019

DECLARATION

I confirm that this is my own work and the use of all material from other sources has been properly and fully acknowledged.

D. Mignac

Acknowledgements

I would like to express my sincere gratitude to my supervisors, Keith Haines and David Ferreira, for their continuous support and guidance throughout my PhD. Their expertise and excitement with my research made me feel always positive and confident about my PhD. I am also very grateful for their trust on my work, even in research projects other than my PhD that I had the pleasure to collaborate. I would also like to thank my monitoring committee members, Jonathan Gregory and Thorwald Stein, for monitoring my progress twice a year and giving valuable suggestions to my research. I would like to thank my sponsor in Brazil, CAPES. This PhD would have been extremely difficult without the financial support from CAPES. I felt honored to be a Brazilian researcher doing my PhD abroad and to have all the support from my country.

I would like to thank members of the Meteorology department, especially the PhD students, who have made Reading a great place to be over the past 4 years. Thanks to my office mates in Harry Pitt 179 and in the Meteorology building 2U07, Helene, Ying Ying, Will, Tom, Michael and Mark for sharing great experiences and for all the memorable PhD trips that I will never forget. I really value our friendship and I hope to visit each of you soon. Thanks to my housemates, Pippo, Ludo and Renato for all the amazing support. You are like brothers to me.

I would like to thank my girlfriend, Emily, and her family for all the love and support. Living abroad is not easy but you always made me feel welcome and I really appreciate all the care and love. You are my family in the UK and thanks for always looking after me. I love all of you.

I would like to express how lucky I am to have such a great family in Brazil. Thanks to my parents, Lilian and Manuel, for all the love and unconditional support. You are everything to me and I miss you every day. Thanks to my grandmother, Berenice, for being such an inspiration to me. Thanks to my deceased grandfather, Alfredo, for making me become the person I am today. This doctoral thesis is dedicated to him.

Abstract

The Atlantic Meridional Overturning Circulation (AMOC) is a key contributor in the climate system, transporting warm waters northwards throughout the Atlantic to compensate for the southward export of cold North Atlantic deep waters. However, observing the AMOC is inherently challenging due its long timescales and large spatial extent, which requires the use of time-evolving, three-dimensional model products to assess the ocean circulation, including: free-running models (FRMs), ocean reanalyses (ORAs) and coupled climate simulations.

In the first and second chapters of this thesis, we show that the present ocean observation network and data assimilation schemes can be used to consistently constrain the ORA interior circulation in both structure and strength throughout the South Atlantic, which is improved with respect to the FRMs. This is in striking contrast with the large disagreement found in the ORA AMOCs, which is traced back to transport discrepancies in the South Atlantic western boundary currents at both upper and deep levels, explaining up to 85% of the ORA spread in the meridional heat transports. This will likely limit the effectiveness of ORAs for climate or decadal prediction studies.

Using the same FRMs and ORAs with realistic salinities but quite different AMOCs, we show in the third chapter that the fresh Antarctic Intermediate Water layer eliminates salinity differences across the AMOC branches at ∼1200 m, which decouples the overturning freshwater transport F_{ov} from the AMOC south of ∼10°N. In the South Atlantic the 0-300 m zonal salinity contrasts control the gyre freshwater transports F_{gyre}, which also determine the total freshwater transports. This decoupling makes the southern F_{ov} unlikely to play any role in AMOC stability, leaving indirect F_{gyre} feedbacks or F_{ov} in the north, as more relevant factors.

In the fourth chapter of this thesis, the internal variability of 10 pre-industrial coupled simulations are used to show that coupled climate systems are governed by different dynamics and contain feedbacks not captured by the box-models. The spatio-

temporal variability of the Atlantic freshwater budgets reveals that the influence of F_{ov} at 34°S in explaining freshwater content (FWC) changes is restricted to the South Atlantic and is always smaller than the influence of F_{gyre} at 34°S. This consistently refutes the main salt-advection feedback mechanism, which states that F_{ov} at 34°S is the main driver of meridional FWC perturbations.

These results represent a substantial step in improving the understanding of the AMOC stability and have an important impact on climate modelling, since FRMs, ORAs and climate models refute box-model theories of AMOC bi-stability and suggest that other climate feedbacks associated with F_{gyre} and the atmosphere will likely dominate those associated with F_{ov} throughout the South Atlantic.

CONTENTS

LIST OF FIGURES

LIST OF TABLES

NOMENCLATURE

$AAIW$	Antarctic Intermediate Water
AC	Agulhas Current
ACC	Antarctic Circumpolar Current
AM	Atmospheric Model
$AMOC$	Atlantic Meridional Overturning Circulation
BC	Brazil Current
BeC	Benguela Current
CAM	Community Atmosphere Model
$CGLORS$	Global Ocean Reanalysis System
$CICE$	Los Alamos Sea Ice Model
$CMCC$	Centro Euro-Mediterraneo sui Cambiamenti Climatici
$CMIP5$	Coupled Model Intercomparison Project 5
$CORE$	Coordinated Ocean Research Experiments

DA	Data Assimilation
$DWBC$	Deep Western Boundary Current
$ECHAM$	European Centre Hamburg Atmospheric Model
$ECMWF$	European Centre for Medium-Range Weather Forecasts
EKE	Eddy Kinetic Energy
EUC	Equatorial Undercurrent
FRM	Free-Running Model
FWC	Freshwater Content
$GLORYS$	Global Ocean Reanalysis and Simulation
$GloSea$	Global Seasonal Forecast System Reanalysis
GM	Gent-McWilliams parameterization
$GOLD$	Generalized Ocean Layered Dynamics
$ITCZ$	Intertropical Convergence Zone
$IWBC$	Intermediate Western Boundary Current
LIM	Louvain-la-Neuve Sea Ice Model
MC	Malvinas Current
MDT	Mean Dynamical Topography
MHT	Meridional Heat Transport
MOC	Meridional Overturning Circulation
MOM	Modular Ocean Model

MW	Mediterranean Water
$NADW$	North Atlantic Deep Water
$NASG$	North Atlantic Subtropical Gyre
NBC	North Brazil Current
$NBUC$	North Brazil Undercurrent
$NEMO$	Nucleus for European Modelling of the Oceans
ORA	Ocean Reanalysis
$ORAP5$	Ocean Reanalysis Pilot 5
$OSCAR$	Ocean Surface Current Analyses Real-time
$OSNAP$	Overturning in the Subpolar North Atlantic Program
$OSSE$	Observation System Simulation Experiment
POP	Parallel Ocean Program
$RAPID$	Rapid Climate Change Array
SAC	South Atlantic Current
$SACW$	South Atlantic Central Water
$SAMBA$	South Atlantic Meridional Overturning Basin-Wide Array
$SAMOC$	South Atlantic Meridional Overturning Circulation
$SASG$	South Atlantic Subtropical Gyre
SEC	South Equatorial Current
$SEUC$	South Equatorial Undercurrent

SIC	Sea Ice Concentration
SLA	Sea Level Anomaly
SSH	Sea Surface Height
SSS	Sea Surface Salinity
SST	Sea Surface Temperature
STC	Subtropical Cell
TW	Tropical Water
$UR025$	University of Reading Reanalysis
WOA	World Ocean Atlas
XBT	eXpendable BathyThermograph

CHAPTER 1

INTRODUCTION

This introductory chapter reviews the current state of the literature about the Atlantic Meridional Overturning Circulation (AMOC) and sets the motivations for the thesis questions and goals. The literature review includes discussions about the ocean circulation and its role in climate in Section 1.1. The observations and modelling approaches to assess the AMOC are discussed in Section 1.2. Time variability and mechanisms involved in the AMOC transports are addressed in Section 1.3. A focus on the South Atlantic circulation is given in Section 1.4, and discussions about the AMOC stability are addressed in Section 1.5. After contextualising the relevant scientific topics of this research, the thesis goals and outline are presented in Section 1.6 and 1.7, respectively.

1.1 Ocean circulation and its role on the climate

The ultimate source of energy that drives the climate system is the radiation from the Sun. Approximately 30% of the incoming solar radiation is immediately reflected back into space by clouds, the atmosphere, and the Earth's surface; about 20% is directly absorbed by the atmosphere and the final 50% warms the Earth's surface: the land and the ocean (*Kiehl and Trenberth*, 1997). However, the Sun's energy is

distributed unevenly over the Earth's surface, with equatorial areas receiving more solar energy and absorbing more heat than areas near the poles. Both ocean currents and atmospheric circulations act to balance this unequal heat absorption by the Earth's surface, transporting heat from the equator to higher latitudes (*Clarke et al.*, 2001). As well as the ocean's ability to transport heat and freshwater over a wide range of time and space scales, it is also able to store and release significant amounts of heat over long periods of time without a large increase in its temperature. A simple indication of this is the fact that 3 m of seawater has roughly the same heat capacity as the whole atmospheric column above it (*Gill*, 1982), which gives the ocean a central role in moderating Earth's climate.

The ocean circulation is driven by air-sea fluxes of momentum, heat and freshwater. The resulting circulation is thus intimately coupled to the atmosphere. For example, as the winds blow above the ocean's surface, the near surface ocean layer moves as a result of the combined effect of wind frictional forces transferring momentum, and the Coriolis force, leading to an Ekman transport. This mechanism drives a net transport of water that is perpendicular to the wind (to the right in the northern Hemisphere and left in the southern Hemisphere), a pattern by which the major ocean gyres are developed (*Ekman*, 1905). As surface waters are displaced meridionally, the Ekman transport results in areas of convergence and divergence that lead, respectively, to: downwelling (i.e. sinking of surface waters) in the center of subtropical gyres and upwelling (i.e. upward motion of interior waters) in the center of subpolar gyres. The water moving meridionally in the gyres also circulates back to its initial latitude within narrow and intense western boundary currents, characterized by baroclinic jets carrying warm waters to higher latitudes (*Sverdrup*, 1947).

Superimposed on the shallow wind-driven circulation, a much deeper ocean circulation acts on longer timescales. This component of the circulation is sometimes referred to as thermohaline circulation, due to its dependence on changes in temperature and salinity, both of which regulate the buoyancy of water parcels (*Clarke et al.*, 2001).

When a water parcel cools or becomes saltier, its density increases resulting in a buoyancy loss and favoring its sinking to greater depths. Buoyancy loss occurs primarily at polar latitudes, where heat loss to the atmosphere and salt rejection from the sea ice formation lead to the sinking of cold, dense water masses (*Marshall and Schott*, 1999; *Kuhlbrodt et al.*, 2007). This deep convection of water masses links the surface and deep oceans, and sets the deep ocean properties. As these deep waters flow throughout the oceans, they gradually become less dense due to mixing with warmer waters from above and eventually return to the surface in wind-driven and mixing upwelling regions (*Kuhlbrodt et al.*, 2007). With respect to the wind-driven regions, the strong westerly winds in the southern ocean are argued to play a key role in enabling the upwelling of deep water masses (*Marshall and Speer*, 2012).

The combined effects of wind and density-driven ocean circulations develop the major pathways of a global meridional overturning circulation (MOC), characterized by a large-scale system of surface and deep currents transporting water, heat and salt all around the globe (Fig. 1.1; *Kuhlbrodt et al.*, 2007). The ocean basins show different MOC strengths and patterns, which are dependent on the deep water formation. For example, there is no deep water formation in the North Pacific as the sea surface salinity (SSS) is too low for sinking to occur (*Warren*, 1983). Therefore the Pacific Ocean is mainly ventilated from the south, while its MOC is primarily dominated by shallow wind-driven circulations (*Zhang and McPhaden*, 2006; *Ferreira et al.*, 2018; *Lee et al.*, 2019). Unlike the North Pacific, the MOC in the North Atlantic has two well-established convection sites in the Labrador and Nordic seas as a result of the North Atlantic's denser waters, explained by their larger SSSs (*Marshall and Schott*, 1999; *Straneo*, 2006). Therefore, the AMOC exports a dense and cold North Atlantic Deep Water (NADW) to the southern ocean, which is compensated by an upper warm branch flowing towards the northern Atlantic.

Due to the northward meridional heat transport (MHT) by the AMOC upper branch, the regions surrounding the subpolar North Atlantic have a warmer climate

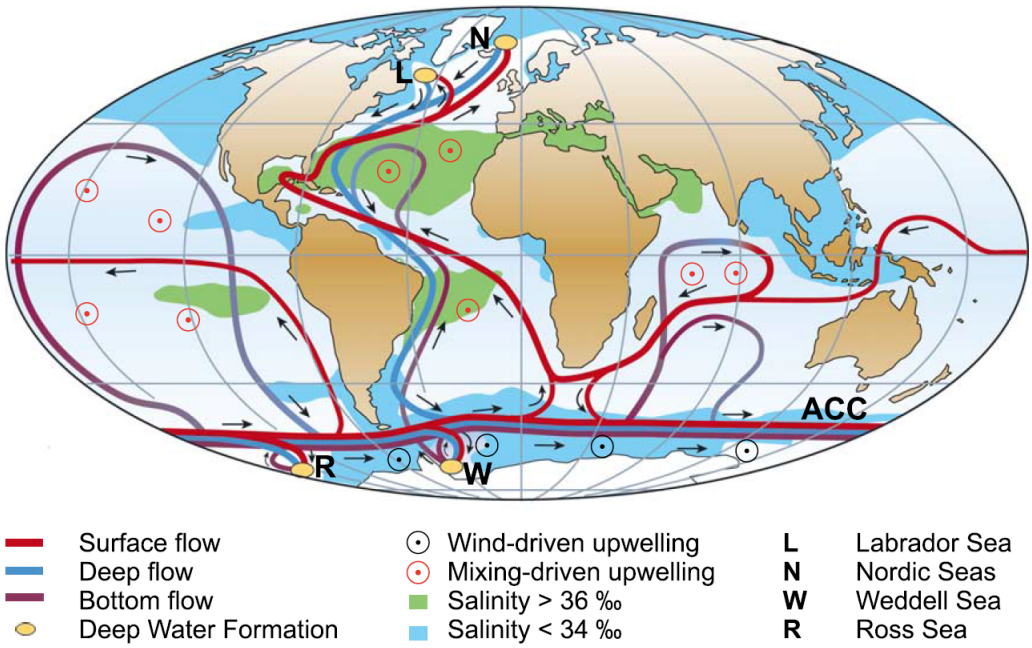

Figure 1.1: Simplified schematic of the Global MOC extracted from *Kuhlbrodt et al.* (2007). The arrows indicate the direction of the surface, deep and bottom flows. Green (blue) shaded areas represent saltier (fresher) surface waters. ACC corresponds to Antarctic Circumpolar Current.

than other regions at similar latitudes (*Clarke et al.*, 2001). For example, several modelling studies have shown that an AMOC slowdown can impact the climate on both regional and global scales. An AMOC weakening could lead to: a surface air temperature cooling of up to 8°C in the North Atlantic (e.g. *Vellinga and Wood*, 2002; *Laurian et al.*, 2009; *Jackson et al.*, 2015), a strengthening of the North Atlantic storm track (e.g. *Zappa et al.*, 2013; *Jackson et al.*, 2015), changes in precipitation patterns due to a southward shift of the Intertropical Convergence Zone (ITCZ), and weakened Indian and Asian summer monsoons (e.g. *Manabe and Stouffer*, 1993; *Zhang and Delworth*, 2005; *Broccoli et al.*, 2006).

Because of its role in transporting heat throughout the Atlantic, the AMOC decadal variations have been suggested to affect the low-frequency variability of the North Atlantic sea surface temperatures (SSTs), influencing the decadal SST warming/cooling cycles defined as the Atlantic Multidecadal Variability (*Latif et al.*, 2003; *Knight et al.*,

2005; *Delworth et al.*, 2007). On much longer time scales, the AMOC-related ocean transport variations have also been invoked to play a key role in the anti-phase changes in the Antarctic and Arctic climates, known as the bipolar seesaw (*Broecker*, 1998; *Pedro et al.*, 2011), as well as in paleoclimate shifts (*Broecker*, 1998, 2003).

The sinking of NADW plays an important role in sequestering heat and anthropogenic carbon into the deep ocean and therefore the AMOC is suggested to be a key element in moderating climate changes (*Kostov et al.*, 2014). It has also been proposed that variations in the MOC and its subsequent impacts on ocean heat uptake may explain the 1998-2012 hiatus in global mean surface warming. This is argued to be related to the intensification of the shallow overturning cells in the Pacific (*Balmaseda et al.*, 2013b; *England et al.*, 2014), changes in the NADW formation rates and upwelling in the southern ocean (*Chen and Tung*, 2014; *Drijfhout et al.*, 2014).

1.2 Assessing the ocean circulation

Although the AMOC dynamics are extremely important for the Earth's climate, reflecting a complex interplay between wind and buoyancy driven flows, as well as eddies and mixing, they are not yet fully understood. According to *Buckley and Marshall* (2016), several AMOC topics still need to be better investigated, for example: the AMOC transports, their modes of variability and meridional coherence; the influence of meridional freshwater transports on the AMOC stability; and the relationship between interior pathways, boundary currents and the AMOC. Addressing these issues becomes even harder since observing the AMOC is inherently challenging due its long timescales and large spatial extent. This situation has been improved with the implementation of trans-basin observing systems, such as: the Rapid Climate Change (RAPID) array at 26.5°N in the Atlantic, since 2004 (*Cunningham et al.*, 2007); the South Atlantic Meridional Overturning Basin-Wide Array (SAMBA) at 35°S deployed in 2014 (*Ansorge et al.*, 2014); and the Overturning in the Subpolar North Atlantic

Program (OSNAP) array at ∼60°N, also launched in 2014 (*Lozier et al.*, 2019). Although these overturning arrays are able to continuously measure AMOC transports, they are too sparse and have only 15 years of observational records so far.

Model products, such as free-running models (FRMs), ocean reanalyses (ORAs) and coupled climate simulations are now commonly used to investigate the AMOC in conjunction with the overturning arrays, since they provide complete, time-evolving descriptions of the three-dimensional ocean circulation. The FRMs are defined here as historical ocean model runs forced with observational estimates of atmospheric forcing, typically from atmospheric reanalyses. Compared to the FRMs, the ORAs additionally employ data assimilation (DA) methods to constrain the ocean model with historical ocean observations (*Balmaseda et al.*, 2015). Generally, the observational data consist of temperature and salinity profiles of the ocean (e.g. Argo floats) in combination with sea level (e.g. from satellite altimeters), sea surface temperature and sea ice concentration (e.g. from satellite microwave radiometers). In the ORAs, atmospheric forcing combined with DA dynamically extrapolates the observational information into regions lacking observations. This makes ocean reanalyses potentially useful products to assess the transports and change indicators, particularly in regions where the ocean still remains under-sampled and observational data correspond to short periods of limited coverage (e.g. *Zuo et al.*, 2011; *Masina et al.*, 2015; *Uotila et al.*, 2019).

ORAs have also been able to properly capture climate signals in the temporal evolution of the global ocean heat content, showing a dominant warming trend of the deep ocean (i.e. below 700 m) in the last two decades, which is consistent with observational estimates (*Balmaseda et al.*, 2013b). Similarly, *Palmer et al.* (2015) showed that many ORAs had consistent ocean heat content trends as a function of depth, including a consistent warming below 700 m. In terms of circulation, *Jackson et al.* (2016) showed, based on a single ORA result, that the 2004-2014 AMOC decline seen in the RAPID transports was actually a recovery from an earlier AMOC strengthening, regulated by the southward propagation of decadal density anomalies from the Labrador Sea. The

findings in *Jackson et al.* (2016) were based upon the ORA's ability to reproduce the interannual variability and decadal trends of the AMOC at 26.5°N, when compared to the observed RAPID transports, which were not assimilated (Fig. 1.2)

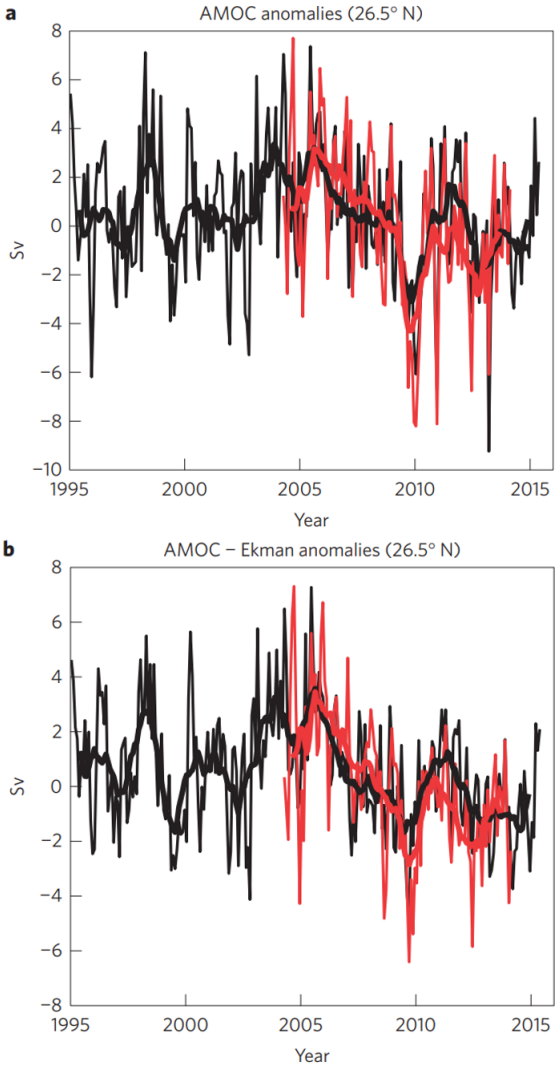

Figure 1.2: Time series of the (a) total AMOC transport anomalies (Sv) and (b) geostrophic AMOC transport anomalies (Sv) at 26.5°N, comparing GloSea5 product (black) with observations from the RAPID array (red). Extracted from *Jackson et al.* (2016).

Contrasting this with previous ORA studies, *Karspeck et al.* (2015) looked at long ORA simulations starting before 1960 and found a substantial disagreement in the ORA AMOCs within these early observation-sparse periods. ORA AMOC trends in *Karspeck*

et al. (2015) were less consistent with each other than those from corresponding FRMs, indicating that AMOC estimates could be sensitive to assimilation techniques. *Masina et al.* (2015) and *Palmer et al.* (2015) however show that ORAs are more likely to agree in more recent time periods, particularly after satellite measurements and Argo floats became available in 1992 and 2000, respectively.

In addition to FRMs and ORAs, the use of coupled climate models can provide AMOC time series over hundreds of years allowing investigation of the multidecadal variability and meridional coherence of the AMOC transports (e.g. *Danabasoglu*, 2008; *Danabasoglu et al.*, 2012; *Robson et al.*, 2012). Unlike ocean only experiments with FRMs and ORAs, these coupled models capture coupled feedbacks in the climate system, given their ocean-atmosphere mutual interactions (e.g. *Yin and Stouffer*, 2007; *Mecking et al.*, 2016). However, they are only constrained by observed (or projected) external forcing, which results in large mean state biases (*Jackson*, 2013; *Liu et al.*, 2017; *Mecking et al.*, 2017). Furthermore, due to very high computational costs of running long coupled simulations, these climate models currently have much lower horizontal and vertical resolutions than the FRMs and ORAs (*Taylor et al.*, 2012). These models also have difficulty in representing the depth of the AMOC and its mean strength, as the AMOC appears to be sensitive to model details, such as resolution, overflow parameterizations and parameterized mesoscale eddy fluxes. The maximum AMOC in coupled models can occur at latitudes between 20°N and 60°N, and ranging from 13 to 31 Sv (*Kostov et al.*, 2014). Even with these limitations, the new generation of coupled models has been extensively used to investigate potential feedbacks in the atmosphere and in the ocean, and how they influence AMOC transports on a range of timescales (*Yin and Stouffer*, 2007; *Mecking et al.*, 2016; *Liu et al.*, 2017; *Gent*, 2018).

1.3 AMOC variability and buoyancy anomalies

The nature of the AMOC variability strongly depends on the timescale. Both models and observations agree that the AMOC variability on intra-annual to internannual timescales is primarily the local response to wind variations, due to the Ekman component of the transports (*Hirschi et al.*, 2007; *Rayner et al.*, 2011; *Roberts et al.*, 2013). For example, ocean models driven by observed winds can reproduce almost 80% of the observed AMOC and heat transport variability by the RAPID array on intra-annual timescales (*Roberts et al.*, 2013), reinforcing the short response of the upper ocean stratification to wind changes.

From interannual to decadal timescales, the geostrophic component is argued to dominate the AMOC variability, reflecting the role played by the east-west density contrasts across the basin (*Hirschi et al.*, 2007; *Cabanes et al.*, 2008). Both observations (*Bryden et al.*, 2009), FRMs (*Buckley et al.*, 2012) and ORAs (*Cabanes et al.*, 2008) show that buoyancy anomalies along the western boundary have a larger contribution than those on the eastern boundary to determine the geostrophic variability of the AMOC in the North Atlantic. This is consistent with *Bingham and Hughes* (2009), who demonstrate that the interannual geostrophic AMOC variability in two ocean models could be largely reproduced using only local density changes on the western boundary slope. However, the observed transports by pilot boundary arrays at 35°S, prior to SAMBA array, show a dual influence of the buoyancy anomalies between the western and eastern boundaries, which have approximately equal contributions to the AMOC variability (*Meinen et al.*, 2013).

Since the AMOC-observing arrays are too sparse and so far are only approximately a decade long, the space and time evolving AMOC in ocean models are mainly used to investigate the connection of the AMOC anomalies throughout the basin. The meridional coherence of the AMOC is mainly driven by the wind field on intra-annual timescales (*Hirschi et al.*, 2007; *Cabanes et al.*, 2008; *Wunsch and Heimbach*, 2013).

However, on decadal and longer time-scales the models show increasing meridional coherence of their AMOCs and MHTs (*Knight et al.*, 2005; *Danabasoglu*, 2008; *Msadek and Frankignoul*, 2009; *Danabasoglu et al.*, 2012), which is likely to be driven by the meridional propagation of the buoyancy anomalies on the boundaries (*Böning et al.*, 2006; *Biastoch et al.*, 2008b; *Danabasoglu*, 2008; *Buckley et al.*, 2012; *Robson et al.*, 2012). Two possible approaches have been proposed for understanding the meridional propagation of buoyancy anomalies: through advection in the Deep Western Boundary Current (DWBC) or interior pathways slowing transporting buoyancy anomalies; or through the fast propagation of anomalies by boundary waves, which balance the Coriolis force against a topographic boundary, such as a coastline (*Johnson and Marshall*, 2002). The relative importance of advection and boundary wave propagation on the buoyancy (hence AMOC) anomalies at different latitudes is not robust across ocean models. In some models, significant time lags are found between the AMOC anomalies in the North Atlantic subpolar gyre and subtropical regions, suggesting a role of advection (e.g. *Zhang*, 2010; *Buckley et al.*, 2012; *Jackson et al.*, 2016), but other modelling studies show a communication of buoyancy anomalies via boundary waves (*Biastoch et al.*, 2008a).

Several mechanisms have been identified as contributing sources of northern buoyancy anomalies, for example: local atmospheric forcing and its influence on the SSTs (e.g. *Buckley et al.*, 2014); shifts in the Gulf Stream paths leading to large temperature anomalies along its front (e.g. *Joyce and Zhang*, 2015); changes in deep convection and water mass formation (e.g. *Zhang*, 2010); shifts in the salinity of the North Atlantic subpolar gyre due to its interaction with the wind forcing and the subtropical gyre (e.g. *Holliday*, 2003); and advection of buoyancy anomalies by the mean currents (e.g. *Cabanes et al.*, 2008; *Buckley et al.*, 2012).

AMOC anomalies in the North Atlantic may also originate in the South Atlantic as the circulation acts as a communicator between the southern and northern oceans (*Garzoli and Matano*, 2011). For example, employing a two-way nesting system with

an eddy-resolving ocean model in the Agulhas region, *Biastoch et al.* (2008a) found that the Agulhas leakage affects the decadal AMOC variability. This remote connection was explained by the following mechanism: low-frequency oscillations in the thermocline depth, induced by decadal variations of the Agulhas leakage regime, travel as Rossby waves across the South Atlantic and subsequently as coastal Kelvin waves along the western boundary into the North Atlantic. This is consistent with the advective transit time of 4-40 years, given by surface drifters and Lagrangian high-resolution model data, to travel from the Agulhas leakage to the northern Atlantic (*Sebille et al.*, 2011). The longest transit time trajectories were associated with convergence and subduction within the subtropical gyres.

Sebille et al. (2011) also show that almost all trajectories crossing the equatorial Atlantic are within the North Brazil Current (NBC), which originates in the tropical South Atlantic western boundary (*Silveira et al.*, 1994). Multidecadal NBC transport variability has been suggested to be a useful indicator of basin-scale AMOC variations (e.g. *Zhang et al.*, 2011; *Rühs et al.*, 2015). Using historical western boundary observations off the Brazilian coast and 700 years of a climate model simulation, *Zhang et al.* (2011) demonstrate that NBC variability influences Labrador Sea deep convection within a lag of a few years. The multidecadal NBC time series from *Zhang et al.* (2011) is also coherent with the Atlantic Multidecadal Oscillation SST patterns, which have already been linked to AMOC variations. The features of the South Atlantic circulation, including the NBC, are better described in the next Section.

1.4 South Atlantic MOC

As seen in Fig. 1.1, the South Atlantic MOC (SAMOC) is represented by an upper, warm branch flowing north towards the equator and a deep, cold branch flowing south towards the pole, resulting in a distinct net heat transport up the large-scale temperature gradient. Therefore, the Atlantic MHT is northward in both hemispheres,

rather than poleward as in the Indo-Pacific ocean (*Trenberth and Caron*, 2001), with important implications for the cross-equatorial global heat transports. For example, recent studies argue that Atlantic heat transports play a key role in setting the mean ITCZ position north of the equator (*Frierson et al.*, 2013; *Marshall et al.*, 2013), highlighted by Fig. 1.3. The hemispheric net radiative forcing of climate at the top of the atmosphere is nearly symmetric about the equator, thus the total (atmosphere plus ocean) equatorial heat transport is small, around 0.2 PW (*Trenberth and Caron*, 2001; *Marshall et al.*, 2013; *Voigt et al.*, 2013). However, due to the SAMOC, the global ocean carries more heat northwards across the equator, around 0.4 PW, than the coupled system does. First, this results in a southward equatorial atmospheric transport to compensate for the ocean heat transports, which displaces the mean ITCZ position north of the equator. Second, both the ocean and the atmosphere are slightly warmer (by $\sim$2°C) in the northern than in the southern hemisphere (*Feulner et al.*, 2013; *Marshall et al.*, 2013). As a result, the northern hemisphere emits slightly more outgoing longwave radiation than the southern hemisphere, supporting the small northward heat transport by the coupled system across the equator (*Marshall et al.*, 2013; *Kang et al.*, 2014).

Fig. 1.4 shows that the SAMOC upper branch is a complex mixture of waters originating from the Indian, Pacific and southern oceans. Observations (e.g. *Sloyan and Rintoul*, 2001) and models (e.g. *Garzoli and Matano*, 2011) demonstrate that the South Atlantic is an active conduit of water masses. *Garzoli and Matano* (2011) reveal that water mass transformations occur all across the basin, but are particularly strong in areas of high mesoscale variability, such as in the Agulhas leakage and in the confluence between the Brazil current (BC) and Malvinas current (MC). The water mass properties exported by the South Atlantic are argued to influence the long-term AMOC variability, particularly on decadal timescales through the heat and salt export by the Agulhas leakage (*Weijer et al.*, 2002; *Biastoch et al.*, 2008a; *Dong et al.*, 2011b; *Sebille et al.*, 2011).

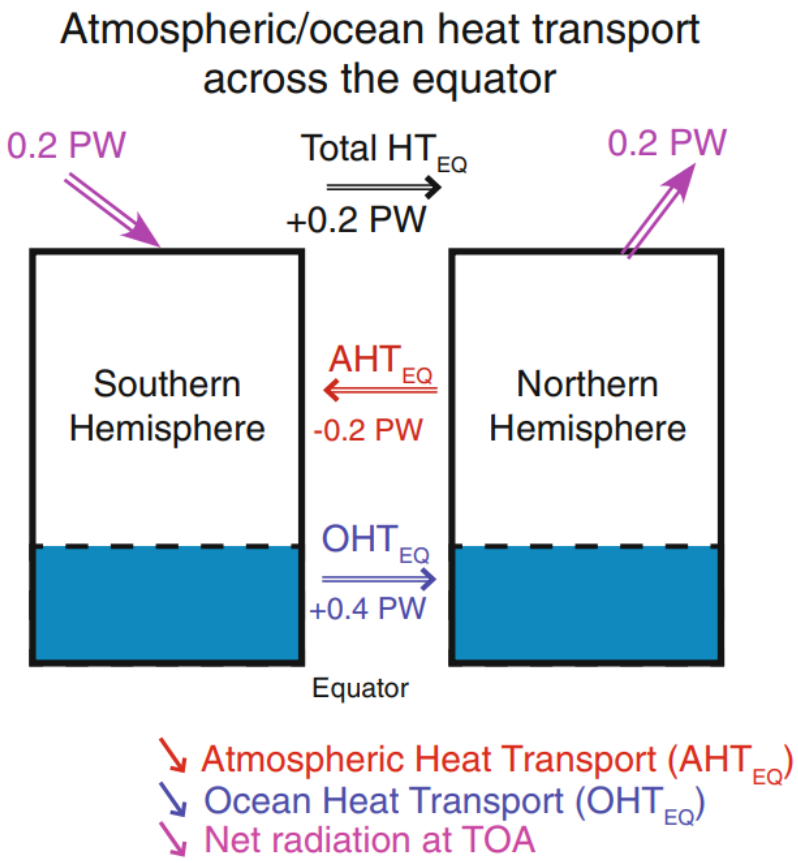

Figure 1.3: Schematic extracted from *Marshall et al.* (2013) showing the global heat transports (PW) across the equator. OHT_{EQ}, AHT_{EQ} and total HT_{EQ} are the ocean, atmospheric and total heat transports across the equator. The numbers are estimates obtained in *Marshall et al.* (2013) from observational reanalysis and satellite data.

The southern Atlantic is bordered by the Antarctic Circumpolar Current (ACC). According to *Gnanadesikan* (1999), *Kuhlbrodt et al.* (2007) and *Marshall and Speer* (2012), some of the NADW returns adiabatically to the surface along the ACC path where strong westerly winds enable the upwelling of deep water masses, therefore connecting the AMOC with the global ocean circulation (Fig. 1.1). ACC waters can migrate northward in the South Atlantic as soon as they leave the Drake Passage, developing the cold MC on the western boundary of the southern Atlantic (Fig. 1.4). MC transport variations have been linked to variations of the ACC transport in the Drake passage, as well as to wind stress forcing in the circumpolar region and to eddy

propagation from the South Pacific (*Vivier et al.*, 2001; *Spadone and Provost*, 2009).

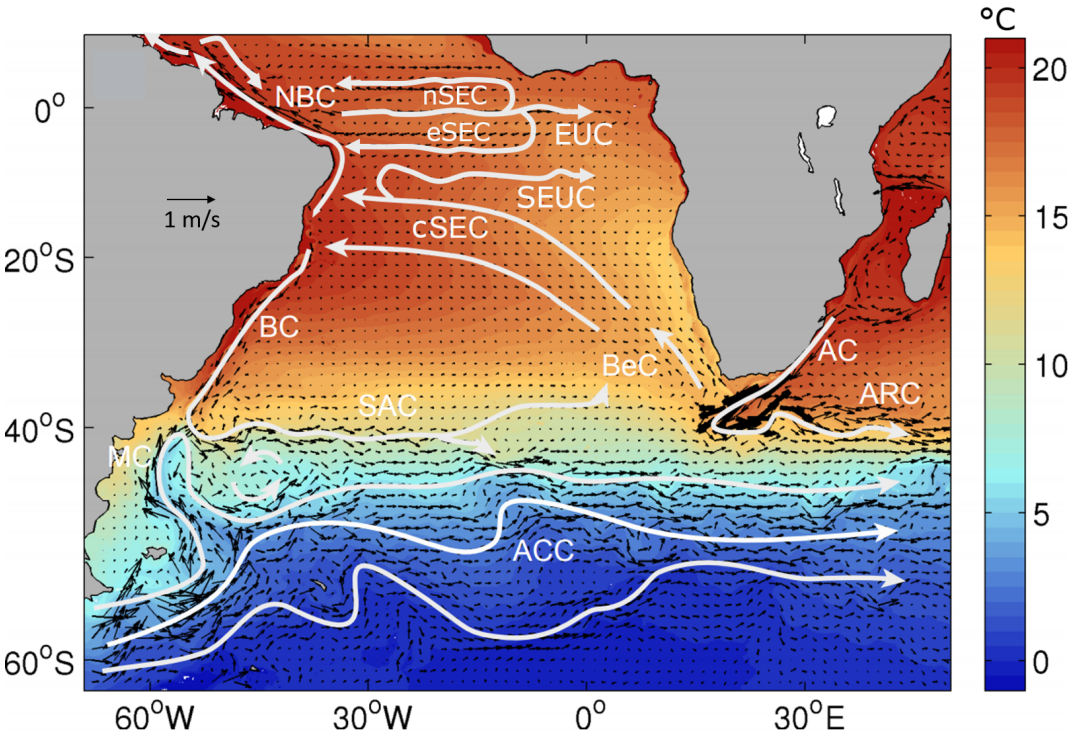

Figure 1.4: The near surface (0-500 m) South Atlantic circulation (m/s) and mean temperature (°C) given by the ORA GLORYS2V4 over 1997-2010. The schematic of the circulation with white arrows are adapted from *Peterson and Stramma* (1991) and *Stramma and Schott* (1999).

The encounter of the cold equatorward MC with the warm poleward BC at ∼40°S results in the Brazil-Malvinas confluence (Fig. 1.4), which is known to have large contrasts in temperature/salinity and a strong eddy activity (*Garzoli*, 1993; *Goni et al.*, 1996). Due to the Brazil-Malvinas confluence, the BC is deflected to the east developing the South Atlantic Current (SAC) at the southern limit of the subtropical gyre. The SAC interacts with the Benguela Current (BeC) and the Agulhas leakage on the eastern side of the basin. The latter results from the Agulhas Current (AC) and its Retroflection Current (ARC) releasing large columns (rings) of warm and salty water from the Indian ocean that drift into the South Atlantic (*Weijer et al.*, 2002). The Agulhas leakage fluctuations have been consistently linked to interannual-to-decadal

variability and trends of the modelled SAMOCs and MHTs (e.g. *Weijer et al.*, 2002; *Dong et al.*, 2011b; *Castellanos et al.*, 2017), as well as being considered a possible source of some of the northern AMOC decadal variability (e.g. *Biastoch et al.*, 2008a).

In Fig. 1.4 the central South Equatorial Current (cSEC) defines the northern limit of the South Atlantic subtropical gyre (SASG). The bifurcation of the cSEC close to the Brazilian coast results in the BC flowing poleward and the NBC flowing equatorward along the western boundary region (*Peterson and Stramma*, 1991). The latitude of the cSEC bifurcation varies from ∼17°S to ∼13°S throughout the year, associated with changes in the local wind stress due to the annual north-south ITCZ migration (*Rodrigues et al.*, 2006). The seasonal variability of the cSEC bifurcation position also contributes to the seasonal variability of both the BC and NBC. The NBC is stronger (weaker) when the SEC bifurcation is located at its southernmost (northernmost) position, and the other way round for the BC (*Peterson and Stramma*, 1991; *Stramma and Schott*, 1999; *Schott et al.*, 2005; *Rodrigues et al.*, 2006). The complex system of Atlantic equatorial currents also includes two additional westward SEC branches, the equatorial (eSEC) and the northern (nSEC), as well as the eastward Equatorial Undercurrent (EUC; *Urbano et al.*, 2008) and the South Equatorial Undercurrent (SEUC; *Molinari*, 1982).

Situated in the tropical Atlantic where equatorial currents are predominantly zonal (Fig. 1.4), the NBC is often invoked as a key element of the AMOC upper branch flow crossing the equator (*Schott et al.*, 2005; *Rabe et al.*, 2008; *Sebille et al.*, 2011; *Zhang et al.*, 2011; *Hummels et al.*, 2015; *Rühs et al.*, 2015). The low-frequency NBC transport variability has been considered to be a useful index of the AMOC variability in historical observations and coupled climate simulations (*Zhang et al.*, 2011), as well as in ocean reanalyses (*Rabe et al.*, 2008). In a set of hindcast, sensitivity and perturbation experiments, this index between the NBC and AMOC transport variability is also supported by *Rühs et al.* (2015), provided that the interannual to decadal variability of the NBC wind-driven circulation is properly accounted for.

A 3D schematic of the South Atlantic western boundary currents and the water masses involved (Fig. 1.5) shows the poleward deepening of the BC from 0 to 1200 m and the equatorward shallowing of the current system represented by the Intermediate Western Boundary Current (IWBC), the North Brazil Undercurrent (NBUC) and the NBC from 1200 m to the surface (*Peterson and Stramma*, 1991; *Stramma and England*, 1999; *Mémery et al.*, 2000; *Soutelino et al.*, 2013). As shown in Fig. 1.5, the SASG shifts southward with depth, indicated by the southward migration of the zonal bifurcations (*Stramma and England*, 1999). It is also evident that south of ∼30°S the BC and the DWBC merge, which represents a water column of more than 3000 m flowing towards the Brazil-Malvinas confluence (*Garzoli*, 1993).

In this complex system of South Atlantic western boundary currents, the main water masses are highlighted in Fig. 1.5. The Tropical Water (TW) is a surface layer of salty and warm water, formed by subduction in the transition zone between the tropics and subtropics (*Stramma and England*, 1999; *Donners et al.*, 2005). Thus, the TW flows both equatorward and poleward as a subsurface salinity maximum. The South Atlantic Central Water (SACW) represents the thermocline waters with temperature between 20 and 5°C, and salinity between 36 and 34.6 psu (*Mémery et al.*, 2000). The SACW is produced locally within the Brazil-Malvinas confluence zone, and recirculates within the subtropical gyre (*Stramma and England*, 1999). The Antarctic Intermediate Water (AAIW) is situated between 600 m and 1200 m, and recognised by a salinity minimum ranging from 34.2 to 34.6 psu (*Stramma and England*, 1999; *Mémery et al.*, 2000; *Garzoli and Matano*, 2011). The AAIW in the South Atlantic originates from two sources: a surface region of the ACC layer, especially in the northern Drake passage and along the MC; and as an injection of Indian Ocean AAIW via the Agulhas leakage.

The NADW sits below the AAIW, and is transported by the DWBC throughout the South Atlantic western boundary. Although it is characterized as a laminar flow in Fig. 1.5, the DWBC breaks up into eddies at ∼8°S, shown by both hydrographic measurements and high resolution models (*Dengler et al.*, 2004; *Garzoli et al.*, 2015).

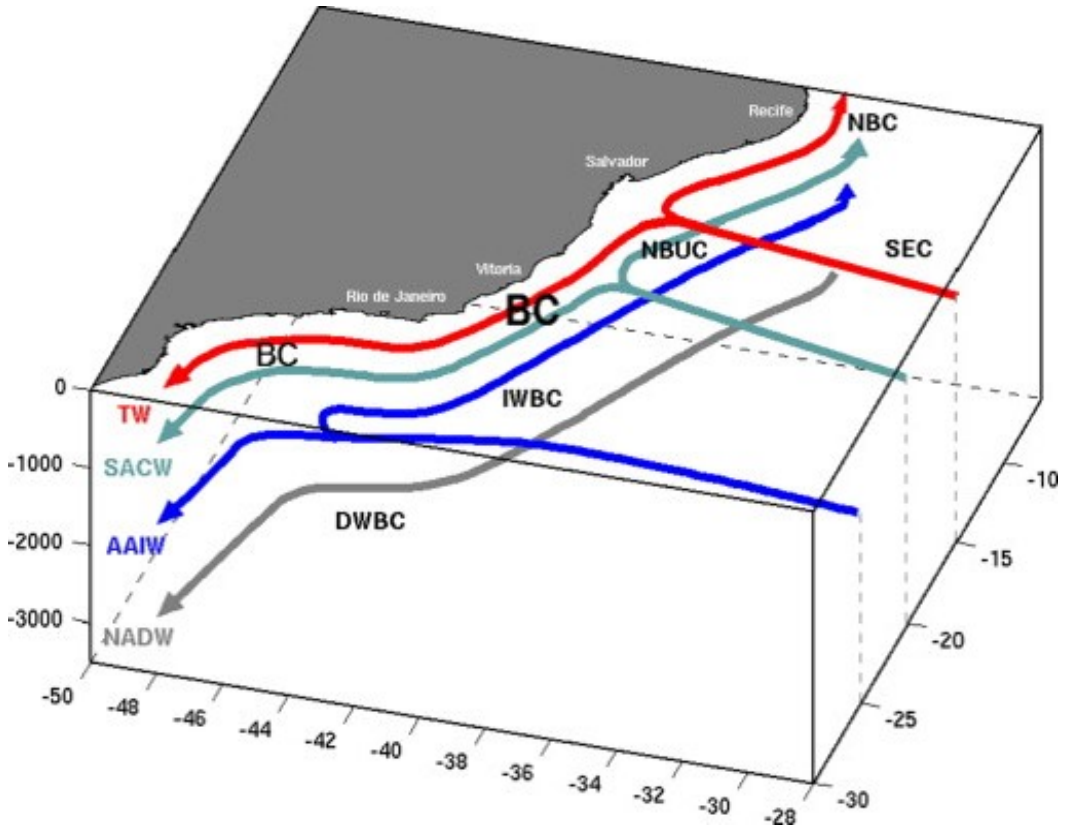

Figure 1.5: 3D schematic of the South Atlantic western boundary circulation and water masses from *Soutelino et al.* (2013).

Therefore, southward of ∼8°S the transport of NADW is accomplished by migrating eddies. Similarly, migrating rings transport NBC waters northward after the NBC is retroflected at ∼10°N (*Johns et al.*, 1990; *Fratantoni et al.*, 1995; *Jochumsen et al.*, 2010), deconstructing the view that the MOC operates as a simplified conveyor belt (*Lozier*, 2010).

1.5 AMOC bi-stability

Rapid changes in the climate system could be triggered when thresholds are exceeded, even if the trends in climate forcing are weak. One such important threshold for the climate system was proposed by *Stommel* (1961). He showed that the AMOC could have two equilibrium states under the same forcing conditions, which was defined as the

AMOC bi-stability. The ″on″ state corresponds to a strong Atlantic overturning cell as seen in the present climate, which is developed by deep convection of water masses in the northern Atlantic. The ″off″ state represents a collapsed AMOC. Changes in the current climate system, driven by an increased melting of sea ice or small but permanent changes in the hydrological cycle, may lead to a rapid transition from ″on″ to ″off″ states. Paleoclimate records also suggest very rapid changes in the past Atlantic climate, which have been linked to sudden changes in the AMOC strength, e.g. from melting ice sheets (*Broecker*, 1998, 2003).

In a simple model with a warm, salty box and another cold, fresh box, *Stommel* (1961) proposed that the overturning strength was driven by the meridional density difference between the two boxes, which in turn was controlled by the overturning transport of salt from the warm into the cold box. This feedback linking the salt advection and the overturning strength was then defined as the salt-advection feedback. Expanding the conceptual model proposed by *Stommel* (1961) to allow cross-hemispheric flows and making it directly applicable to NADW formation, *Rahmstorf* (1996) found that the AMOC stability depends on the sign of the overturning freshwater transport (F_{ov}) at the southern Atlantic boundary, more precisely at 34°S. Based on results from this simple box-model, *Rahmstorf* (1996) stated that when F_{ov} at 34°S is negative, i.e. AMOC exports freshwater from the Atlantic, a weakening of the AMOC leads to a freshening of the basin, causing a further weakening of the AMOC. In this case the salt-advection feedback is positive and has a destabilizing effect so that the AMOC is in a bi-stable regime. Conversely, if F_{ov} at 34°S is positive, a weakening of the AMOC makes the Atlantic saltier, thus encouraging recovery in the AMOC strength. In this case the salt-advection feedback is negative, has a stabilizing effect and the AMOC is in a monostable regime. Fig. 1.6 illustrates the salinity behavior of the upper and lower branches when the AMOC is considered to be in bi-stable or monostable regimes.

Liu et al. (2017) argue that F_{ov} at 34°S is not an accurate metric because it neglects the freshwater transport between the Atlantic and the Arctic. Therefore, recent coupled

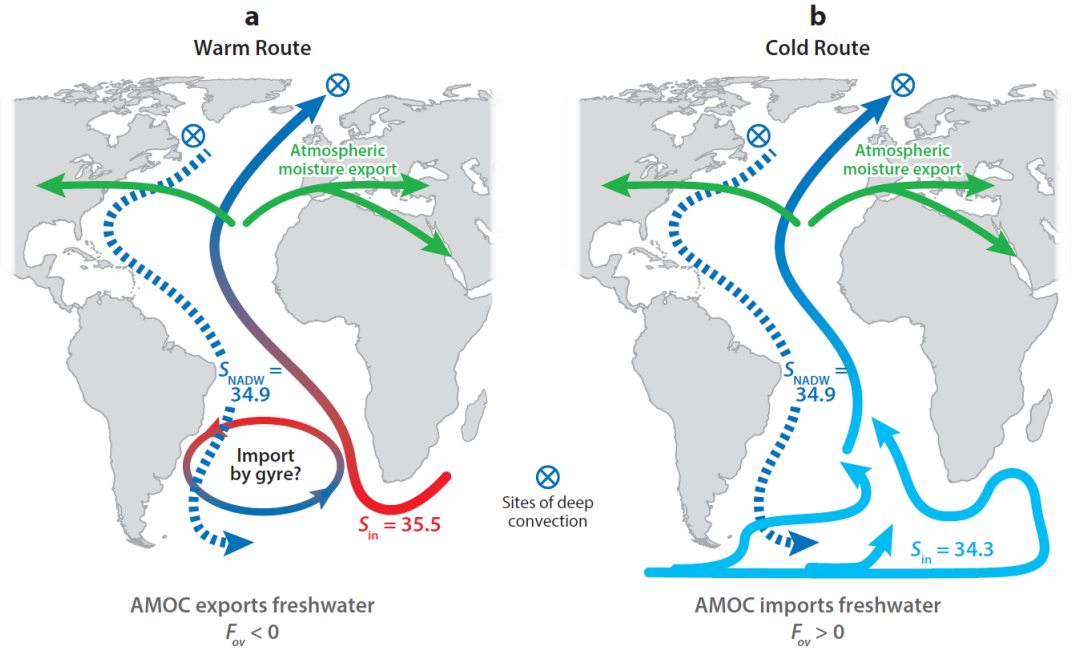

Figure 1.6: Situation of bi-stable (a) and monostable (b) AMOC regimes extracted from *Ferreira et al.* (2018). In (a) waters (red-blue arrow) get fresher as they are transported northward, so the deep flow (dashed blue arrow) is fresher than the upper branch, corresponding to an export of freshwater from the Atlantic basin (i.e. F_{ov} <0). In (b) the AMOC is fed by the cold (fresh) waters that get saltier as they are transported northward, consistent with a net evaporation over the Atlantic basin; the AMOC imports freshwater. The blue crossed circles indicate sites of deep convection.

modelling studies have refined this F_{ov} stability indicator at 34°S, by also considering AMOC-related freshwater transports across the northern Atlantic boundary (*Huisman et al.*, 2010; *Liu and Liu*, 2013; *Liu et al.*, 2017). They support that the F_{ov} divergence across the Atlantic boundaries would be a better stability indicator to represent the basin-wide salt-advection feedback. However, some other studies suggest to use the F_{ov} divergence only across the subtropical North Atlantic, the region where F_{ov} usually reaches a negative peak in both ocean and coupled models (*Yin and Stouffer*, 2007; *Mecking et al.*, 2016).

Regardless of the different F_{ov} metrics used as stability indicators, Fig. 1.7 summarizes the three main assumptions behind the salt-advection feedback mechanism, proposed by box-model studies. The first assumption relies on the fact that the over-

turning strength is proportional to the density difference between the North Atlantic and the southern ocean. This buoyancy-driven relationship finds support in some ocean models (*Griesel and Maqueda*, 2006; *Cheng et al.*, 2018) but not in others (*de Boer et al.*, 2010; *Wolfe and Cessi*, 2010). Additionally, southern ocean winds are suggested to have an important role in forcing the NADW upwelling and therefore the AMOC return flow (Fig. 1.1). This reveals a much more complex situation than the one proposed by box-models, showing that other AMOC drivers, rather than only buoyancy-driven processes, must be considered in the southern ocean.

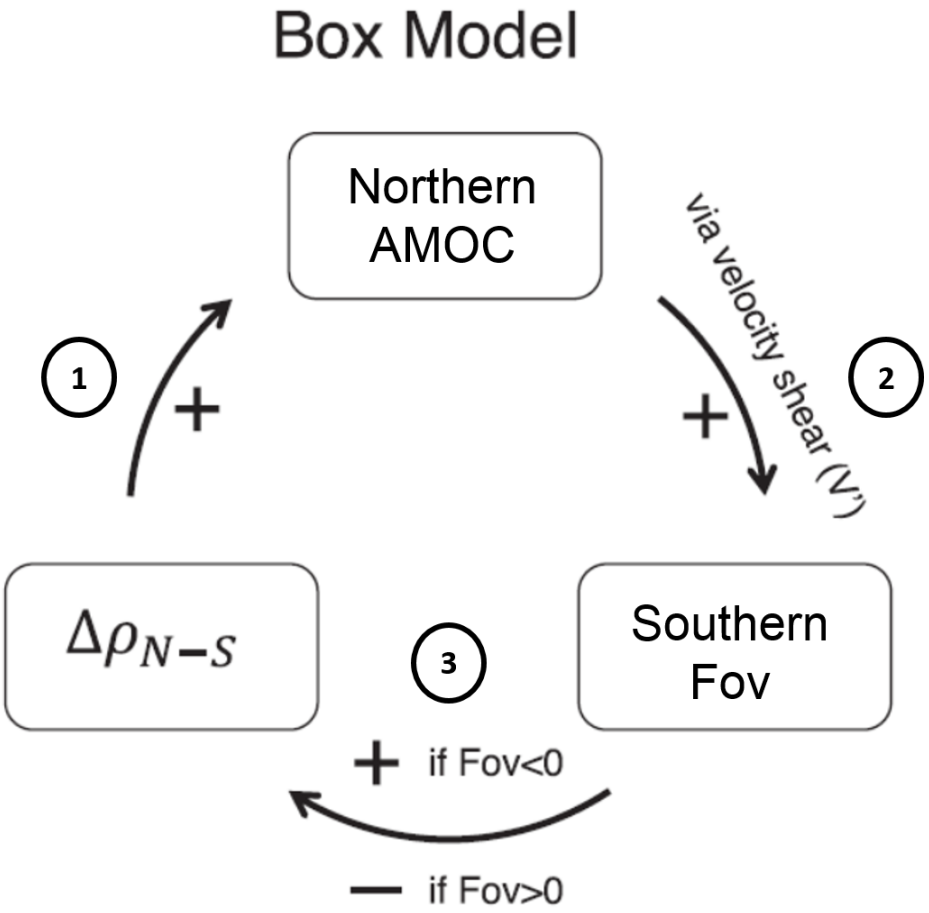

Figure 1.7: Schematic of the salt-advection feedback and its assumptions proposed by simple box-model studies, adapted from *Cheng et al.* (2018). The numbers relate to the assumptions in the order that they are referred to in the text.

The second assumption in Fig. 1.7 is that changes in F_{ov} are primarily driven by

changes in the circulation rather than changes in the salinity distributions throughout the Atlantic (*Rahmstorf*, 1996). This has been recently questioned by *Cheng et al.* (2018). They found that decadal and longer time-scale F_{ov} variability in two Earth system simulations is instead governed by salinity rather than velocity variations everywhere in the Atlantic apart from the northern subtropics. Consistently, *Cheng et al.* (2018) also showed that the long-term AMOC variability at 45°N in both Earth system models has only a weak effect on F_{ov} in the South Atlantic, suggesting that transport shear associated with basin-wide AMOC variability may not be a determinant factor in influencing the southern F_{ov} variability, at least in these models.

Finally, the third box-model assumption in Fig. 1.7 is based on the fact that changes in the southern F_{ov} perturb the north-south density differences, and as such, they feedback on the northern AMOC. Previous modelling studies also call this assumption into question, as they show that decadal north-south density differences are almost entirely controlled by density fluctuations in the northern Atlantic rather than in the southern ocean (*Griesel and Maqueda*, 2006; *Danabasoglu*, 2008; *Cheng et al.*, 2018). Some of these studies, such as *Danabasoglu* (2008) and *Yeager and Danabasoglu* (2014), reveal that the AMOC multidecadal variability is closely related to subpolar North Atlantic density variations. Therefore, this suggests that processes pertaining to the North Atlantic might be the most important forcing mechanism for the AMOC variability on these timescales. This is also supported by *Cheng et al.* (2018), who found no evidence of southern F_{ov} feedbacks on the northern AMOC in the long-term variability of two Earth System simulations. This was proposed by *Cheng et al.* (2018) as the main missing link in Fig. 1.7 in preventing the feedback loop from closing for internal variability in these two models. However, care must be taken since the salt export from the Agulhas leakage, for example, is argued to be a source of multidecadal variability for the northern AMOC (*Weijer et al.*, 2002; *Biastoch et al.*, 2008a)

The reliability of F_{ov} as a stability indicator also depends on its relative importance when compared to the other components of the Atlantic freshwater budget. Observa-

tional analysis suggests that the AMOC currently exports freshwater out of the Atlantic basin (e.g. *Garzoli et al.*, 2013), which corresponds to a negative F_{ov}. Since the Atlantic is also a net evaporative basin (*Wijffels et al.*, 1992), the closure of the North Atlantic freshwater budget requires a large freshwater input into the basin by a process other than the AMOC (Fig. 1.6). Eddy-driven mixing and particularly wind-driven gyres are often invoked as potential sources of freshwater being transported into the North Atlantic (*De Vries and Weber*, 2005; *Sijp*, 2012; *Mecking et al.*, 2016; *Ferreira et al.*, 2018). As noted by *Sijp* (2012), the gyre component in the South Atlantic can adjust in conjunction with F_{ov} during a changing AMOC. In an eddy-permitting coupled model, *Mecking et al.* (2016) showed that changes in the gyre transports are twice as large as changes in F_{ov} at 34°S, after a transition from ″on″ to ″off″ states.

Furthermore, F_{ov} has also been shown to be sensitive to biases in models from the Coupled Model Intercomparison Project 5 (CMIP5). *Mecking et al.* (2017) clearly showed that correcting salinity biases in CMIP5 models impacts F_{ov} everywhere south of the North Atlantic subtropical gyre, even changing its sign in the South Atlantic. According to *Mecking et al.* (2017), correlations between the AMOC strength at 26.5°N and F_{ov} 34°S are only explained by the dependence of the salinity biases on the AMOC. After the model salinities are corrected, these correlations become negligible.

The AMOC bi-stability in coupled models remains an open question. Freshwater hosing experiments have been able to produce AMOC ″off″ states in coarse models (e.g. *Rahmstorf*, 1996), but the development of an ″off″ state is not clear in more complex climate models. Some freshwater hosing experiments in complex coupled systems do not show any evidence of an AMOC shutdown (e.g. *Stouffer et al.*, 2006), whereas others are able to maintain a collapsed AMOC state for 450 years (e.g. *Mecking et al.*, 2016). However, as pointed out by *Gent* (2018), 450 years of a collapsed AMOC is not a conclusive proof that this state is truly at equilibrium. Despite the uncertainties of a bi-stable AMOC in modelling studies, the last generation of coupled models has indeed revealed potential feedbacks in the atmosphere (*Yin and Stouffer*, 2007) and in the

ocean (*Mecking et al.*, 2016), challenging the central role played by F_{ov} in determining the AMOC stability.

A different view of AMOC stability indicators is also given by *Saenko et al.* (2003). By applying freshwater perturbations only in the AAIW formation regions, they show that the transition between the ″on″ and ″off″ states in a coupled model occurs when the densities in the AAIW and NADW formation regions become comparable to each other. Therefore, when the AAIW density becomes larger (smaller) than the NADW density, the result is the rapid development of an AMOC ″off″ (″on″) state. They conclude that one of the reasons for a stable modern climate is the larger density difference of the NADW over the AAIW, when compared to glacial climates.

1.6 Research goals

The overall goal of this thesis is to investigate the Atlantic ocean transports, particularly in the South Atlantic, focusing on their variability and feedbacks on the climate system from a variety of model products, including FRMs with distinct spatial resolutions, state-of-the-art ORAs and coupled climate simulations. In this context this research aims to address the following key questions:

- What are the benefits and limitations of DA in improving the simulations of the South Atlantic ocean circulations, which are otherwise difficult to measure? How sensitive are FRM and ORA heat transports with respect to variations in temperatures and meridional velocities in distinct oceanic regions?
- What is the role of salinity in modulating freshwater transports across the Atlantic? How do FRM and ORA salinity distributions reveal climate feedbacks between F_{ov} transports and the AMOC?
- Can evidence for salt-advection feedback assumptions (Fig. 1.7) be detected in the internal variability of coupled climate simulations?

1.7 Thesis outline

The research questions posed above are addressed into the next four chapters, as follows:

- Chapter 2 describes the dataset of FRMs and ORAs, introduces a mathematical framework for how their transports are calculated, and documents a detailed evaluation of the South Atlantic circulation in these model products, which are compared to hydrographic measurements and recent observational studies. The evaluation considers two main regions: (i) the southern Atlantic, where the model products are compared to high-density lines of eXpendable BathyThermographs (XBTs) at 35°S; and (ii) the western boundary of the tropical South Atlantic, where the model products are compared to western boundary velocity measurements from a moored array section at 11°S.

- Chapter 3 focuses on the South Atlantic meridional heat and volume transports between 35°S and the equator, using the same dataset of FRMs and ORAs presented in Chapter 2. The benefits and limitations of DA in changing the circulation are evaluated by performing several analyses to quantify relevant contributions to the inter-model transport spread. It is analysed how variations in temperature and meridional velocities, particularly at the western boundary compared with ocean interior, contribute to explain transport agreements and disagreements between the model products. The time variability of the ORA transports, particularly after Argo data became available, is also evaluated.

- Chapter 4 shows similar analyses with the same FRMs and ORAs to investigate the role of vertical and horizontal salinity gradients in modulating, respectively, the overturning and gyre freshwater transports throughout the Atlantic. These analyses are combined with analyses of the AMOC strength to elucidate climate feedbacks between F_{ov} and the AMOC in the South Atlantic, with important implications for theories of AMOC bi-stability.

- Chapter 5 evaluates whether the salt-feedback mechanisms (Fig. 1.7) are valid in the pre-industrial runs of two CMIP5 model groups, which are distinguished by the sign of F_{ov} in the southern Atlantic. The mean transports and salinity patterns are firstly evaluated within the two groups and linked to previous FRM and ORA results in Chapter 4. The long CMIP5 simulations are then further used to identify: (i) whether salinity or meridional velocity variability dominates F_{ov} variability on a range of timescales; (ii) whether meridional freshwater content gradients are dominated by freshwater transports in the North or in the South Atlantic; and (iii) how far the southern F_{ov} can be correlated to the AMOC transports throughout the basin.

Finally, general conclusions and recommendations for further research are given in Chapter 6. This research resulted in two published papers. The findings of Chapter 2 and particularly Chapter 3 were condensed and published in Ocean Science (*Mignac et al.*, 2018). The findings of Chapter 4 were published in Geophysical Research Letters (*Mignac et al.*, 2019). ORA diagnostics developed by this research were also used in ORA intercomparisons for other ocean basins, contributing to ORA papers in the polar regions (*Uotila et al.*, 2019) and in the North Atlantic (*Jackson et al.*, 2019). The former was published in Climate Dynamics and the latter was published in Journal of Geophysical Research.

CHAPTER 2

FREE-RUNNING MODELS AND OCEAN REANALYSES

2.1 Overview

This Chapter provides in Section 2.2 a detailed description of the FRMs and ORAs that are used in this thesis, followed by the mathematical framework of how their meridional transports are calculated in Section 2.3. Section 2.4 shows results of the South Atlantic transport evaluation in these model products, comparing them with trans-basin and western boundary hydrographic estimates at 35°S and 11°S, respectively. Section 2.5 evaluates the transports of GloSea5 reanalysis in the South Atlantic and proposes reasons why they are so different from all the other model products. Finally, Section 2.6 ends the Chapter with discussion and conclusions.

2.2 Description of the dataset

Two FRMs and five ORAs, each with a global domain, are considered in this work. All the products are configured with the Nucleus for European Modelling of the Oceans (NEMO; *Madec*, 2008) model, which is a state-of-the-art primitive equation z-level model employing both hydrostatic and Boussinesq approximations. For all products,

NEMO is configured with a partial cell topography (*Adcroft et al.*, 1997), and a quasi-isotropic tripolar ORCA grid (*Madec and Imbard*, 1996). Sub-sections listing the main characteristics of the FRMs and ORAs are presented below. Tab. 2.1 compares the main configurations of each product.

2.2.1 Free-Running Models

The standard configurations of the FRMs at 1/4° and 1/12° horizontal resolution used here have been setup within the DRAKKAR consortium (e.g. *Barnier et al.*, 2006; *Penduff et al.*, 2010; *Treguier et al.*, 2014; *Marzocchi et al.*, 2015). The FRM at 1/4° horizontal resolution, hereafter FRM4, has 46 z-levels with thickness ranging from 6 m at the surface to 250 m at the ocean bottom. FRM4 is forced by the ERA-Interim atmospheric reanalysis product (*Simmons et al.*, 2007) from the European Centre for Medium-Range Weather Forecasts (ECMWF). The ERA-Interim reanalysis provides winds at 10 m, surface air temperature and humidity at 2 m, daily radiative fluxes and precipitation fields, which are used to compute 6-hourly turbulent air/sea fluxes using the *Large and Yeager* (2004) and *Large and Yeager* (2009) bulk formulae. The integration of FRM4 was conducted at the University of Reading and is described in *Haines et al.* (2012) and *Stepanov and Haines* (2014) as the free control run associated with the University of Reading Reanalysis Version 3 (UR025.3). The initial conditions in 1989 are derived from a previous 1/4° run with hydrographic data assimilation (*Smith and Haines*, 2009). A moderate relaxation of SSS is applied towards *Levitus et al.* (1998) with a time scale of approximately 180 days.

The FRM at 1/12° horizontal resolution, hereafter FRM12, has 75 z-levels. Its vertical grid is refined at the surface (1 m for the first level), smoothly increasing to a maximum thickness of 200 m at the bottom. The integration of FRM12 was performed by the Marine Systems Modelling group at the National Oceanography Centre in Southampton, and is described in *Marzocchi et al.* (2015). The DRAKKAR Surface Forcing Set 4.1 (DFS4.1) or Set 5.1 (DFS5.1) is employed, depending on the time period

as shown by Tab. 2.1. As detailed in *Brodeau et al.* (2010), DFS combines elements from two sources: (i) the Coordinated Ocean Research Experiments (CORE) forcing dataset, from which daily radiative fluxes and monthly precipitation are extracted; and (ii) ECMWF products from which wind, surface air temperature and humidity fields are taken. As in FRM4, 6-hourly momentum and heat turbulent fluxes are computed in FRM12 following *Large and Yeager* (2004) and *Large and Yeager* (2009). FRM12 is initialised in 1978 from *Levitus et al.* (1998) climatology and applies the same SSS restoring term as in FRM4. Both FRM4 and FRM12 employ a free-slip (no-stress) configuration for the lateral momentum boundary conditions. Both of their sea-ice components are resolved employing NEMO's native Louvain-la-Neuve Sea Ice Model version 2 (LIM2; *Timmermann et al.*, 2005).

2.2.2 Ocean Reanalyses

The MyOcean global ocean reanalysis activity provided a series of global ORAs at eddy-permitting resolution (1/4°) constrained by assimilation of observations and covering the altimetric era (i.e. period starting with the launch of TOPEX POSEIDON and ERS-1 satellites at the end of 1992). Five of these ORAs are considered, namely: (i) the Ocean Reanalysis Pilot 5 (ORAP5; *Zuo et al.*, 2015) from ECMWF; (ii) the Global Ocean Reanalysis System version 5 (CGLORSV5; *Storto and Masina*, 2016) from the Centro Euro-Mediterraneo sui Cambiamenti Climatici (CMCC); (iii) the University of Reading Reanalysis Version 4 (UR025.4; *Valdivieso et al.*, 2014); (iv) the Global Ocean Reanalysis and Simulation Version 4 (GLORYS2V4; *Lellouche et al.*, 2013) from Mercator Ocean; and (v) the Global Seasonal Forecast System 5 Reanalysis (GloSea5; *Blockley et al.*, 2014) from the UK MetOffice. These ORAs employ different state-of-the-art ocean DA systems, which assimilate, in distinct ways, reprocessed observations of sea level anomaly (SLA), SST, in situ temperature (T) and salinity (S) profiles, and sea ice concentration (SIC). The DA schemes vary between variational methods (e.g. ORAP5, CGLORSV5 and GloSea5) and ensemble-based methods (e.g. GLORYS2V4),

which differ in the way how the model error covariances are treated. In variational methods, the model error covariances are parameterized by the variances of ocean variables and the assimilation increments are balanced following physical relationships in the ocean, such as the water-mass property conservation, the equation of state, and the geostrophic and hydrostatic balances (*Storto et al.*, 2011; *Mogensen et al.*, 2012). Since the geostrophic balance is not a valid assumption in equatorial areas, this makes more challenging to balance the velocity increments and constrain the circulation near the equator (e.g. *Waters et al.*, 2017). In ensemble-based methods, the model error covariances are estimated by ensemble anomalies (e.g. *Lellouche et al.*, 2013). Therefore, the size and perturbations applied to the ensemble are of great importance to increase its spread and give more representative ensemble anomalies for the estimation of model error covariances (*Pham et al.*, 1998). The main references of the ORA DA schemes and their assimilated observations can be found in Tab. 2.1. The vertical discretisation of GLORYS2V4, ORAP5, UR025.4 and GloSea5 follows exactly the same configuration as in FRM12 with 75 z-levels. CGLORSV5 has 50 z-levels in a similar configuration to FRM4.

All the ORAs are forced with the ERA-Interim atmospheric reanalysis product from ECMWF. The turbulent air-sea fluxes were calculated using the same methodology as in the FRMs, but their input into NEMO varies between 3 and 6-hour sampling depending on the product (see Tab. 2.1). In GLORYS2V4, large-scale corrections of the atmospheric forcings are also applied (*Lellouche et al.*, 2013), whereas in ORAP5 the impact of surface wave forcing on the ocean mixing and circulation is included (*Janssen et al.*, 2013). As in the FRMs, NEMO is coupled to the LIM2 sea-ice model, except in GloSea5 which is coupled to the Los Alamos Sea Ice Model (CICE3.0; *Hunke and Lipscomb*, 2010).

The surface relaxations differ between the ORAs. In ORAP5 and CGLORSV5, the SST data in Tab. 2.1 are used to correct the turbulent heat fluxes, with a restoring term of -200 W m^{-2} K^{-1}. The SSSs are also relaxed towards the World Ocean Atlas

Table 2.1: The ocean model products and their central configurations.

Products	Model	Forcings	Data assimilation	Assimilated observations	Initial condition
FRM4	NEMO3.2-LIM2, 1/4°, 46 z-levels	6-hourly ERA-Interim	None	None	1/4 run with hydrographic data assimilation
FRM12	NEMO3.2-LIM2, 1/12°, 75 z-levels	6-hourly DFS4.1 (1978-2007) and 5.1 (2008-2010)	None	None	Levitus (1998) T/S climatology
ORAP5	NEMO3.4-LIM2, 1/4°, 75 z-levels	6-hourly ERA-Interim with wave forcing	NEMOVAR (3D-Var) (*Mogensen et al.*, 2012)	OSTIA SST, AVISO SLA, in situ T/S profiles from EN3_v2 with bias correction for XBT, OSTIA sea-ice concentration	12-year spin-up initialised from WOA09 T/S climatology and followed by 5-year assimilation run
CGLORSV5	NEMO3.2-LIM2, 1/4°, 50 z-levels	3-hourly ERA-Interim	Global OceanVar (3D-Var) (*Storto et al.*, 2011)	Reynolds 1/4° run with hydrographic data assimilation AVHRR + AMSR-E SST, AVISO SLA, in situ T/S profiles from EN3_v2 with bias correction for XBT, NSIDC (NASA Team algorithm) sea ice concentration	Mean January condition of a 4-year spin-up initialised from EN4 T/S analysis
UR025.4	NEMO3.2-LIM2, 1/4°, 75 z-levels	6-hourly ERA-Interim	Met Office FOAM NEMO assimilation system (Optimal Interpolation) (*Storkey et al.*, 2010)	ICOADS in situ SST and NODC satellite SST, AVISO SLA, in situ T/S profiles from EN3_v2 with bias correction for XBT, EUMETSAT OSISAF sea ice concentration	EN3 T/S analysis
GLORYS2V4	NEMO3.1-LIM2, 1/4°, 75 z-levels	3-hourly ERA-Interim with radiative flux corrections	SAM2 (Singular Evolutive Extended Kalman Filter) (*Pham et al.*, 1998)	Reynolds 1/4° AVHRR-only SST, AVISO SLA, in situ T/S profiles from Coriolis CORA4.1 database, CERSAT sea ice concentration	EN4 T/S analysis
GloSea5	NEMO3.2-CICE, 1/4°, 75 z-levels	3-hourly ERA-Interim	NEMOVAR (3D-Var) (*Mogensen et al.*, 2012)	GTS in situ SST and AVHRR+GHRSST satellite SST, AVISO SLA, in situ T/S profiles from EN4, EUMETSAT OSI-SAF sea ice concentration	EN3 T/S analysis

2009 (WOA09; *Locarnini et al.*, 2010) for ORAP5, and towards the UK Met Office ENhAnced ocean data assimilation and ClimaTe prediction (ENACT/ENSEMBLES) EN4 dataset (*Good et al.*, 2013) for CGLORSV5, with time scales of approximately 300 days. No global SST and SSS restoring strategies have been implemented in UR025.4, GloSea5 or GLORYS2V4, and the only surface restoring mechanism is through the increments introduced by data assimilation itself. As also seen in Tab. 2.1, the initialisation and spin-up differ between the ORAs. On lateral boundaries, UR025.4, ORAP5 and GloSea5 adopt a free-slip configuration, whereas CGLORSV5 and GLORYS2V4 employ a partial-slip condition. In the latter, the constant of proportionality (α) between the tangential stress and the tangential velocity is defined as 0.5 for both products. More specific details comparing these NEMO-based ORAs can be found in *Masina et al.* (2015).

Monthly averages of the FRMs and ORAs are used for the analyses in Chapters 2, 3 and 4. The use of monthly means mitigates possible jumps introduced by incremental assimilation over a time window of several days. In order to avoid any dynamical spin-up in the early years of the simulation for products starting in the early nineties (e.g. GLORYS2V4), and because UR025.4 ends in 2010, a common time period from 1997 to 2010 is chosen to calculate the mean transports.

2.3 Mathematical Framework

In order to compare the transports with South Atlantic hydrographic measurements in Section 3.3, the model overturning stream function is calculated at any latitude as below:

$$\psi(z) = \int_W^E \int_z^0 v(x,z)dzdx \tag{2.1}$$

where z is the vertical coordinate increasing upward, W and E correspond to the western and eastern boundaries, and v represents the model meridional velocity. The

overturning strength ψ_{max} at each latitude is defined as the vertical maximum of the stream function. The depth of ψ_{max} is denoted by z_{max}. The volume transports for any particular zonal section can also be calculated redefining the west-east and depth limits of the integrals in Eq. 2.1. For example, in the case of the NBC in subsection 2.4.2, its transport across the western boundary current is calculated between the depths of particular isopycnals, following the same methodology as in *Schott et al.* (2005) and *Hummels et al.* (2015).

Similarly to the overturning stream function, the model MHT at any latitude is given by:

$$MHT = \rho C_p \int_W^E \int_{-H}^0 vT dz dx \tag{2.2}$$

where ρ is the seawater density ($\sim$1025 $kg\ m^{-3}$), C_p is the specific heat capacity of seawater ($\sim$4000 $J\ kg^{-1}\ ^\circ C^{-1}$), and T is the potential temperature.

The AMOC transports can be represented by the sum of the geostrophic (ψ_{Geo}) and Ekman (ψ_{Ek}) components, where the Ekman transport is calculated from the zonal wind stress τ_x at any latitude:

$$\psi_{Ek} = -\int_W^E \frac{\tau_x}{\rho f} dx \tag{2.3}$$

where f is the Coriolis parameter.

ψ_{Geo} is calculated indirectly by the difference between ψ_{max} and ψ_{Ek}.

2.4 South Atlantic transport evaluation

In this section FRM and ORA transports are compared to hydrographic measurements in the southern Atlantic and at the western boundary of the tropical South Atlantic. In the former region, the quarterly high-density XBT-based estimates (XBT-AX18) at $\sim$35°S (*Garzoli and Baringer*, 2007) from 2002 to 2010 are used for comparison, as well

as recent observational estimates which employ different methodologies to calculate the SAMOC between 35°S and 20°S. For example, an Argo climatology (*Dong et al.*, 2014), altimeter synthetic profiles based on the correlation of the AVISO SLA and isotherm depths (*Dong et al.*, 2015), and dynamic height fields from Argo and sea surface heights (SSHs) from AVISO (*Majumder et al.*, 2016), are used together with wind fields to provide observation-based estimates of the total transports in the southern Atlantic. None of these observational estimates can be regarded as truly independent of the ORAs, because all the datasets mentioned above, including the XBTs, are assimilated (see Tab. 2.1).

In the tropical South Atlantic, the comparison is mostly focused on the western boundary at 11°S. At this latitude, the NBC and DWBC transports are based on high-frequency velocity measurements from a moored western boundary array section, with transport estimates from 2000 to 2004 (*Schott et al.*, 2005) and from 2013 to 2014 (*Hummels et al.*, 2015). These are independent observations from the ORAs.

2.4.1 Southern Atlantic

In order to provide a fair comparison with the XBT-AX18 measurements, the FRM and ORA transports at 35°S are sampled in the same months as in the 2002-2010 XBT-AX18 measurements. Comparison with these observational estimates (Fig. 2.1) suggest that the ORA SAMOCs and MHTs, with the exception of GloSea5, are stronger and more realistic than those of the FRMs at 35°S. For example, UR025.4 and GLO-RYS2V4 have very similar SAMOC strengths to the XBT-AX18 transects and other observation-based studies, showing 17.51 $\pm$ 3.4 Sv and 18 $\pm$ 3.3 Sv, respectively. However, their MHTs are still 0.1 PW lower than the lowest observational estimate from *Dong et al.* (2015). The MHT underestimation of the FRMs and ORAs relative to the observations at 35°S has already been reported by several authors (e.g. *Dong et al.*, 2011a; *Dong et al.*, 2011b; *Perez et al.*, 2011; *Sitz et al.*, 2015; *Majumder et al.*, 2016; *Stepanov et al.*, 2016). Significant XBT-derived trends across 35°S after the late

1990s (*Goes et al.*, 2015a), uncertainties in the reference level of geostrophic velocities, and the sampling resolution of the western boundary (*Goes et al.*, 2015b) might also contribute to the XBT-AX18 MHT overestimation with respect to the ORAs in Fig. 2.1b. Among the ORAs, GloSea5 has an unusually low SAMOC strength and its MHT is actually southward (i.e. negative), whereas all the other model products and observation estimates show a northward MHT. Therefore, there is clearly an issue with GloSea5 transports in the South Atlantic. For this reason, GloSea5 transports are not considered in this Section and are discussed separately in Section 2.5.

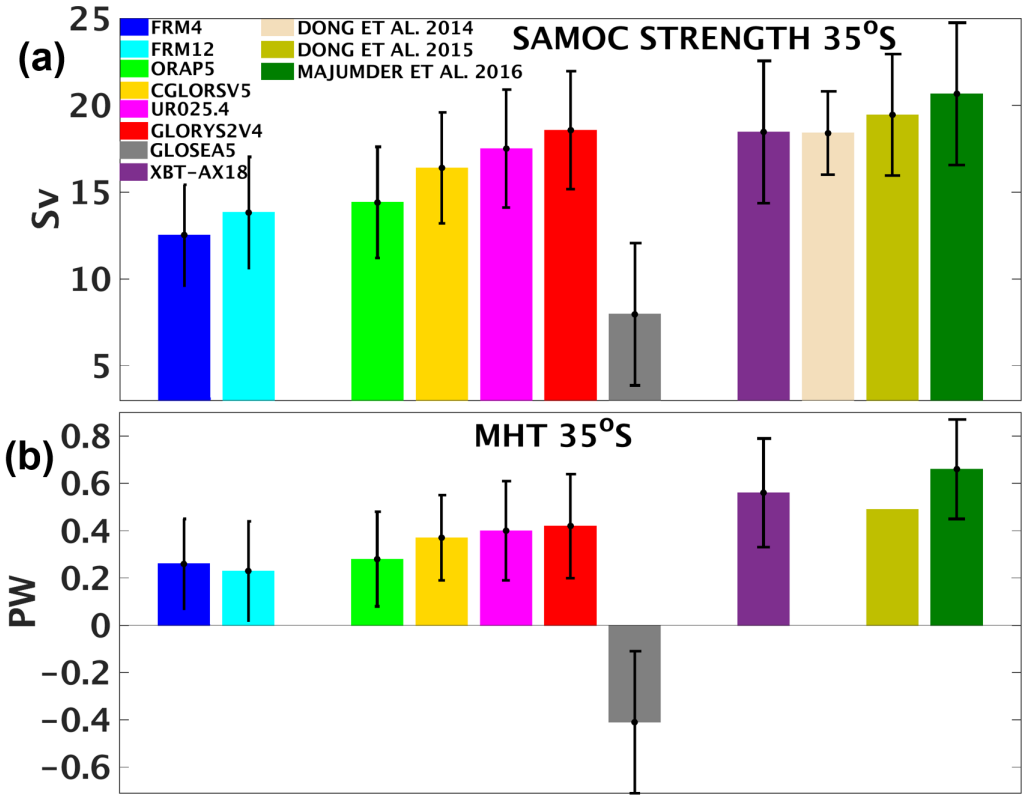

Figure 2.1: The (a) SAMOC strength ψ_{max} (Sv) and (b) MHT (PW) at 35°S. The black bars in (a) and (b) represent monthly standard deviations, except for the XBT-AX18, *Dong et al.* (2015) and *Majumder et al.* (2016) estimates which correspond to quarterly, weekly and daily standard deviations, respectively. In the model products, the SAMOC strength and MHT are sampled in the same months as in the 2002-2010 XBT-AX18 measurements.

Fig. 2.2 shows that the seasonal cycle of ψ_{max} at 35°S, with amplitude varying

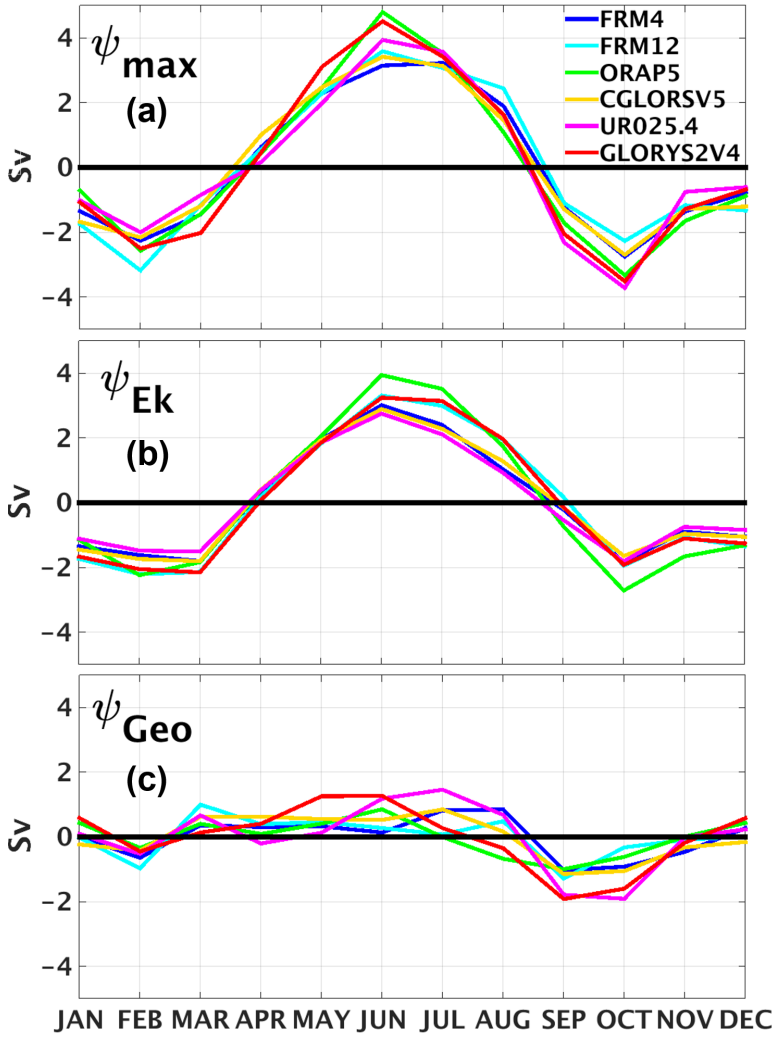

Figure 2.2: The seasonal cycle at 35°S of (a) ψ_{max} (Sv), (b) ψ_{Ek} (Sv) and (c) ψ_{Geo} (Sv).

from 6 Sv (FRM4) to 7.2 Sv (ORAP5), is driven by the seasonal cycle of ψ_{Ek} (Fig. 2.2b), having a clear peak in June-July. This matches quite well the Ekman transports dominating the SAMOC seasonal cycle in other modelling studies at 35°S (e.g. *Majumder et al.*, 2016; *Stepanov et al.*, 2016), which have very similar amplitudes to those shown by Fig. 2.2b. However, the dominance of the Ekman seasonal component in the XBT-AX18 transects is masked by an out-of phase relationship with the geostrophic component, resulting in a SAMOC seasonal cycle of only 1.8 Sv (*Dong et al.*, 2009). The model products do not have any clear seasonal cycle in the geostrophic transports

(Fig. 2.2c), while other observation-based estimates at 35°S also show a much stronger SAMOC seasonal cycle of ∼7 Sv (*Dong et al.*, 2014; *Dong et al.*, 2015). According to *Meinen et al.* (2013) and *Goes et al.* (2015b), the XBT-AX18 transects may be influenced by sampling aliasing in space and time which could result in a weaker SAMOC seasonal cycle.

In order to understand the boundary current contributions to the SAMOC strength in Fig. 2.1a, Fig. 2.3 shows the SAMOC upper branch transports at 35°S divided into western, interior and eastern boundary components as in *Dong et al.* (2009) and *Dong et al.* (2014). The western boundary (Fig. 2.3a) is dominated by the southward flow of the BC whereas the eastern boundary (Fig. 2.3c) is dominated by the northward flow of the Agulhas leakage. The western boundary and interior transports are stronger in the ORAs than in the FRMs, and are in better agreement with the observational estimates, despite differences of ∼5 Sv between some ORAs and the XBT-AX18 transects in Fig. 2.3a. The eastern boundary transport is ∼29 Sv in the observational estimates, also slightly higher than ∼26 Sv in the FRM12 and GLORYS2V4 which have the largest transports among the model products in Fig. 2.3c.

At 35°S, top-to-bottom transports accumulated from west to east are displayed in Fig. 2.4. The model transports are sampled in the same XBT-AX18 months to be consistent with the accumulated top-to-bottom transports shown by *Dong et al.* (2009). The model products show an accumulated transport of approximately -40 Sv in the western boundary region, which is 5 Sv lower than XBT-AX18 estimates. The differences in the accumulated transports between the model products and the XBT-AX18 values become even larger at 3°E, where most of the products reach -20 Sv while the observations still show approximately -35 Sv. This 15 Sv difference is compensated by a stronger XBT-AX18 northward flow at the eastern boundary, which is consistent with Fig. 2.3c.

The FRM12 has a signature of the northward MC at the western boundary (Fig. 2.4), which is not seen in the XBT-AX18 transects. This northward flow reaches up to

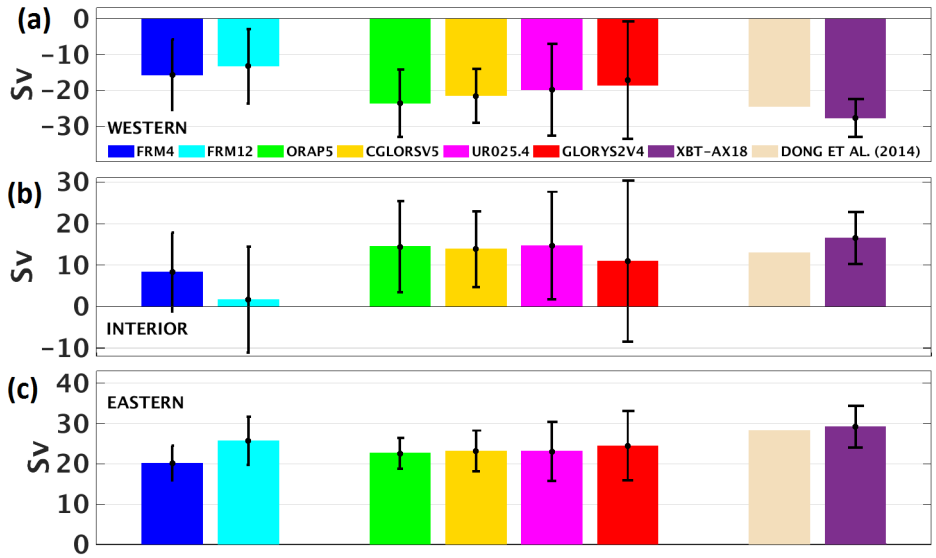

Figure 2.3: Transports (Sv) at 35°S down to z_{max} for the (a) western boundary (west of 48°W), (b) interior (from 48°W to 3°E), and (c) eastern boundary (east of 3°E). These three regions are defined as in *Dong et al.* (2009) and *Dong et al.* (2014). In the model products the transports are sampled in the same months as in the 2002-2010 XBT-AX18 measurements.

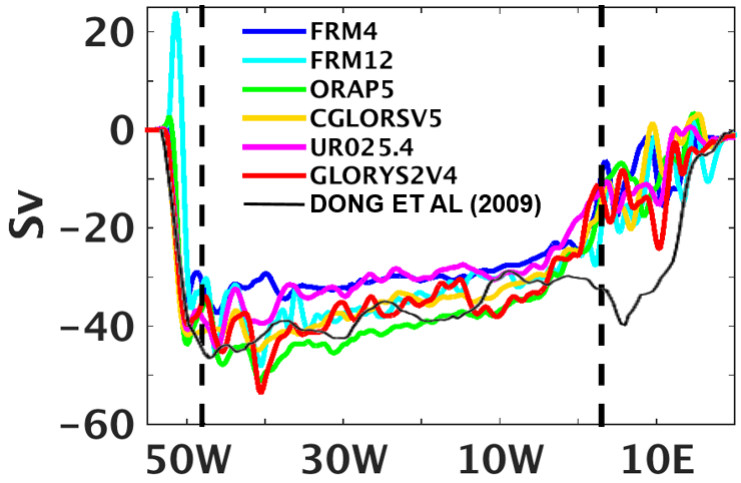

Figure 2.4: Top-to-bottom transports (Sv) at 35°S accumulated from west to east for all the model products and XBT-AX18 measurements from *Dong et al.* (2009). The vertical dashed lines correspond to the limits at 48°W and 3°E, used to separate western, interior and eastern boundaries, respectively. The model transports are sampled in the same XBT-AX18 months as in *Dong et al.* (2009).

~20 Sv in FRM12 and is counteracted by a stronger BC, which alters the accumulated transports by more than 50 Sv (i.e. from 20 Sv to -35 Sv) by 48°W. The presence of

the MC at 35°S explains the weak southward western boundary transports of FRM12 within the SAMOC upper branch (Fig. 2.3a). The misrepresentation of the Brazil-Malvinas confluence in the FRM12 is clearly seen in the 1997-2010 SSH maps of Fig. 2.5. The cold MC water, represented by low SSHs, extends further north in FRM12, reaching up to ∼34°S. The mean position of the Brazil-Malvinas confluence in the other ORAs, particularly CGLORSV5, UR025.4 and GLORYS2V4, is limited to ∼36°S and this is in a much closer agreement with the AVISO gridded product.

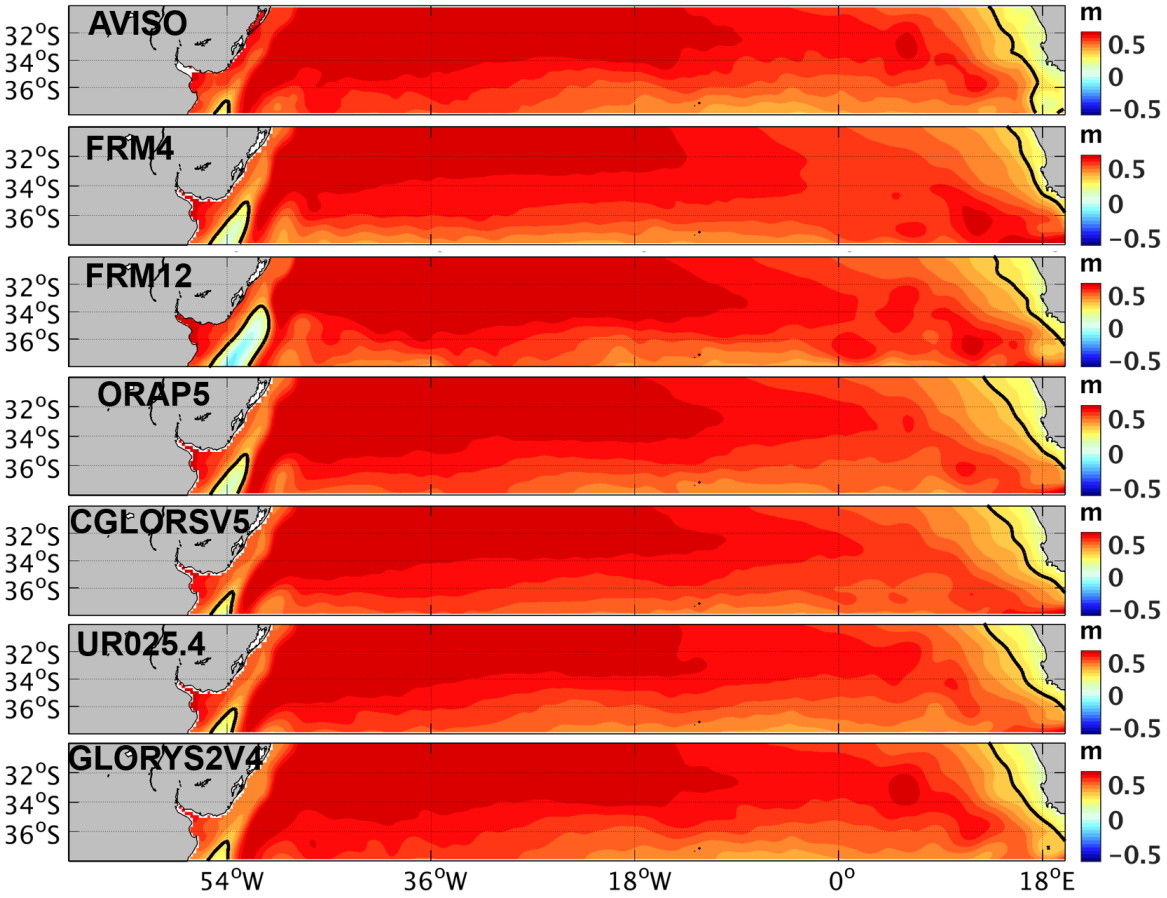

Figure 2.5: The 1997-2010 SSH (m) in the southern Atlantic for AVISO and the model products. The solid black line represents the contour of 0.3 m. The offset of the model SSHs with respect to AVISO is removed to allow a better comparison of the mean circulation features.

On the eastern side of the basin it is observed the mean SSH shape of the Agulhas retroflection (Fig. 2.5), which releases large rings of warm and salty water from

the Indian Ocean into the South Atlantic. The mean SSH structure of the Agulhas retroflection also varies reasonably between the FRMs and ORAs with GLORYS2V4 showing the closest SSHs relative to AVISO eastward of ∼0°E. The differences found there between the ORAs may be due to the different DA methods employed (Tab. 2.1) and how altimetry observations, particularly the Mean Dynamical Topography (MDT), are treated in each of them (*Backeberg et al.*, 2014; *Masina et al.*, 2015).

2.4.2 Tropical South Atlantic

Figure 2.6 shows the western boundary meridional circulation at 11°S where the NBC core is already well developed and extends down to ∼1200 m. The ORAs have a stronger western boundary circulation compared to the FRMs. For example, the ORA NBC core is generally broader and reaches up to 0.6 m/s at 11°S, which is consistent with measurements of *Schott et al.* (2005) and *Hummels et al.* (2015).

The NBC and DWBC transports at 11°S (Fig. 2.7) are calculated using the same neutral density interfaces as in *Hummels et al.* (2015), which separate the NBC and the DWBC layers in the model products (Fig. 2.6). As a result of the stronger western boundary circulation reproduced by the ORAs, their NBC transports are larger than the FRMs (Fig. 2.7a). The UR025.4 and GLORYS2V4 NBC transports have 23.9 ± 5.3 Sv and 25.0 ± 5.4 Sv, quite close to the *Schott et al.* (2005) and *Hummels et al.* (2015) observed NBC values of 25.8 ± 5.3 Sv and 26.8 ± 5.1 Sv, respectively. Although DA appears to bring the ORA NBC transports closer to the observations, the ORA NBC spread is still large with differences of more than 5 Sv between ORAP5 and GLORYS2V4. A more detailed investigation of the ORA transport discrepancies is described in Chapter 3.

The ORA deep western boundary transports at 11°S also agree well with the DWBC observational estimates, although their monthly variability is only half of the DWBC monthly variability measured by *Schott et al.* (2005) and *Hummels et al.* (2015) (Fig. 2.7b). The observed DWBC transport variability is consistently reproduced in the

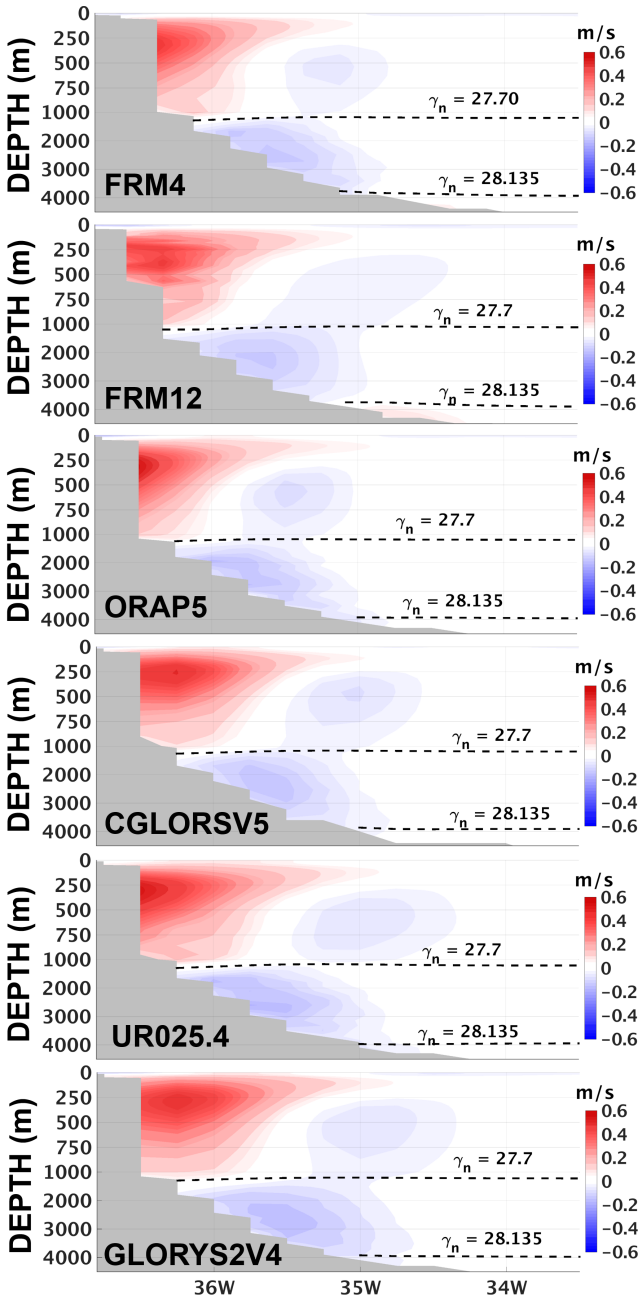

Figure 2.6: Zonal section at 11°S of the mean meridional velocity component (m/s) for the period 1997-2010. The horizontal dashed lines correspond to the depths of neutral densities, γ_n=27.70 $kg\ m^{-3}$ and γ_n=28.135 $kg\ m^{-3}$, used to separate the NBC and the DWBC layers as in *Hummels et al.* (2015). Note the stretched vertical axis between 0-1000 m, compared to 1000-5000 m.

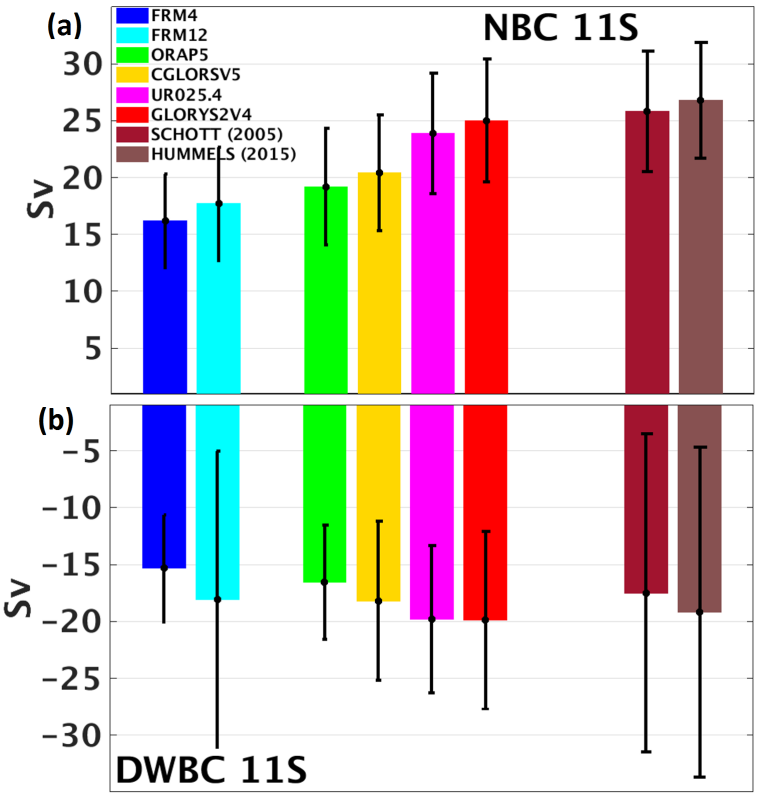

Figure 2.7: Transports (Sv) of the (a) NBC and (b) DWBC at 11°S calculated between the neutral densities interfaces shown by Fig. 2.6 and applying the same longitudinal limits as in *Schott et al.* (2005) and *Hummels et al.* (2015). The black bars represent the monthly variability of the NBC and DWBC transports.

FRM12, around ± 13 Sv, which also has a mean DWBC transport close to the ORAs and observational estimates.

In fact, FRM12 DWBC transports at 11°S surprisingly range from -50 to 13 Sv, which is similar to the observed DWBC range from -60 to 20 Sv in *Schott et al.* (2005) and *Hummels et al.* (2015). Some of the model products at 1/4° horizontal resolution, such as GLORYS2V4, can also show strong DWBC transports up to -50 Sv, but none of them reproduce a DWBC flow reversal, as shown by FRM12 and observations. These DWBC flow reversals are caused by the break-up of the DWBC into a series of anticyclonic eddies at ∼8°S (*Dengler et al.*, 2004), denoted by their positive temperature anomalies, which are clearly developed in the FRM12 (Fig. 2.8a) but not seen in

UR025.4 (Fig. 2.8b). Since FRM12 and UR025.4 are the only products with daily data available, Fig. 2.8 compares only these two in order to evaluate the DWBC eddies.

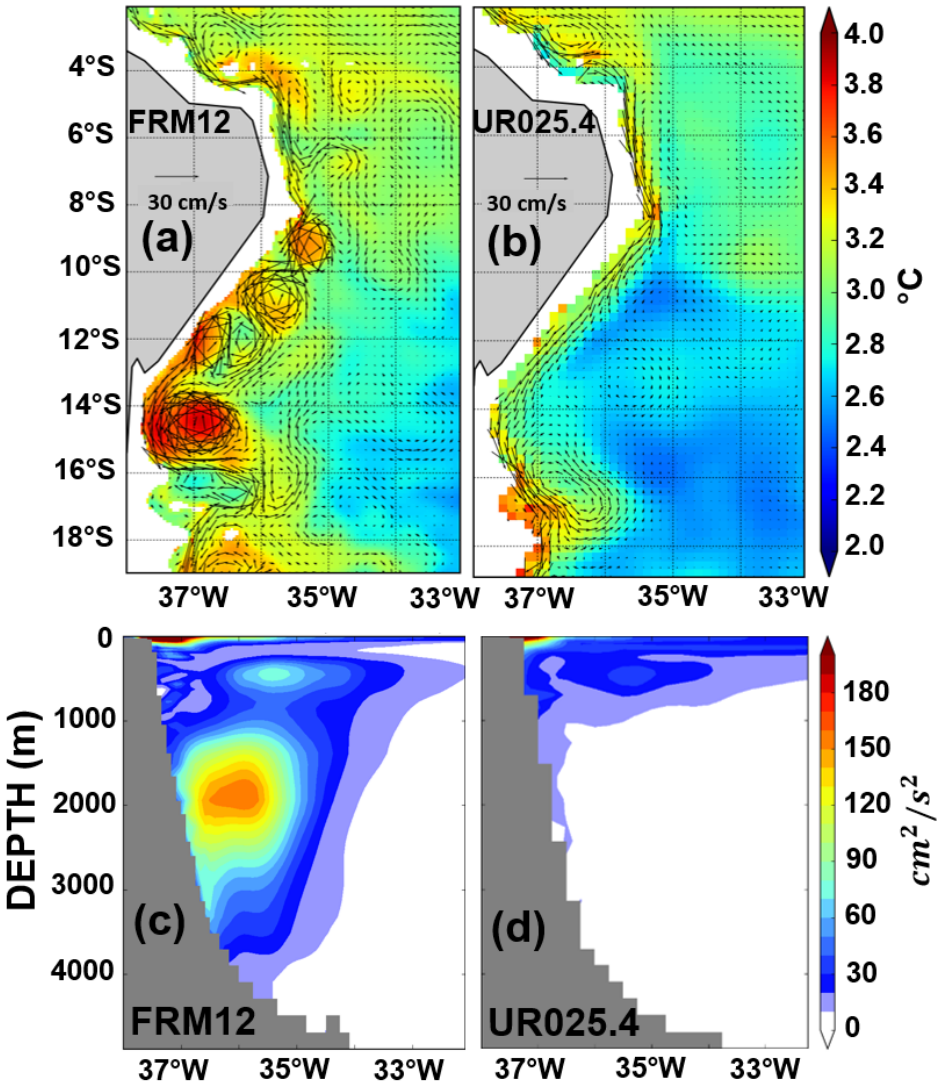

Figure 2.8: Current speed (cm/s) and temperature (°C) at 1900 m in 2000/01/05 for (a) FRM12 and (b) UR025.4 along the tropical South Atlantic western boundary. In (c) and (d) the FRM12 and UR025.4 EKE ($cm^{-2}\ s^{-2}$) are displayed at 11°S, respectively, calculated from daily means for the period 1997-2010.

Although Fig. 2.8a-b are snapshots of the currents at 1900 m, the DWBC eddies in FRM12 are continuously developed throughout the year, consistent with *Dengler et al.*

(2004). Fig. 2.8c shows a peak of Eddy Kinetic Energy (EKE) between 1500-2500 m in FRM12, which is calculated using daily means over the period 1997-2010. As expected by the laminar DWBC flow in UR025.4 (Fig. 2.8b), its EKE at the DWBC depth is negligible (Fig. 2.8d). This suggests that horizontal resolution may play a key role in the development of these DWBC eddies, and that the lack of observations in such deep regions prevents DA from constraining the ORA transport variability in the DWBC. *Garzoli et al.* (2015) suggest that there are two main pathways after the DWBC breaks down into a series of eddies at ∼8°S: the main portion of the NADW flow continues along the Brazilian continental shelf in the form of a strong reformed DWBC, while a smaller portion, about 22% of the initial transport, flows towards the interior of the basin. The DWBC eddies are thought to influence the NADW proportion that flows towards the interior of the basin (*Garzoli et al.*, 2015).

The ORAs also show consistent changes in the South Atlantic equatorial currents when compared to the FRMs (Fig. 2.9). The eastward SEUC is consistently intensified in the ORAs, reaching up to ∼0.25 m/s, whereas it is nearly absent in the FRMs. The ORA SEUC velocities are within the range of 0.2-0.4 m/s found by the observational study of *Molinari* (1982) and *Urbano et al.* (2008). Moreover, the westward eSEC and cSEC branches become stronger in the ORAs, particularly in ORAP5 and CGLORSV5. This intensified equatorial current system, shown by the ORAs, is directly related to their consistent interior transports, which are discussed in more detail in Chapter 3.

2.5 GloSea5 transports

Fig. 2.1 clearly shows that there are issues with GloSea5 transports in the southern Atlantic. The southward MHT in GloSea5 at 35°S is in striking contrast with the northward MHTs from other model products and observational estimates. In fact, GloSea5 misrepresents by far the southern Atlantic circulation. In Fig. 2.10, GloSea5 top-to-bottom transports, accumulated from west to east (as in Fig. 2.4), have a

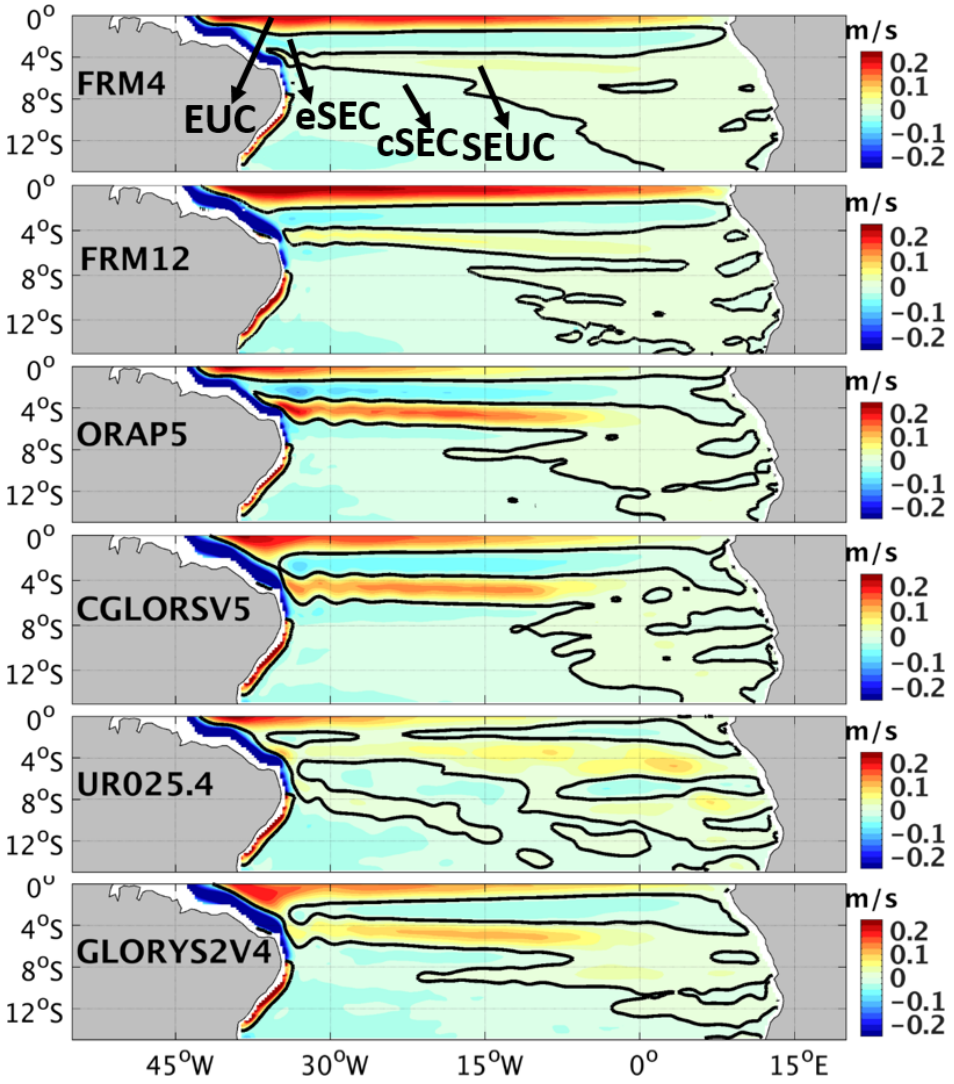

Figure 2.9: The 1997-2010 zonal velocity component (m/s) in the tropical South Atlantic between 100 and 500 m. The black contour corresponds to 0 m/s. The arrows in the top figure indicate the equatorial currents as shown by the *Stramma and Schott* (1999) schematic for the same depth range.

strong signature of the northward MC in the western boundary, which is not seen in the XBT-AX18 transects. This northward flow reaches up to ∼70 Sv in GloSea5 and is counteracted by a very strong BC, which abruptly reduces the accumulated transports in more than 100 Sv (i.e. from 70 Sv to -40 Sv) by 48°W. The interior flow also seems to be affected by the very strong dynamics in the GloSea5 western boundary, showing a second smaller peak east of 48°W in the accumulated transports.

The misrepresentation of the Brazil-Malvinas confluence in GloSea5 is clearly seen in the 1997-2010 SSH maps of Fig. 2.11. The low SSHs representing cold MC waters extend to ∼30°S in GloSea5, much further north than AVISO SSHs indicate.

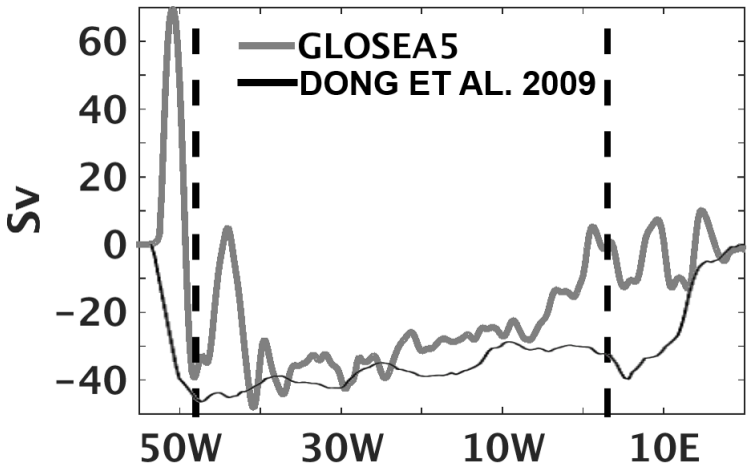

Figure 2.10: Top-to-bottom transports (Sv) at 35°S accumulated from west to east for GloSea5 and XBT-AX18 measurements as in Fig. 2.4.

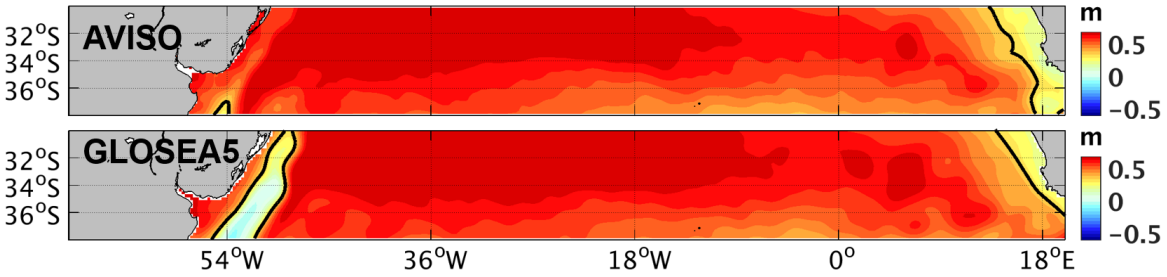

Figure 2.11: The 1997-2010 SSH (m) in the southern Atlantic for AVISO and GloSea5. The solid black line represents the contour of 0.3 m. The offset of the model SSHs with respect to AVISO is removed to allow a better comparison of the mean circulation features.

At 11°S, GloSea5 has substantially weak western boundary circulations with both the NBC and DWBC cores showing smaller velocity magnitudes (Fig. 2.12) when compared to the ORAs and FRMs (Fig. 2.6). GloSea5 NBC and DWBC transports at 11°S are only ∼10 Sv and -7 Sv, respectively, which are much weaker than the lowest FRM4 NBC and DWBC transports in Fig. 2.7. Finally, GloSea5 also shows very unusual circulation patterns near the equator (Fig. 2.13) with respect to all other

model products (Fig. 2.9). Its eSEC is so strong that develops westward flow in the latitudes where the eastward EUC flow should dominate, according to all the other model products and *Stramma and Schott* (1999).

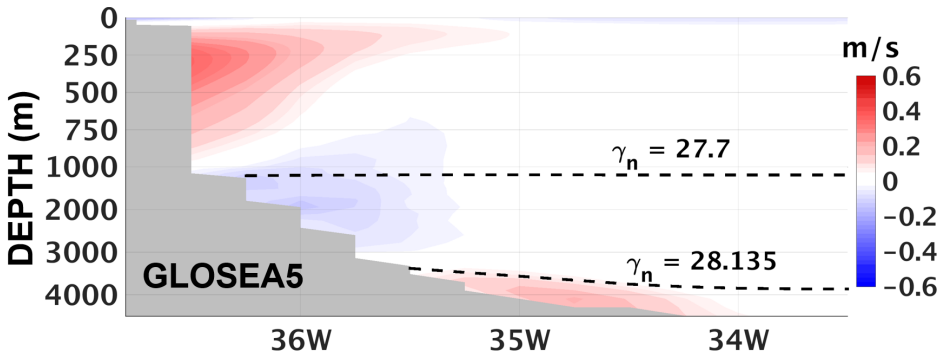

Figure 2.12: Zonal section at 11°S of the 1997-2010 meridional velocity component (m/s) for GloSea5. Note the stretched vertical axis between 0-1000 m, compared to 1000-5000 m.

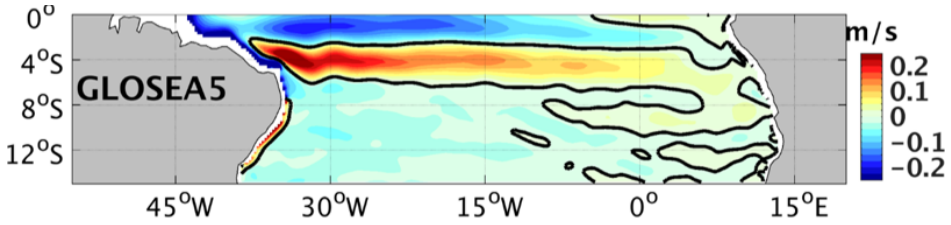

Figure 2.13: The 1997-2010 zonal velocity component (m/s) in the tropical South Atlantic between 100 and 500 m for GloSea5. The black contour corresponds to 0 m/s.

In order to better investigate what may be the causes for such discrepant GloSea5 transports with respect to the other model products, the Atlantic meridional transports in GloSea5 are evaluated over time, from its first year available in 1989 until 2010 (Fig. 2.14). The GloSea5 product, which employs the current MetOffice ocean 3D-Var DA system, is compared to the UR025.4 reanalysis, which is based on an older version of the MetOffice operational system with an Optimal Interpolation DA method (Tab. 2.1). The comparison between these two ORA products can give some insights about when GloSea5 transports start to drift and the latitudes where they have the largest discrepancies.

Figure 2.14 clearly shows that the GloSea5 transports begin to drift between 1992

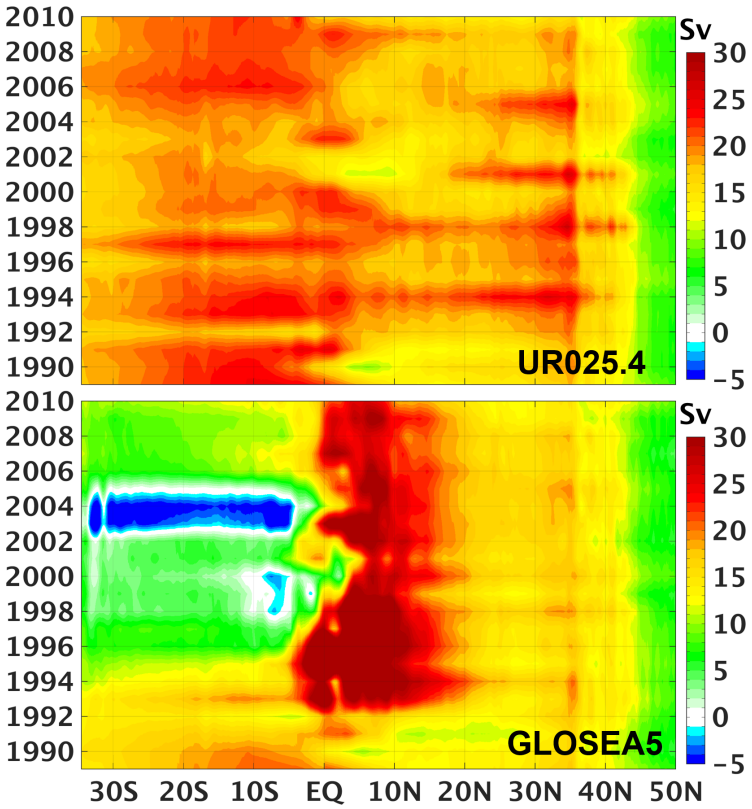

Figure 2.14: The annual AMOC strength (Sv) in UR025.4 and GloSea5.

and 1993 with AMOC peaks of more than 30 Sv in the equatorial region. The development of this very strong equatorial AMOC after 1992 in GloSea5 is followed by an abrupt AMOC decrease in the South Atlantic from 1995 onwards, explaining the weak GloSea5 circulation at 35°S (Fig. 2.1a) and 11°S (Fig. 2.13). GloSea5 SAMOC strength even becomes negative from 2003 to 2005, giving the southward MHT in Fig. 2.1b. The anomalous GloSea5 transports south of ∼20°N remain as a persistent feature over time, even after the beginning of the Argo period in the 2000s.

The GloSea5 transport issues are perhaps surprising as *Jackson et al.* (2016) show that this ORA closely matches the RAPID array at 26.5°N, accurately capturing the northern AMOC interannual variability and decadal trends. The RAPID array measurements extend from 2004 to present, but UR025.4 ends in 2010. In the overlapping period from 2004 to 2010, GloSea5 and UR025.4 AMOC strengths at 26.5°N are 16.10

± 3.4 Sv and 18.30 ± 4.3 Sv, respectively, both quite close to the 2004-2010 RAPID array estimates of 17.20 ± 3.8 Sv.

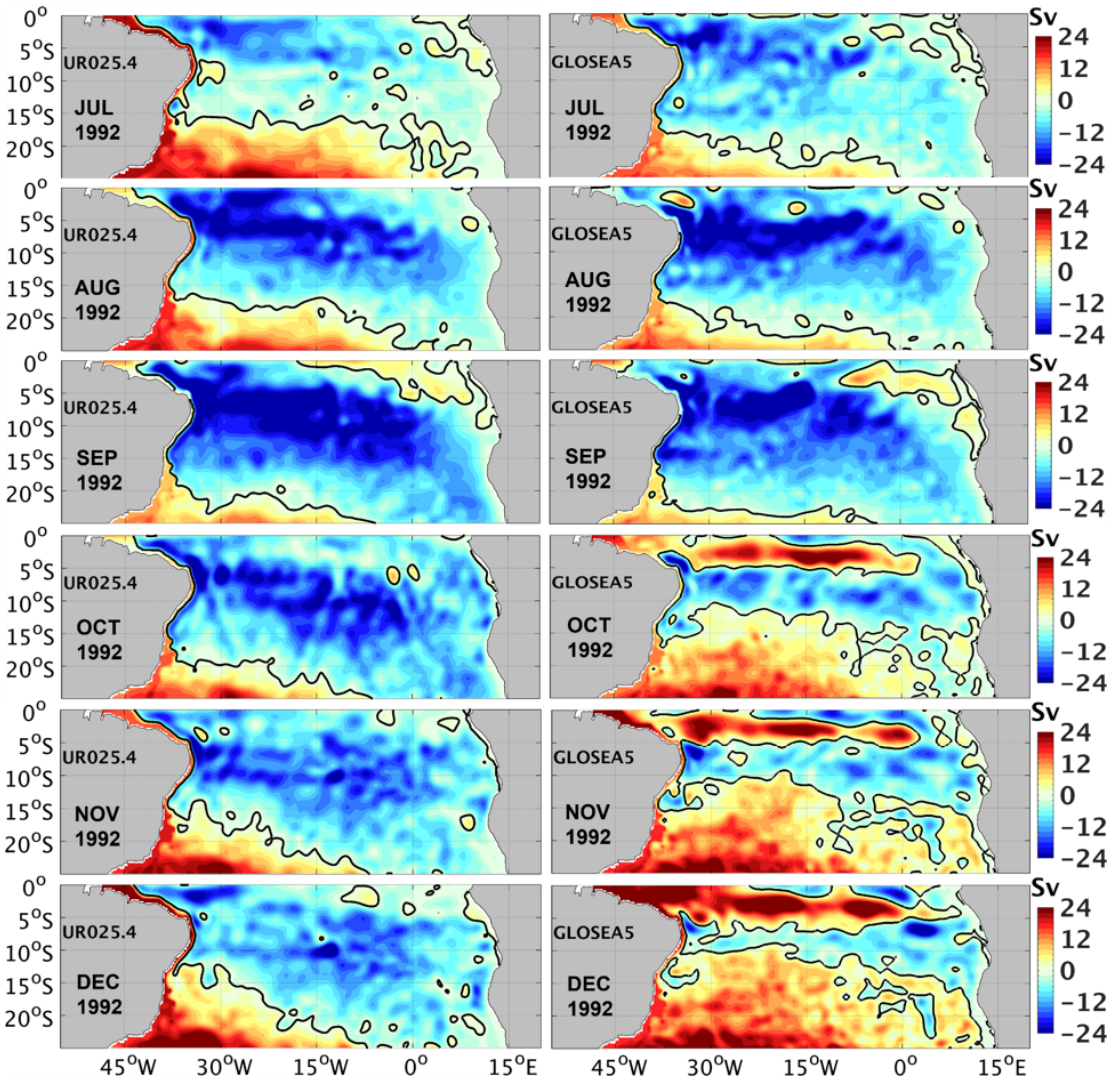

Figure 2.15: The monthly east-west accumulated meridional transports (Sv) from the surface down to z_{max} at each latitude. The solid black contour corresponds to 0 Sv.

The east-west accumulated transports from the surface down to z_{max} are evaluated on a monthly basis from July to December 1992 in the tropical South Atlantic (Fig. 2.15). Both UR025.4 and GloSea5 show very similar east-west accumulated transports in the basin interior until September 1992. Although Fig. 2.15 only covers the last half of 1992, the transport agreements in the basin interior between UR025.4 and GloSea5

go back to their first month in January 1989. GloSea5 transports begin to drift in October 1992, precisely the month when altimetry observations are introduced into the DA system (*Blockley et al.*, 2014; *Jackson et al.*, 2016). A clear latitudinal band of very strong northward transports between 5°S and the equator develops in GloSea5 after October 1992, consistent with the unusual circulation patterns near the equator shown by Fig. 2.13. Unlike Glosea5, UR025.4 interior transports in the equatorial South Atlantic do not show any abrupt changes after October 1992.

The monthly net accumulated transports of UR025.4 and GloSea5 at the western boundary from Fig. 2.16, which are equivalent to the overturning strength, are shown for the tropical South Atlantic from September to December 1992. Consistent with Fig. 2.14 and Fig. 2.15, the overturning strength in GloSea5 begins to drift in October 1992 near the equator (Fig. 2.16), reaching almost 60 Sv by December 1992 (i.e. 40 Sv stronger than UR025.4).

2.6 Discussion and Conclusions

The South Atlantic circulation at 35°S and in the western boundary at 11°S were evaluated for a global NEMO-based dataset of five ORAs and two FRMs with distinct spatial resolutions. The ORAs mainly differ by their initial conditions, their DA schemes and to some small extent by the observations assimilated, as they share very similar ocean model configurations and are all forced with the ERA-Interim atmospheric product (Tab. 2.1).

Comparisons with hydrographic measurements and observational studies, at both 35°S and 11°S, show that most of the ORAs reproduce more realistic large-scale and western boundary transports than the FRMs. For example, ORAs show much stronger SAMOCs and MHTs than the FRMs (Fig. 2.1), including: a better representation of boundary and interior transports at 35°S, consistent with the XBT-AX18 estimates (Fig. 2.3); an improved positioning of the mean oceanic fronts, such as the Brazil-

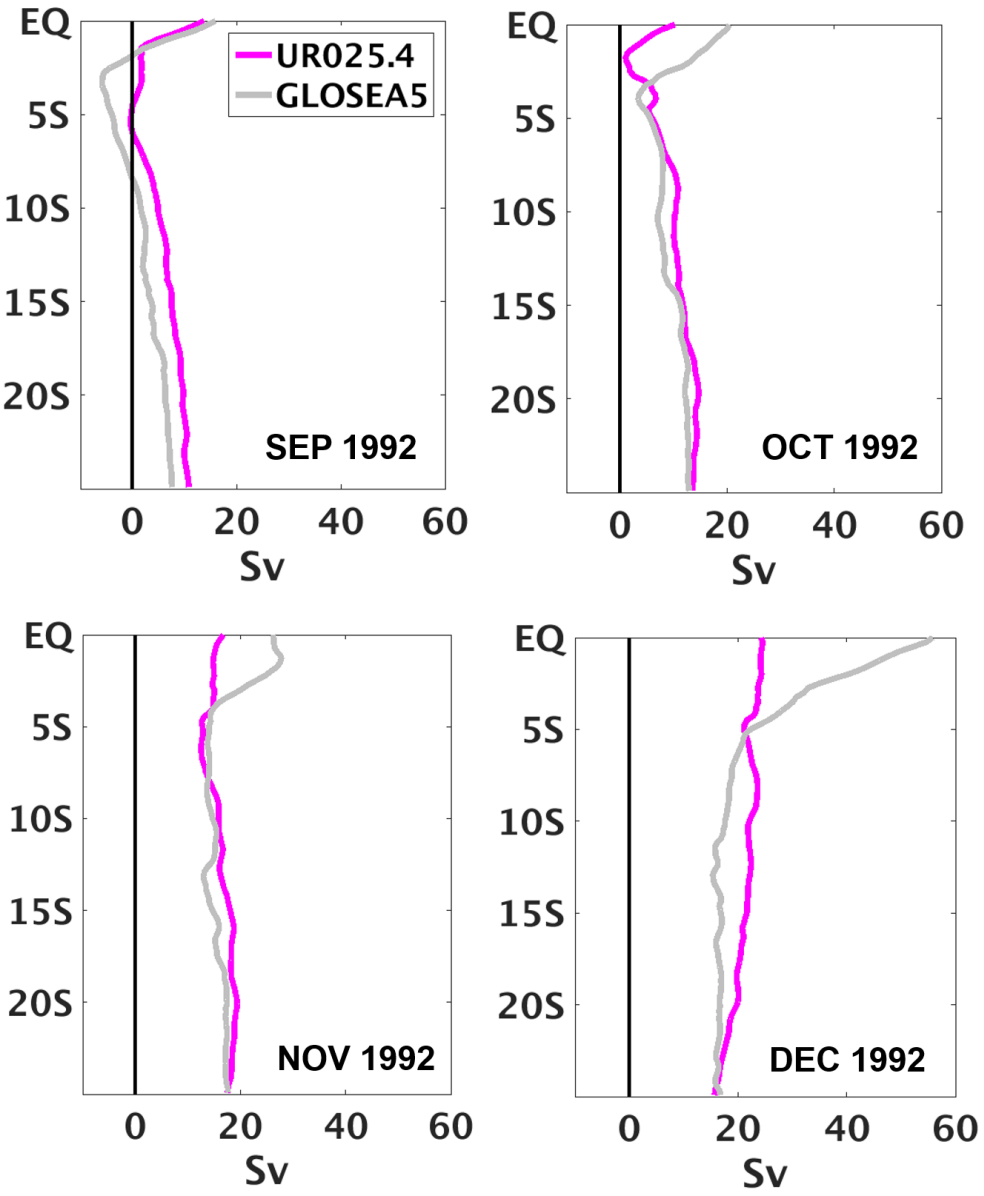

Figure 2.16: UR025.4 and GloSea5 monthly AMOC strengths (Sv) from September to December 1992 for the tropical South Atlantic.

Malvinas confluence (Fig. 2.5), as well as an improved representation of the south equatorial currents (Fig. 2.9); and the ORAs have more consistent mean NBC-DWBC transports when compared to western boundary measurements at 11°S (Fig. 2.7), although the ORA spread of the NBC transports is still large. The limitations of DA in constraining the western boundary ORA transports are discussed in more detail in

Chapter 3.

The eddy-permitting model products, including all the ORAs, were not able to correctly reproduce the DWBC variability, such as the DWBC flow reversals due to the development of deep eddies. In contrast, the DWBC variability in the high resolution FRM12 shows the successful development of DWBC eddies (Fig. 2.8). This suggests that horizontal resolution plays a role in the DWBC eddy development. A high-resolution model will better represent coastline orientation changes, the sloping bathymetry near the coast and the shear between the NBC and DWBC (e.g *Soutelino et al.*, 2013; *Dengler et al.*, 2004; *Garzoli et al.*, 2015). These elements can help trigger barotropic and baroclinic flow instabilities, as suggested by *Dengler et al.* (2004), as the causes for the DWBC eddy generation. The lack of observations in such deep regions can also prevent DA from constraining the ORAs in the DWBC.

Finally, although GloSea5 is considered a reference product for the North Atlantic circulation (*Jackson et al.*, 2016), here we show that this ORA has anomalous transports south of ∼20°N (Fig. 2.14), which begin to drift with altimetry assimilation in October 1992. According to *Blockley et al.* (2014), an altimeter bias correction technique is employed to correct biases in the GloSea5 MDT, which is added to the SLA observations prior to assimilation. Since GloSea5 misrepresents the South Atlantic circulation by far, including the Brazil-Malvinas confluence, the NBC-DWBC and the equatorial currents, its inconsistent transports may be derived from how the model MDT biases are treated in GloSea5, particularly south of ∼20°N. Bias-correction strategies could be revisited in the previous MetOffice DA system, employed in UR025.4, in order to better evaluate any sources of error within the newer DA system. For this reason, GloSea5 is excluded from the following ORA analyses in Chapters 3 and 4.

CHAPTER 3

SOUTH ATLANTIC MERIDIONAL HEAT AND VOLUME TRANSPORTS

3.1 Introduction

The South Atlantic acts as a communicator between the southern and northern oceans (*Garzoli and Matano*, 2011) through the AMOC transporting warm water northward across the Equator to compensate for the southward export of a cold NADW. The northward upper limb of the SAMOC is a complex mixture of water masses originating from the Indian, Pacific, and Southern oceans, which are blended together in the South Atlantic gyre circulations. The water mass redistribution in the South Atlantic and the inter-ocean exchanges can significantly influence the long-term AMOC variability (*Garzoli and Matano*, 2011), particularly on decadal timescales through the heat and salt export by the Agulhas leakage (*Weijer et al.*, 2002; *Sebille et al.*, 2011).

Marshall et al. (2013) argue that the northward ocean heat transport across the Equator sets the mean position of the ITCZ in the Northern Hemisphere. Since the South Atlantic is the only major ocean basin that transports heat equatorward, quantifying and understanding the SAMOC should help to explain the inter-hemispheric heat exchanges and improve interannual to decadal climate simulations, as also recently rein-

forced by *Lopez et al.* (2016). For this reason, a SAMOC observing system was already initiated in 2002 with quarterly high-density XBT lines at 35°S (*Garzoli and Baringer*, 2007) and more recently with the development of SAMBA array (*Ansorge et al.*, 2014), analogous to the RAPID array in the North Atlantic (*Cunningham et al.*, 2007). However, the lack of long-term measurements in the area still limits our understanding of the South Atlantic state and its variability, reflecting the large disagreement in the transports between observational and model studies (*Garzoli et al.*, 2013; *Dong et al.*, 2014; *Dong et al.*, 2015; *Majumder et al.*, 2016; *Stepanov et al.*, 2016).

In this context, ORAs could be useful tools to monitor ocean circulation and change indicators (*Masina et al.*, 2015; *Palmer et al.*, 2015). ORAs employ ocean general circulation models and DA schemes to synthesize a diverse network of available ocean observations in order to arrive at a consistent estimate of the historical ocean state. ORA diagnostics have been put together with three-dimensional velocity fields constructed from Argo and SSH observations to study the SAMOC variability and its relation with the MHTs between 35 and 20°S (*Majumder et al.*, 2016). Although both observations and ORAs show strong correlations between the SAMOC and MHT, *Majumder et al.* (2016) also found significant discrepancies in the heat transport magnitudes among the ORAs and between the ORAs and the observations. Their result reveals the need for further assessment of the skills and uncertainties of the ORAs in the South Atlantic, such as comparing them with FRMs and evaluating their SAMOC contributions across the eastern, interior, and western boundary regions shown in Fig. 1.5 and Fig. 1.4.

The next generation of operational climate prediction systems will implement eddy-permitting ocean models, and it is expected that ORAs will provide improved initial conditions for such climate prediction models. The comparison between ORAs and FRMs is a critical step in assessing the feasibility of initialising the ocean transports which are not directly observed. Such intercomparisons therefore can give valuable insights about how the transports are affected by DA (e.g. *Zuo et al.*, 2011; *Karspeck et al.*, 2015). To address these issues, we use state-of-the-art ORAs at eddy-permitting

resolution with two FRMs at eddy-permitting and eddy-resolving resolutions to study the meridional transports in the South Atlantic between 35°S and the equator. Focusing on the meridional volume and heat transports, we first identify similarities and differences among products. Going further than *Majumder et al.* (2016), we also narrow down these transport differences in an attempt to understand the potential impact (and limitations) of the DA schemes in improving the ORA states in the South Atlantic.

This chapter is organised as follows. Sections 3.2 and 3.3 show the results of the meridional transports and the contributions of the temperature and meridional velocities to the spread in the heat transports, respectively. Section 3.4 evaluates the western boundary role in the South Atlantic large-scale transport discrepancies between the products. Section 3.5 investigates the time variability of the transports. Finally, Section 3.6 contains the discussion and conclusions.

3.2 Meridional transports

Figure 3.1a shows the time mean AMOC strength for each product and at each latitude from 35°S to 60°N. The ensemble spreads of ψ_{max} for all products (ENS-ALL) and for only the ORAs (ENS-ORA) are shown in Fig. 3.1b. The discrepancies in AMOC strength between the ORAs are largest in the South Atlantic, reaching the maximum spread of 3.5 Sv (ENS-ALL) and 3 Sv (ENS-ORA) in the area between 20°S and the equator. The two FRMs are similar to each other, both with relatively low AMOC across the basin. The assimilation of observations in the reanalyses appears to increase the AMOC strength at all latitudes, which is supported by the previous analyses in Chapter 2. In the North Atlantic, especially in the subpolar gyre north of ∼35°N, the ORA AMOCs are consistently 3-4 Sv higher than in the FRMs. However, the increase of the ORA AMOCs is less consistent south of ∼35°N, especially in the South Atlantic where the differences in the SAMOC transports can reach up to ∼8 Sv between GLORYS2V4 and ORAP5. The latter is the ORA that has the lowest transports in

the South Atlantic, closest to the FRMs.

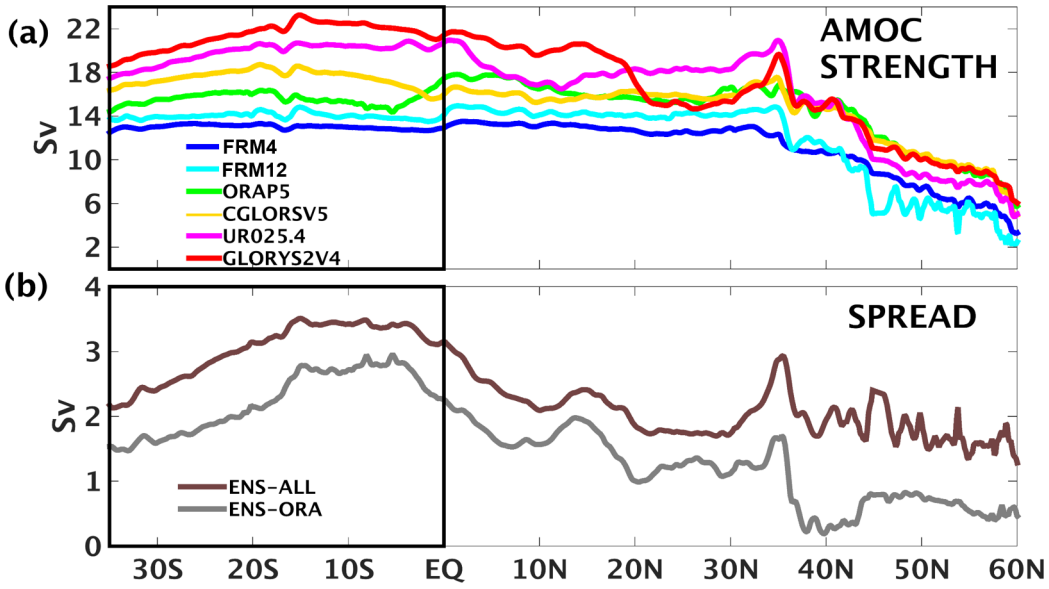

Figure 3.1: (a) The AMOC strength (Sv) averaged over 1997-2010 as a function of latitude, and (b) its spread (Sv) defined as the spread of the ENS-ALL and ENS-ORA. The black box highlights the South Atlantic.

As in the AMOC strength (Fig. 3.1), the inter-product spread in the South Atlantic MHT gets larger towards the equator, with differences up to 0.4 PW between GLORYS2V4 and ORAP5 (Fig. 3.2). The MHT based on integrating the *Liu et al.* (2015) surface heat flux product southward of 80°N is also considered. This product uses top of atmosphere net radiation flux from the Clouds and Earth's Radiation Energy System modified by the ERA-Interim atmospheric transports. The MHT from *Liu et al.* (2015) suggests higher heat transports in good agreement with UR025.4 and GLORYS2V4 across the South Atlantic basin, although the surface integration method accumulates errors from all higher latitudes. *Liu et al.* (2015) estimates also reasonably agree with the XBT-AX18 and other South Atlantic observational studies at 35°S and 30°S. However, the observational estimates diverge north of 30°S, with the transports from *Dong et al.* (2015) and *Majumder et al.* (2016) differing by ∼0.7 PW at 20°S. These discrepancies underscore the uncertainties in observed transports through the South Atlantic.

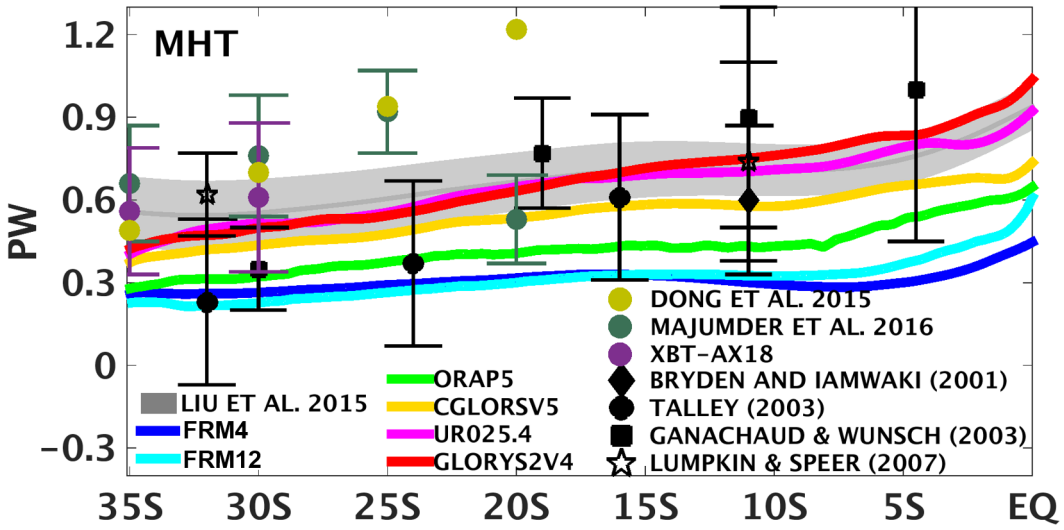

Figure 3.2: MHT (PW) as a function of latitude averaged over 1997-2010. The MHT from *Liu et al.* (2015) and its annual standard deviation is represented by the shaded grey area. The products are also compared to hydrographic and inverse modelling estimates from the literature at several latitudes.

Figure 3.3a-f show maps of the 1997-2010 east-west accumulated volume transports from the surface down to z_{max} (typically ∼1200 m) for each latitude, same approach used in Fig. 2.15. These contours can be regarded as streamlines of the upper ocean gyre circulations. The northern boundary of the subtropical gyre (dashed contour of zero transport), near 20°S and 15°S, agrees well between products, with only GLORYS2V4 extending slightly further north. The subtropical gyre to the south is only partially shown but the strength of this gyre is quite consistent between the ORAs and FRM12, and significantly stronger than in FRM4. The large-scale circulation equatorward of 15°S is dominated by a southward flow increasing westwards until the strong northward NBC flow is reached in a very narrow western boundary area. The ORA southward flow in the basin interior ranges between -14 and -18 Sv. For consistency with the overturning strength ψ_{max} (represented in Fig. 3.3a-f by the westernmost accumulated transports), the NBC region typically reaches ∼36 Sv of northward flow. This agrees with other studies of the role of the NBC in the AMOC upper branch crossing the equatorial Atlantic (e.g. *Rabe et al.*, 2008; *Sebille et al.*, 2011; *Rühs et al.*,

2015).

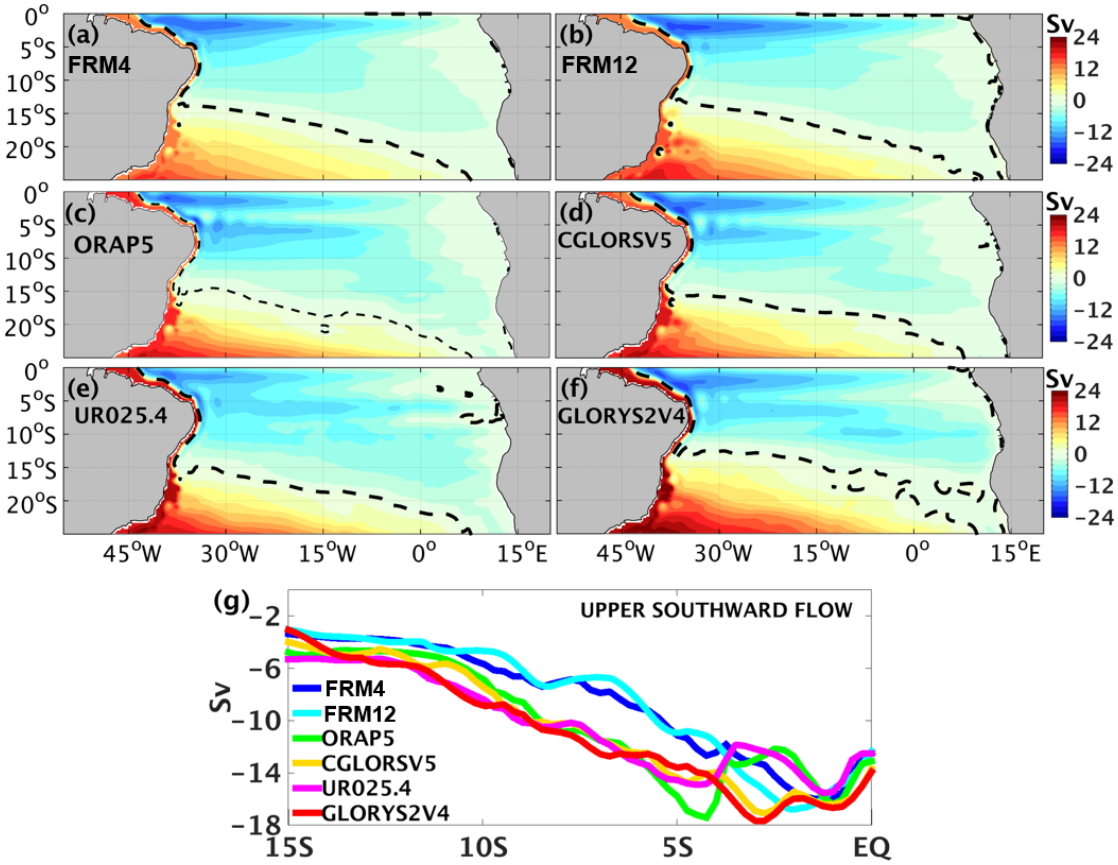

Figure 3.3: (a) East-west accumulated volume transports (1997-2010) for each product (a to f) calculated from the surface down to z_{max} at each latitude. The upper southward flow in (g) is defined by the southward maximum of the east-west accumulated volume transports. Units are in Sv and the black dashed contour corresponds to 0 Sv.

Figure 3.3g shows the southward maximum of the east-west accumulated transports between 15°S and the equator. The generally good agreement of this interior component of the circulation between the ORAs is in striking contrast with their ψ_{max} (Fig. 3.1). Indeed the ENS-ORA spread of the interior flow (∼1 Sv) is about three time less than the spread in ψ_{max} for the same latitude range. The ORA southward transports differ from the FRMs, with two peaks of southward transport between 10°S and the equator where the FRMs only have one. The zonal currents, which are shown by Fig. 2.9 and can be inferred in Fig. 3.3, reveal consistent changes in the equatorial current system

between the ORAs and the FRMs. The cSEC branch, described in the top 500 m tropical circulation schematics of *Stramma and Schott* (1999), is nearly absent in the FRMs, but more evident in the ORAs, also leading to stronger southward transports in Fig. 3.3g. Thus, there is both qualitative and quantitative evidence that the DA in the ORAs is doing a good job in reproducing a consistent interior circulation for the tropical South Atlantic basin.

Despite evidence of the ORA consistency in the interior circulation in the tropical South Atlantic as well as in the subtropical gyre further south, the overturning transport component ψ_{max}, associated with the very narrow NBC, is not as well constrained (Fig. 2.7). Although DA brings the ORA NBC transports closer to the observations when compared to the FRMs, Fig. 2.7a also shows that the ENS-ORA NBC spread is still large, around 3 Sv, which is consistent with the ENS-ORA spread in the SAMOC strength (Fig. 3.1). This suggests that, at least in this latitude range, the NBC strength alone can explain the large-scale transport discrepancies between the ORAs, which will be discussed in more detail in Section 3.4.

3.3 Temperature and velocity contributions

In this section, the contributions from T and v variability for the heat transports are analysed, as well as the relationship between the MHT and the SAMOC upper limb. Figure 3.4 shows a meridional section of the zonal-mean temperatures from WOA13 (*Locarnini et al.*, 2013), together with zonal-time mean anomaly T from each product. Large anomalies in the FRMs can be seen, particularly in the tropics where the models may have limitations representing sharp vertical gradients in the tropical thermocline. In FRM4 there is a large warm anomaly of up to 3°C in the upper 200 m of the tropical South Atlantic, whereas FRM12 has a weaker warm anomaly in the top 200 m, but a much more extensive cold anomaly of ∼2°C in the ocean interior down to ∼500 m. All the ORAs show much weaker anomalies (mostly <0.5°C), presumably due to the

assimilation of SST and T/S profiles which are able to better constrain the T vertical structure. Below 1200 m the differences between the products and WOA13 are much smaller.

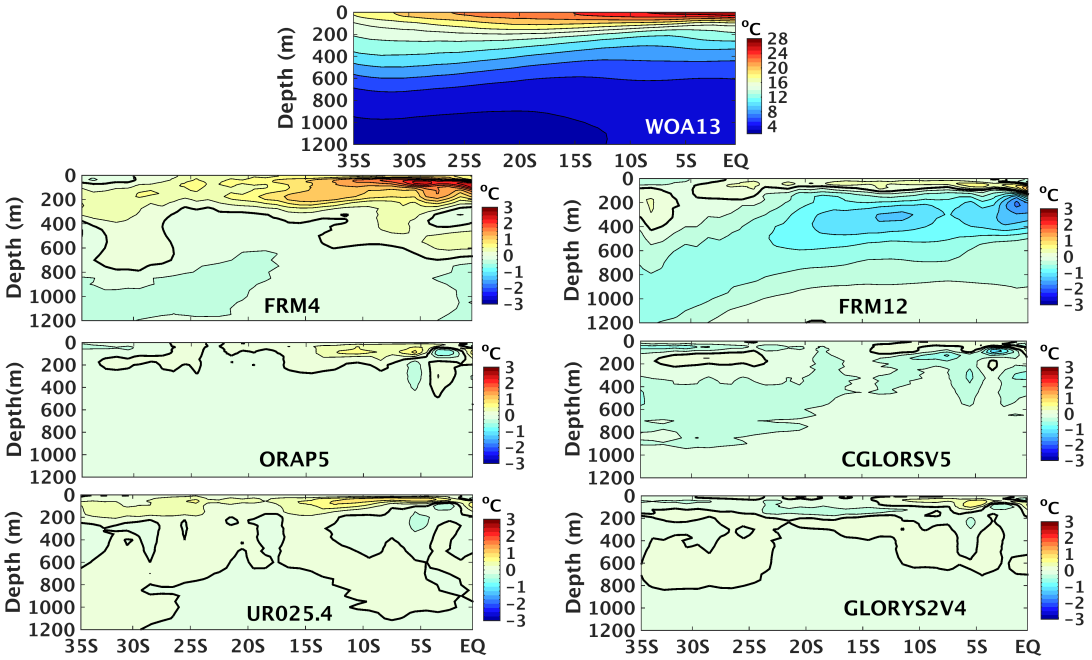

Figure 3.4: The zonal averaged temperature (°C) as a function of latitude for WOA13 from 1995 to 2012 (top panel), followed by the zonal averaged temperature of each product from 1997-2010 minus WOA13. The thick solid line represents the 0°C contour.

Figure 3.5 evaluates the relative T and v contributions to the ENS-ALL MHT spread. We compare the original MHTs (Fig. 3.5a) with the MHTs based only on circulation differences ($v\overline{T}$; Fig. 3.5c), and only on temperature differences ($\overline{v}T$; Fig. 3.5e), where the overbar denotes the ENS-ALL mean. In order to identify locations where T and v contribute to different transports in ENS-ALL, ocean temperature transports per 0.25° of longitude (p-OTTs) from top to bottom are also calculated across the basin (Fig. 3.5b), with their p-$v\overline{T}$ (Fig. 3.5d) and p-$\overline{v}T$ (Fig. 3.5f) contributions. Note that the units in the maps of Figs. 3.5b, d, f are PWT (PetaWatt Temperature Transport; *Talley*, 2003; *Macdonald and Baringer*, 2013) per 0.25°. The spatial discretisation of the MHT on a longitudinal 0.25° grid allows to present FRM12 on a comparable scale to that of the other models.

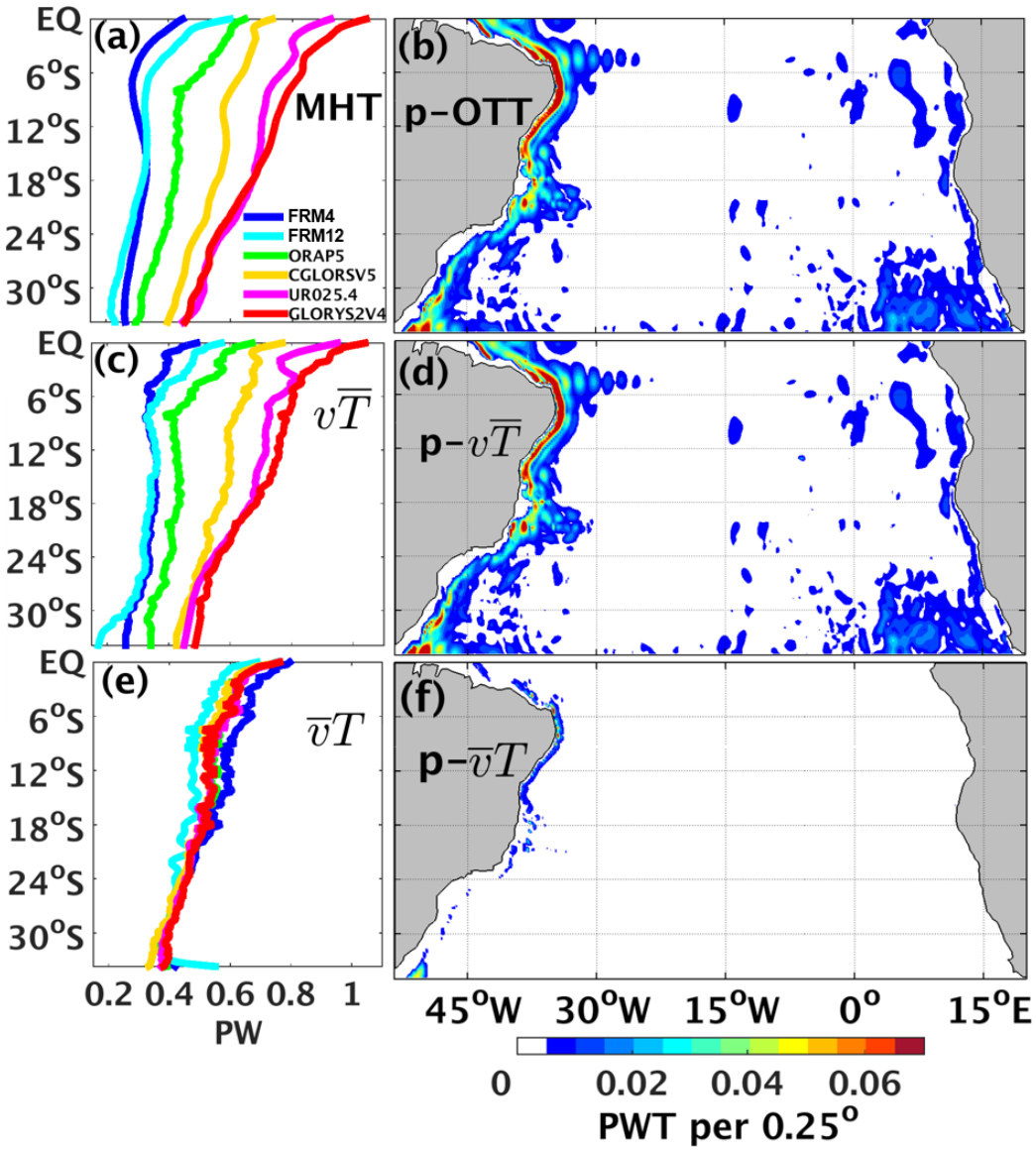

Figure 3.5: (Left) The original MHTs (a), the MHTs based on the $v\overline{T}$ component (c), and the MHTs based on the $\overline{v}T$ component (e) in PW. (Right) The ENS-ALL spread of the p-OTTs (b), p-$v\overline{T}$ (d) p-$\overline{v}T$ and (f) in PWT per 0.25°. Overbar represents the mean of the ENS-ALL.

The strong similarity between Figs. 3.5a-b and Figs. 3.5c-d reveals that v rather than T differences drive the inter-product spread in the MHTs, both regionally and in the zonal integrals. The $v\overline{T}$ component captures variations from ∼0.2 PW to 1 PW (Fig. 3.5c), explaining ∼83% of the total MHT spread which is mainly concentrated

in the areas with largest mean transports, i.e. the narrow western boundary region (Fig. 3.5d). Even with relatively large T anomalies found in the FRMs (Fig. 3.4), the $\overline{v}T$ component only differs by ∼0.13 PW between the products across the basin (Fig. 3.5e), mainly due to temperature differences in FRM4 and FRM12. However, a very narrow maximum of p-$\overline{v}T$ (Fig. 3.5f) can also be seen right against the western boundary, especially in the NBC region around 11°S and near the Brazil-Malvinas Confluence at 35°S. This is interpreted as due to variations in boundary temperatures needed to geostrophically support the large differences in western boundary current velocities between the products. However, these temperature differences make little transport contribution. The detailed role of the western boundary for the inter-product transport discrepancies will be discussed again in Section 3.4.

The dominance of the circulation determining heat transports also extends to the time variability. The monthly correlation between ψ_{max} and MHT within all products is above 0.8 for most of the South Atlantic (Fig. 3.6). *Dong et al.* (2009) and *Garzoli et al.* (2013) estimated quarterly correlation values around 0.75 between circulation and heat transports at 35°S from the XBT-AX18 observations. *Majumder et al.* (2016) found that a 1 Sv change in the SAMOC strength corresponds to a change of 0.046 PW at 35°S and 0.056 PW at 20°S in the MHT. This agrees relatively well with the ENS-ORA which show a 1 Sv change in SAMOC strength corresponds to ∼0.052 PW change between 35°S and 20°S. It is interesting to note that correlations abruptly fall from 0.85 to ∼0.45 near the equator. The interior southward flow gradually increases in the tropical South Atlantic reaching similar magnitudes to ψ_{max} between 5°S and the equator (Fig. 3.3g). In this region, the temperature differences between the NBC core and the southward basin interior circulation reach up to ∼5.5°C in the top 300 m, similar to the ΔT of ∼6.5°C between the SAMOC upper and lower limbs. Therefore it is likely that these large upper level tropical circulations explain why ψ_{max} does not dominate the MHT variability close to the equator, as also noted by *Valdivieso et al.* (2014).

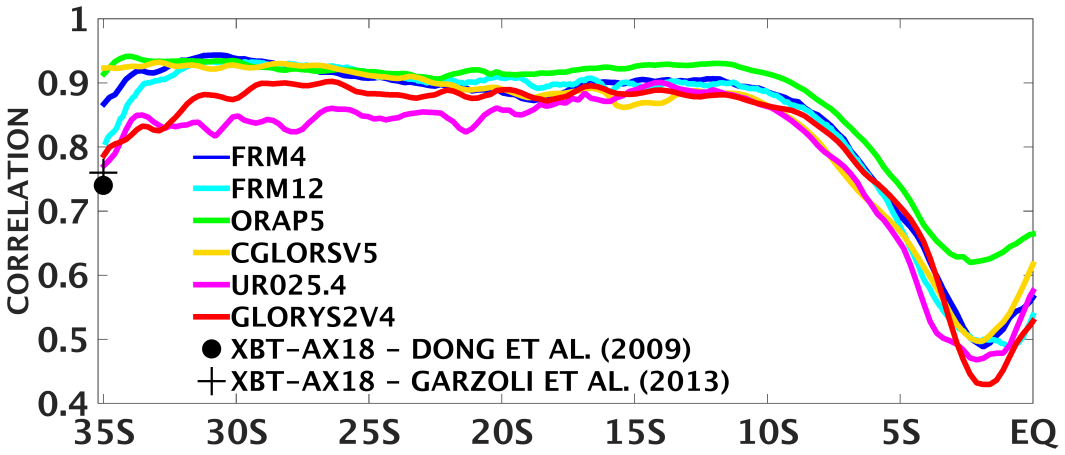

Figure 3.6: The monthly Pearson correlation between the SAMOC strength and the MHT as a function of latitude for 1997-2010, calculated with significance level of 95%. The quarterly XBT-AX18 correlation between the SAMOC strength and MHT at 35°S is also included for comparisons.

3.4 Western boundary contribution

Figure 3.7 shows the linear regression coefficient between the inter-product p-OTTs and their MHTs across the whole basin. The western boundary grid points in the tropical South Atlantic reach up to ∼0.4 PWT per 0.25°, out of 1 PW across the whole basin, so that ∼40% of the differences in the MHT can be explained by transports in a 0.25°-wide band (a single grid point in all models except FRM12), with values elsewhere in the basin interior very close to zero. This is consistent with Fig. 3.3 showing that the large-scale southward flow at upper levels does not differ much between products, while ψ_{max} varies considerably, mainly due to the narrow NBC. Weaker negative linear regression coefficients are found eastward of the NBC in Fig. 3.7, representing the influence of the southward DWBC, reflecting the sloping bathymetry and the broader current scale than the NBC. South of 25°S the p-OTT contributions to the total MHT are more distributed, with a noticeable contribution from the Agulhas leakage caused by the different intensity and positioning of the Agulhas rings between the products as they travel westward across the southern Atlantic (Fig. 2.5).

Figure 3.7 also shows a continuous and dominant narrow band of positive regression

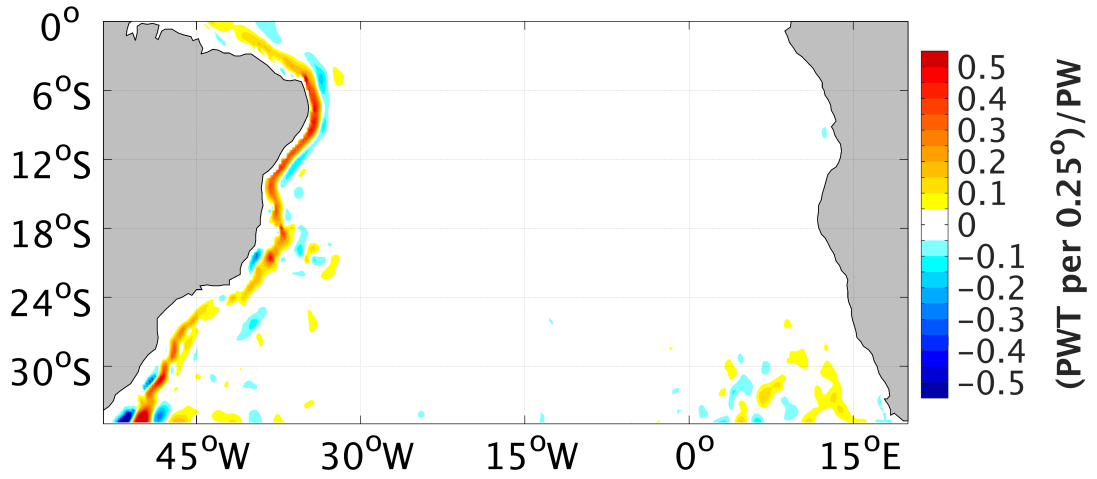

Figure 3.7: The linear regression coefficient between the inter-product p-OTTs and their MHTs for each latitude. Units are in PWT per 0.25° per 1 PW across each latitude.

coefficients all down the western boundary, including latitudes where the p-OTTs have a southward transport associated with the BC, e.g. between 35°S and 25°S (see schematic of Fig. 1.5). This reveals that products with larger northward MHTs (e.g. CGLORSV5, UR025.4 and GLORYS2V4) must have weaker southward p-OTTs near the western boundary, i.e. a weaker BC, resulting in the positive MHT linear regressions. In the case of CGLORSV5, UR025.4 and GLORYS2V4, this is reinforced by a stronger northward subsurface transport of the IWBC and NBUC, which feeds the NBC in the tropical South Atlantic (Fig. 3.8a and Fig. 3.8b). Based on Fig. 3.7, a region within 6° of the coast is selected to calculate the TW, SACW and AAIW transports of the upper western boundary circulation, with their isopycnal limits defined as in *Mémery et al.* (2000) and *Donners et al.* (2005). For each latitude, any southward water mass transport is accounted for as the BC (Fig. 3.8a), whereas any northward transport contributes to the IWBC-NBUC-NBC system (Fig. 3.8b), allowing to represent the deepening of the poleward BC and the shallowing of the equatorward IWBC-NBUC-NBC flows, as shown by Fig. 1.5 (*Soutelino et al.*, 2013).

In GLORYS2V4 and UR025.4, the IWBC and NBUC transports are at least 5 Sv larger than in ORAP5 and the FRMs (Fig. 3.8), and the former products then pro-

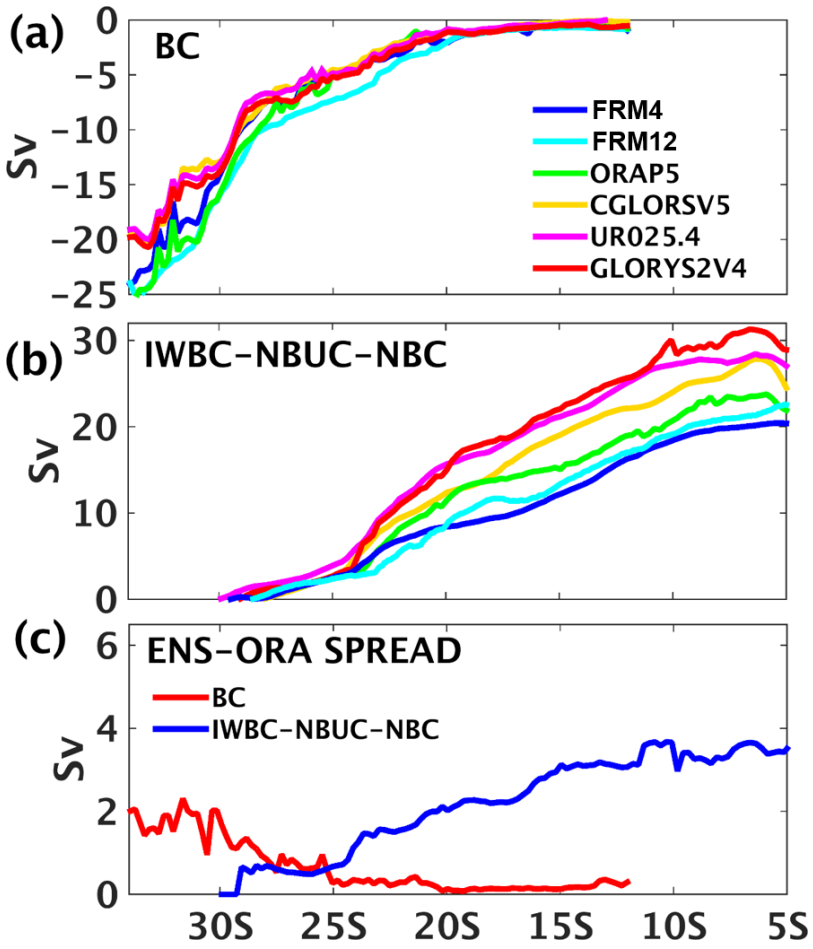

Figure 3.8: The transports (Sv) within 6° of the west coast for the (a) BC and (b) IWBC-NBUC-NBC system, following the isopycnal limits of the South Atlantic western boundary water masses as in *Mémery et al.* (2000) and *Donners et al.* (2005). The TW, SACW and AAIW limits are defined in $kg\ m^{-3}$ with $\sigma < 25.5$, $25.5 \leq \sigma < 27.1$, and $27.1 \leq \sigma < 27.3$, respectively. The ENS-ORA spread (Sv) of the western boundary current transports are displayed in (c).

duce a stronger NBC in the tropical South Atlantic, consistent with the observational estimates at 11°S (Fig. 2.7a). At each latitude the ORAs usually modify the upper western boundary circulation in the same direction, increasing (decreasing) the transports of the northward (southward) currents compared to the FRMs, which leads to higher MHTs across the entire basin. However, the western boundary transport magnitudes are not properly constrained in the ORAs, as reinforced by Fig. 3.8c, with the ENS-ORA spread increasing as current strengths increase. The IWBC-NBUC-NBC

spread particularly growths from ∼1 to 3.5 Sv towards the north which is comparable to the SAMOC spread seen in Fig. 3.1b. There is much better agreement for the BC near 35°S between the ORAs (ORAP5 excepted), with smaller spreads compared to the NBC.

In Fig. 3.9, the transports are schematically broken down into four boxes, the upper and lower western boundary region (within 6° of the coast), and the upper and lower ocean interior (z_{max} separates the upper and lower layers). Figure 3.9 summarises how the inter-product changes in the upper western boundary circulation correlate with the other three boxes (for the current systems involved see Fig. 1.5). In the tropical South Atlantic (Fig. 3.9a), the northward flows in the upper western boundary box in GLORYS2V4 and UR025.4 are ∼10 Sv and 8.5 Sv larger than in FRM4, respectively. These are mainly compensated by larger flows in the DWBC, by ∼9 Sv and 8 Sv in GLORYS2V4 and UR025.4, respectively, relative to FRM4. These large inter-product compensations confined to the western boundary extend to the subtropical region (Fig. 3.9b), where the ORAs with highest southward DWBC transports also show highest northward transports in the western boundary upper limb. Similarly, *Sitz et al.* (2015) found that the strengthening in the SAMOC upper limb with increasing model resolution is mainly compensated by strengthening of the poleward transport in the deeper layers, mostly in the western part of the basin. This large compensation between the upper and lower western boundary circulation is evident within all products in Fig. 3.9a, with the deep western boundary typically compensating for ∼70-75% of its upper limb transports, which was also noted in the observations of *Schott et al.* (2005) and *Hummels et al.* (2015) (Fig. 2.7).

In contrast to their western boundary circulations, the ORAs show very similar upper interior flows across the South Atlantic, consistently stronger than in the FRMs, regardless of direction (southward in Fig. 3.9a and northward in Fig. 3.9b). This consistency is retained even in the subtropical gyre (Fig. 3.9b), where the northward basin interior circulation can have larger magnitude than the upper western boundary

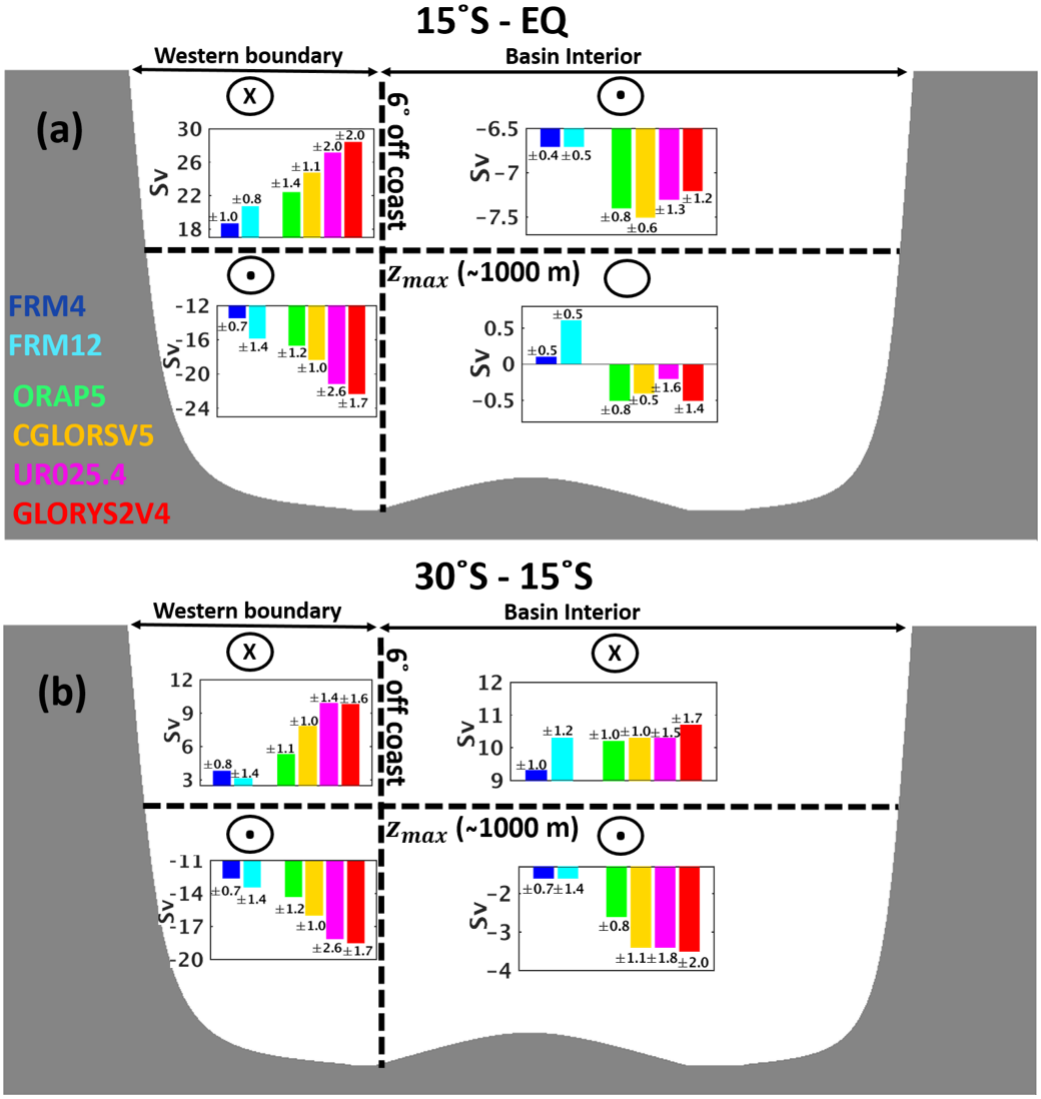

Figure 3.9: 4-box model of the averaged transports (1997-2010, in Sv) from (a) 15°S to the equator, and from (b) 30°S to 15°S. 6° off the coast is chosen to separate the western boundary from the basin interior. The depth of maximum SAMOC z_{max} for each product is used to separate the upper and deep circulations. The circles with x and dots represent flow going into and out of the page, respectively. The empty circle means that there is no agreement about the direction of the flow. $\pm$ corresponds to the interannual variability of each product. Note the different axes for each box.

currents to balance the DWBC. The deep interior box has negligible transports in the tropical South Atlantic, but significant southward transports further south, especially in the ORAs, suggesting that some portion of the NADW flows towards the interior of

the basin in the subtropical South Atlantic (*Garzoli et al.*, 2015).

3.5 Temporal variability

Figures 3.10a-f show that the interannual variability in p-OTTs is larger in the ORAs and in the high resolution FRM12 than in FRM4. The assimilation of observations in eddy-permitting models introduces variability that would otherwise only appear with higher resolution, as in FRM12. According to *Masina et al.* (2015), this higher variability in the ORAs is in better agreement with the EKE estimates from the Ocean Surface Current Analyses Real-time (OSCAR) than that of the FRMs. Although some of the ORAs have more transport variability than others throughout the basin, the western boundary variability remains a dominant feature, particularly northward of 25°S. In Fig. 3.10g, the interannual p-OTTs variances for each product are summed within 6° of the western boundary coast as a function of latitude and displayed as a percentage of the total MHT variance. It shows that the western boundary controls ∼70% of the interannual MHT variability in the tropical South Atlantic for almost all the products (UR025.4 excepted), but it is less dominant further south.

South of 25°S, the interannual variability of the transports is more spread, with contributions from the western boundary (near the Brazil-Malvinas confluence), and near the eastern boundary (due to the Agulhas leakage) with the largest values around 0.06 PWT per 0.25° in FRM12, UR025.4 and GLORYS2V4. The different levels of variability in the Agulhas leakage between FRM4 and ORAs may be attributed to the impacts of the SLA assimilation (*Backeberg et al.*, 2014). However, even between ORAs these Agulhas patterns differ, e.g. the weaker contributions in ORAP5 may be due to smoothing from the super-observation method applied to the altimeter data (*Mogensen et al.*, 2012), as also noted by *Masina et al.* (2015).

Figure 3.11a shows the monthly time series of both ψ_{max} and the maximum southward flow in the basin interior (as in Fig. 3.3g), as a spatial average from 15°S to the

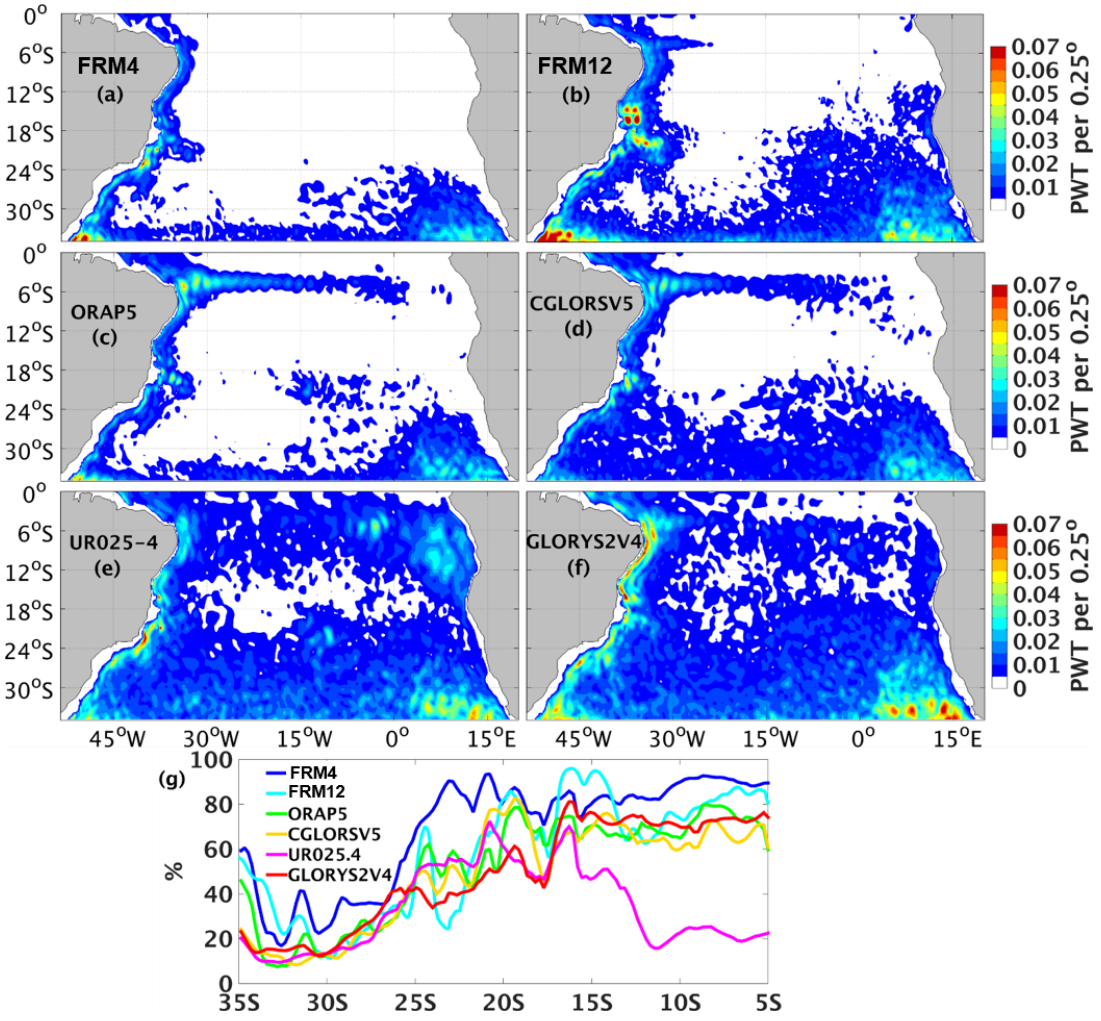

Figure 3.10: (a-f) Interannual p-OTT spread for the period 1997-2010. Units are in PWT per 0.25°. In (g) the interannual p-OTTs variances for each product are summed within 6° of the west coast across each latitude and displayed as a percentage of the total MHT variance.

equator. There appears to be greater consistency in the ORA southward transports in the second half of the time series, which is not seen in ψ_{max}. In Fig. 3.11b, the time series of the ENS-ORA spread for both components are also displayed. A running mean of 6 months was applied to smooth the ENS-ORA monthly variability. Even with large variations, particularly in the first years of the time series, the ENS-ORA spread for the upper southward flow is seen to reduce from ∼3 Sv to 1 Sv in the later years. This may be explained by the initiation of the Argo program and the increased number

of observations to constrain the southward interior flow in the ORAs. Although not shown, the ORA northward interior transports between 30°S and 15°S also look more consistent in the later years. However, the ENS-ORA spread in ψ_{max} remains nearly steady over this period, although the assimilation does increase the NBC transports in the ORAs relative to the FRMs (Fig. 2.7).

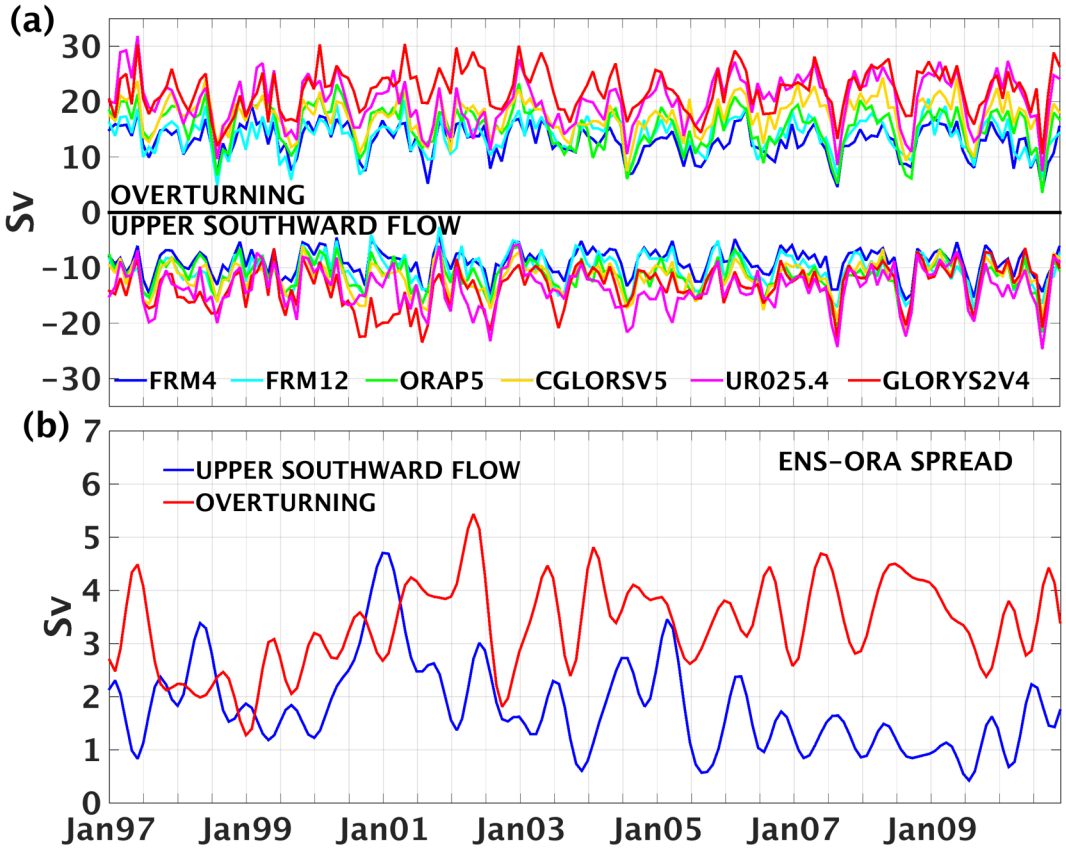

Figure 3.11: (a) Monthly time series of ψ_{max} (Sv) and the maximum upper southward flow (Sv) for each product calculated as an average from 15°S to the equator, and (b) their ENS-ORA spreads (Sv). A running mean of 6 months was applied to smooth the ENS-ORA spread time series. The upper southward flow is calculated using the same approach as in 3.3g.

3.6 Discussion and Conclusions

Some aspects of the circulation are well constrained by data assimilation (see also Chapter 2 for a more detailed ORA validation). The ORA circulation in the basin

interior is consistently modified across the basin relative to the FRMs (Fig. 3.3 and Fig. 3.9), with interior meridional transports converging as Argo data are introduced (Fig. 3.11). Zonally integrated temperature sections for the ORAs are also very similar to WOA13 (Fig. 3.4), whereas the FRMs have large anomalies. The relationship between the magnitudes of SAMOC and MHT in the ORAs is in good agreement with that inferred in observations (e.g. *Garzoli et al.*, 2013; *Majumder et al.*, 2016), and the SAMOC upper limb and MHT are also strongly correlated in time at most latitudes (Fig. 3.6).

Here, although the DA consistently changes the upper western boundary transports in the same direction (e.g. increasing the northward IWBC-NBUC-NBC and decreasing the southward BC), they do not consistently constrain the boundary current transport magnitudes. Large SAMOC and MHT discrepancies still remain between the ORAs. These discrepancies are mainly attributed to differences in the narrow South Atlantic western boundary currents found within a few degrees of the coast. For example, the NBC (15°S-equator) explains 85% of the inter-product differences in the total MHTs, with compensating variations in the return flow (DWBC) also close to the coast. Since the overturning stream function ψ_{max} is mainly associated with these boundary flows, it is not well constrained by the ORAs, particularly in the tropical South Atlantic.

Analysis of the heat transports also reveals that differences in transport rather than differences in temperature dominate the inter-product spread, even within the western boundary region. The temperature contribution to the inter-product spread in heat transport, $\overline{v}T$, is only $\sim$17% of the total spread, but its signature is evident right against the western boundary where temperature differences are required to geostrophically support the velocity differences between products. The local response to small density changes on the western boundary slope was also found to largely determine the meridional transport variability in ocean models in the North Atlantic, as noted by *Bingham and Hughes* (2009), emphasising the large sensitivity of the currents with respect to local density gradients against the boundary.

It is noteworthy that the lateral boundary conditions in the ORAs and FRMs vary between free-slip (α=0) and partial-slip (α=0.5). However, there is no clear correspondence between the choice of lateral boundary conditions and the strength of the western boundary transports, with free-slip products (e.g. UR025.4) having similar transports to partial-slip products (e.g. GLORYS2V4).

Two possible reasons for the ORA differences in the western boundary currents are: (i) the lack of near boundary observations, and/or (ii) the differences in DA error covariances when assimilating interior basin measurements lying near to the western boundary. Observation system simulation experiments (OSSEs) with AMOC trans-basin arrays have shown that the meridional flow strength can be sensitive to the number of hydrographic profiles near the boundaries in both North (e.g. *Hirschi et al.*, 2003; *Baehr et al.*, 2004) and South Atlantic (e.g. *Perez et al.*, 2011). The combined assimilation of open ocean hydrographic observations and the continuous RAPID array western boundary measurements have also been shown to locally improve the AMOC strength at 26.5°N (*Stepanov et al.*, 2012). This emphasises the role that more systematic observations located at the eastern and western boundaries at several latitudes may play in monitoring the AMOC (*Marotzke et al.*, 1999). In the future, the SAMOC observing system (*Ansorge et al.*, 2014; *Hummels et al.*, 2015), which will provide time series of NBC measurements at the western boundary at 11°S, could be assimilated into the ORAs to constrain the regions of largest spread in the tropical South Atlantic.

Differences in data assimilation methods near the boundaries may also be influencing the overturning in the different ORAs. For example, *Balmaseda et al.* (2013a) noted that the AMOC at 26°N in the ECMWF reanalyses is very sensitive to the treatment of observations and the parametrization of their errors near to the boundaries, although similar changes are not documented for other ORAs. *Stepanov et al.* (2012) also showed that the assimilation impacts of the RAPID western boundary measurements on the AMOC can vary according to the prescribed horizontal scales of the DA error covariances, e.g. with boundary-focused covariances producing larger positive

impacts on the AMOC than isotropic covariances. In order to better understand the large SAMOC sensitivity found between the ORAs, future work in Section 6.4 explores the response of the western boundary and SAMOC transports to changes in the ORA configurations, such as sensitivity experiments to the assimilated datasets and to the DA schemes near the western boundary.

CHAPTER 4

DECOUPLED FRESHWATER TRANSPORT AND MERIDIONAL OVERTURNING IN THE SOUTH ATLANTIC

4.1 Introduction

The freshwater transport by the AMOC itself (F_{ov}) has been proposed as an indicator of the AMOC bi-stability, a situation where the AMOC could switch between ″on″ and ″off″ states (a collapsed or weak AMOC). Based on results from simple box models (*Stommel*, 1961; *Rahmstorf*, 1996; *De Vries and Weber*, 2005, a bi-stable AMOC is suggested to occur when the overturning circulation exports freshwater from the Atlantic ($F_{ov} < 0$), with F_{ov} typically being measured at the southern boundary at 34°S. In this scenario, *assuming other feedbacks are negligible*, a weakening of the AMOC is followed by a weakening of F_{ov} and freshening of the whole basin, which in turn further reduces the model AMOC creating a positive feedback loop (*Drijfhout et al.*, 2011; *Hawkins et al.*, 2011).

However, F_{ov} at 34°S may be a poor indicator of the true freshwater feedbacks during a changing AMOC, because the South Atlantic subtropical gyre can adjust in conjunction with the AMOC, as noted by *Sijp* (2012). Furthermore, F_{ov} has also been shown to be sensitive to biases in coupled climate models, with suggested implications

that many models may be artificially stable (*Yin and Stouffer*, 2007; *Jackson*, 2013; *Liu et al.*, 2017; *Mecking et al.*, 2017). In particular, F_{ov} in the southern Atlantic can easily change sign when salinity bias corrections are accounted for, as seen for many CMIP5 models (*Mecking et al.*, 2017).

It is in this context that ORAs can be useful tools to investigate the freshwater transport throughout the Atlantic, since they employ DA methods to constrain models to a diverse network of available ocean observations, giving a consistent estimate of the historical ocean state (e.g. *Masina et al.*, 2015; *Palmer et al.*, 2015). The complete, time-evolving ORA descriptions of the ocean circulation are already used for initialising climate model transports, aiming to improve decadal predictions of the AMOC (*Pohlmann et al.*, 2009; *Bellucci et al.*, 2013). Comparisons between ORAs and historical model runs without data assimilation, i.e. FRMs, also give valuable insights into how ocean transports, which are not directly observed, are affected by DA (e.g. *Karspeck et al.*, 2015).

In order to elucidate feedbacks between salinity and the strength of the AMOC, here we use two FRMs and four ORAs to investigate the role of salinity in modulating both overturning and gyre freshwater transports across the Atlantic. We also draw some useful comparisons between the meridional freshwater transports and the meridional heat transports. This chapter begins with a brief overview of the mathematical framework in Section 4.2. The components of the transports are investigated in Section 4.3, followed by an analysis of the salinity distribution and its impact on the freshwater overturning (Section 4.4) and gyre (Section 4.5) components. Discussion and conclusions are presented in Section 4.6.

4.2 Mathematical Framework

In order to calculate transports across each latitudinal section, following a number of earlier studies, notably *Bryden and Imawaki* (2001), the mean baroclinic freshwater and

heat transports are decomposed into a mean vertical (overturning) and mean horizontal (gyre) component:

$$F_{mean} = F_{ov} + F_{gyre} = -\frac{1}{\hat{S}} \int_{-H}^{0} v^* \langle S \rangle \, dz - \frac{1}{\hat{S}} \int_{W}^{E} \int_{-H}^{0} v'' S'' dz dx \tag{4.1}$$

$$Q_{mean} = Q_{ov} + Q_{gyre} = \rho C_p \int_{-H}^{0} v^* \langle T \rangle \, dz + \rho C_p \int_{W}^{E} \int_{-H}^{0} v'' T'' dz dx \tag{4.2}$$

where H is the ocean depth, W and E correspond to the western and eastern boundaries, $\langle \cdot \rangle$ represents the zonal mean, the double prime $''$ denotes deviations from zonal averages, $\hat{S}$ is the section averaged salinity, and v^* corresponds to deviations of the zonal mean meridional velocity from its section averaged values. In Eq. 4.2, ρ is the seawater density and C_p is the specific heat capacity of seawater. Positive (negative) F_{mean} and Q_{mean} are northward (southward).

4.3 Transport components

In Figs. 4.1a-c, the 1997-2010 F_{mean} transports are shown with F_{ov} and F_{gyre} components. The gyre component of these transports is anti-symmetric with similar magnitudes but opposite sign around ∼5°N, and we will return to this component later. Unlike F_{gyre}, F_{ov} magnitudes are quite different in each hemisphere. Throughout the South Atlantic, F_{ov} is consistently small, although not consistently negative, ranging from -0.07 to 0.1 Sv, and therefore F_{mean} is determined by F_{gyre}. All the products show a slightly negative F_{ov} at 34°S, supported by observations (*Garzoli et al.*, 2013), which has been suggested to indicate a bi-stable AMOC as discussed in Section 5.1. In contrast, the North Atlantic has a large negative F_{ov} peak reaching -0.6 Sv in the ORAs, also consistent with the observations (*McDonagh et al.*, 2010; *McDonagh et al.*, 2015). As a result, F_{mean} is negative through the North Atlantic at least down to 20°N,

due to the dominance of F_{ov} over F_{gyre} in the subtropics. The North Atlantic negative F_{ov} peak in the FRMs is only about -0.3 Sv, consistent with the fresh FRM bias which will be discussed later.

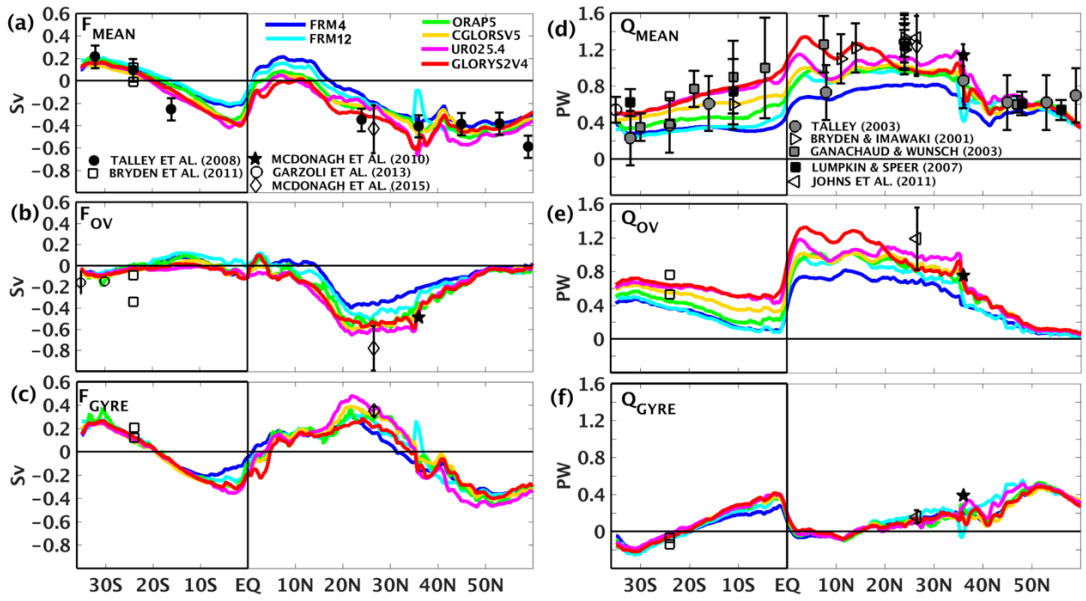

Figure 4.1: The mean (a) freshwater (Sv) and (d) heat transports (PW) across the Atlantic from 1997 to 2010, with their (b, e) overturning and (c, f) gyre components, respectively. Observational transport estimates at various sections are also included for comparison, using calculations based on Eq. 4.1 and Eq. 4.2.

Figure 4.1b also clearly shows consistency between the ORAs in reproducing F_{ov} in both hemispheres, despite AMOC differences of up to ~8 Sv throughout the basin (Fig. 3.1). This is perhaps surprising as the spread of the overturning heat component Q_{ov} (Fig. 4.1e) is clearly sensitive to the AMOC differences (Fig. 3.5), determining the spread in the mean heat component Q_{mean} (Fig. 4.1d). The gyre heat transports Q_{gyre} (Fig. 4.1f) are much smaller in both basins, and agree with each other and with the observations, supporting the consistent interior circulation shown by the model products in Fig. 3.3 and Fig. 3.9.

4.4 F_{ov} and vertical salinity structure

The AMOC stream function shown in Fig. 4.2a transports freshwater northwards or southwards depending upon the salinity difference between its northward moving upper branch and its southward moving lower branch (NADW). Figure 4.2b shows the zonal and depth averaged salinity difference between the upper and lower waters, ΔS, as a function of latitude for the FRMs, ORAs and EN4.2.1. Note that a positive ΔS (i.e. upper branch saltier than the lower branch) corresponds to a northward salt transport and a southward freshwater transport (and vice-versa). The solid lines correspond to the case where the boundary between upper and lower waters is set at 1200 m, ΔS_{1200m}, approximately separating the upper and lower AMOC branches (i.e. the depth of the maximum AMOC stream function; Fig. 4.2a). Dashed lines have a dividing boundary at only 300 m, ΔS_{300m}, chosen to match the shallow salinity stratification in the South Atlantic. For the AMOC depth, ΔS_{1200m} is $\sim$0.8 psu in the North Atlantic, but this falls to $\sim$0 psu in the South Atlantic. Therefore because the upper and lower branches of the AMOC have similar salinity in the South Atlantic, the AMOC has very little freshwater transports in this basin (Fig. 4.1b), even though the AMOC itself is strong (Fig. 4.2a) and varies greatly between the different products (Fig. 3.1). This decoupling between the AMOC and F_{ov} in the South Atlantic, due to a small ΔS_{1200m}, contrasts with the large North Atlantic ΔS_{1200m} and substantial F_{ov} between 20°N and 40°N.

Figure 4.2c shows the equivalent temperature differences, with ΔT_{1200m} steady at $\sim$6°C in the South Atlantic, allowing the AMOC to still play a leading role in heat transport throughout this basin (Fig. 4.1e). Furthermore, the wind driven Subtropical Cells (STCs; *Zhang et al.*, 2003), which counteract (enhance) the AMOC south (north) of the equator in Fig. 4.2a, produce a sharp cross-equatorial Q_{ov} increase, but have little effect on F_{ov} (Fig. 4.1b). Following the same approach as in Fig. 4.2, the ΔS_{150m} between the upper (0-150 m) and lower (150-300 m) STC branches is less than $\sim$0.1 psu (Fig. 4.3a), which acts to neutralise the STC circulation impact on F_{ov}. Unlike ΔS_{150m},

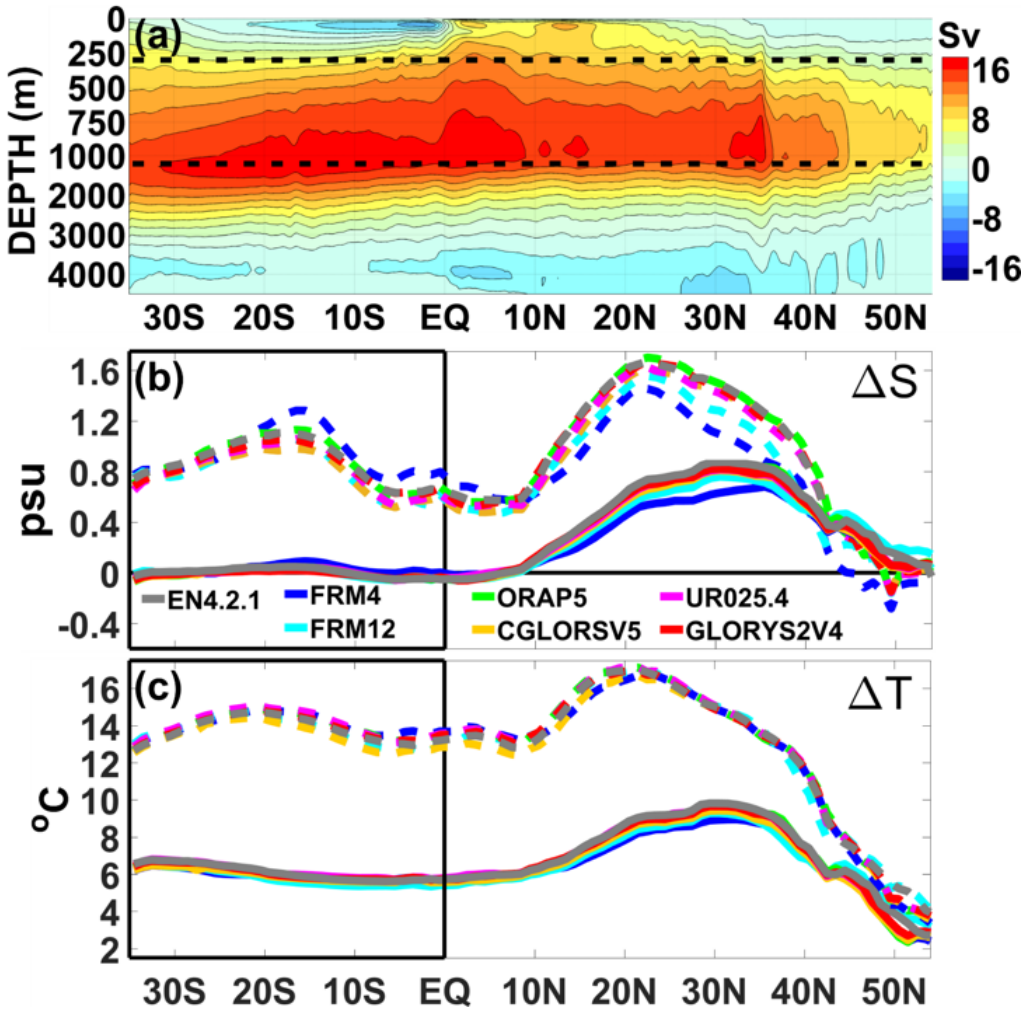

Figure 4.2: (a) The 1997-2010 AMOC stream function (Sv) computed as the mean of all the model products. In (b) and (c) the 1997-2010 zonally averaged ΔS (psu) and ΔT (°C) are divided at 300 m (dashed lines) and 1200 m (solid lines), respectively, to separate the upper and lower branches. The horizontal black dashed lines in (a) correspond to depths of 300 m and 1200 m shown in (b, c). Note the stretched vertical axis in (a) between 0-1000 m, compared to 1000-5000 m.

the ΔT_{150m} is ~8.2°C and ~8.8°C in the south and north STC cells, respectively (Fig. 4.3b), allowing these shallow circulations to contribute significantly to Q_{ov} near the equator. Note that all products show a north STC cell ~0.6°C warmer than the south cell, consistent with the strongest Q_{ov} north of the equator.

In order to understand the vertical salinity differences between the northern and southern basins, Fig. 4.4a shows the zonally averaged salinity from EN4.2.1 with su-

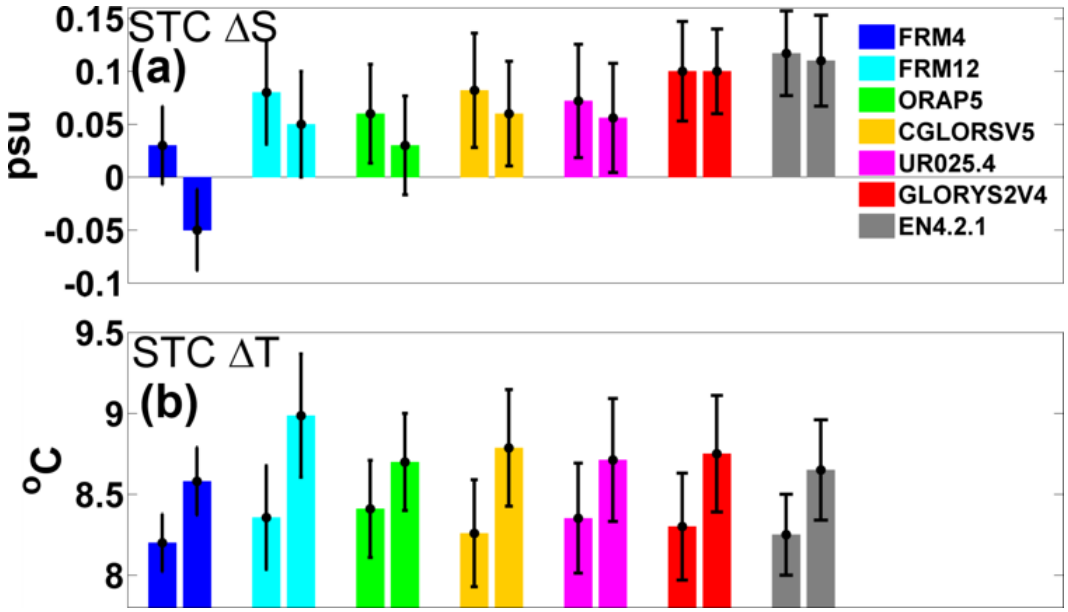

Figure 4.3: The (a) ΔS (psu) and (b) ΔT (°C) of the STCs adopting the depth of 150 m to separate their upper (0-150 m) and lower (150-300 m) branches. The south STC cell from 5°S to the equator is represented by the left bar of each product, whereas the north STC cell from 5°N to the equator corresponds to the right bars. The black bars represent the annual standard deviation of the south and north STC cells.

perimposed AMOC stream function contours from Fig. 4.2a. The upper ocean salinity maximum in the South Atlantic Subtropical Gyre (SASG) is weaker and decreases rapidly with depth compared to the North Atlantic Subtropical Gyre (NASG), supporting Fig. 4.2b. This is partly due to the very fresh AAIW formed at ∼50°S, which subducts under the SASG truncating the salinity core to much shallower depths. This intermediate layer is even fresher than the NADW, so that the top 1200 m layer has almost the same salinity as the NADW below (Fig. 4.4b), giving negligible ΔS_{1200m} up to ∼10°N where the AAIW is curtailed. The surface salty core also weakens at the latitude of the mean ITCZ (∼5°N), producing a sub-surface salinity maximum before it freshens again down to 300 m. This low-high-low salinity structure in the top 300 m near the equator is consistent with the very small ΔS_{150m} across the STCs (Fig. 4.3a).

ΔS_{1200m} increases in the North Atlantic as the AAIW is replaced by the very salty Mediterranean Water (MW). The MW helps to deepen and intensify the NASG upper

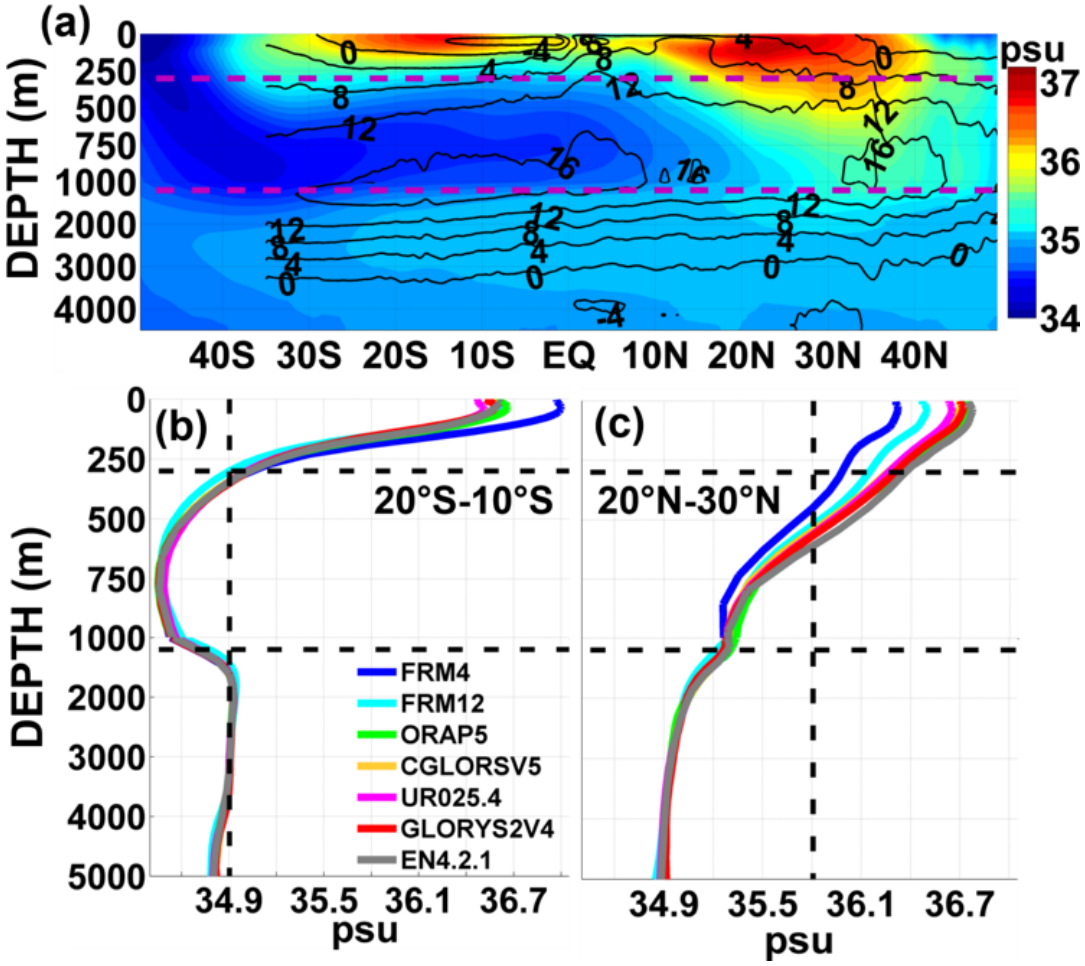

Figure 4.4: (a) The 1997-2010 zonally averaged salinity (psu) from EN4.2.1 in the Atlantic, superimposed with AMOC stream function (Sv) contours from Fig. 4.2. The salinity profiles (psu) from (b) 20°S to 10°S and (c) 20°N to 30°N, are also shown for all products. The vertical black dashed lines in (b, c) correspond to the 0-1200 m mean salinity from EN4.2.1. The depths of 300 m and 1200 m are represented by the horizontal purple and black dashed lines in (a) and (b, c), respectively. Note the stretched vertical axis.

layer salinity core (*Blanke et al.*, 2006; *Jia et al.*, 2007), giving high salinity down to considerable depth in the profiles of Fig. 4.4c. The deep NASG salinity core leads to a strong contrast between the upper and lower layer salinities (i.e. larger ΔS_{1200m}), which then allows the AMOC to produce a strong freshwater transport in the subtropical North Atlantic. The F_{ov} strength, and hence the coupling between the AMOC and the freshwater budget, is controlled by ΔS_{1200m}. This explains key results related to

AMOC bi-stability arguments, for example how correcting the model salinity biases significantly change the correlations between the AMOC strength and F_{ov} through the basin (*Mecking et al.*, 2017).

All the reanalyses show very good agreement with EN4.2.1 salinities in both South and North Atlantic (Fig. 4.2b and Fig. 4.4b-c), due to the assimilation of salinity profiles and the additional SSS relaxation towards climatology in ORAP5 and CGLORSV5. The realistic zonal-depth mean salinities seen in the ORAs in both hemispheres also lead to their consistent F_{ov} (Fig. 4.1b). The ORAs have larger ΔS_{1200m} in the North Atlantic, in better agreement with EN4.2.1 than the FRMs, leading to a larger negative F_{ov} peak there, which is closer to hydrographic inverse estimates (Fig. 4.1b). The FRM upper layers (0-1200 m), even with SSS restoring, are fresher than EN4.2.1 in the NASG. This is a common model deficiency possibly due to excessive MW mixing with surrounding water masses (*Jia*, 2000; *Jia et al.*, 2007; *Legg et al.*, 2009), which DA helps to mitigate in the ORAs (Fig. 4.4c). This upper fresh bias reduces the FRM vertical salinity contrasts in the subtropical North Atlantic, giving their smaller negative F_{ov} peak. In the SASG (Fig. 4.4b) the FRM biases are mostly confined to the top 250 m, and therefore project less onto the AMOC upper branch, supporting the better F_{ov} agreement between all model products in the South Atlantic.

4.5 F_{gyre} and horizontal salinity gradients

We have seen how the shallower (deeper) salinity core of the South (North) Atlantic in Fig. 4.4 influences the F_{ov} strength. We now evaluate the salinity and temperature deviations from zonal averages, S'' in Eq. 4.1 and T'' in Eq. 4.2, for particular depth ranges upon which the gyre circulation acts. Figure 4.5 shows that ORA S'' and T'' are much stronger in the upper 0-300 m relative to the 300-1200 m depth range in both hemispheres, but especially in the South Atlantic. In contrast, the ORA gyre circulations displayed in Fig. 4.6 clearly extend deeper, with the 300-1200 m depth

range having similar or even larger gyre circulation strengths in areas such as the Gulf Stream and the North Atlantic subpolar region.

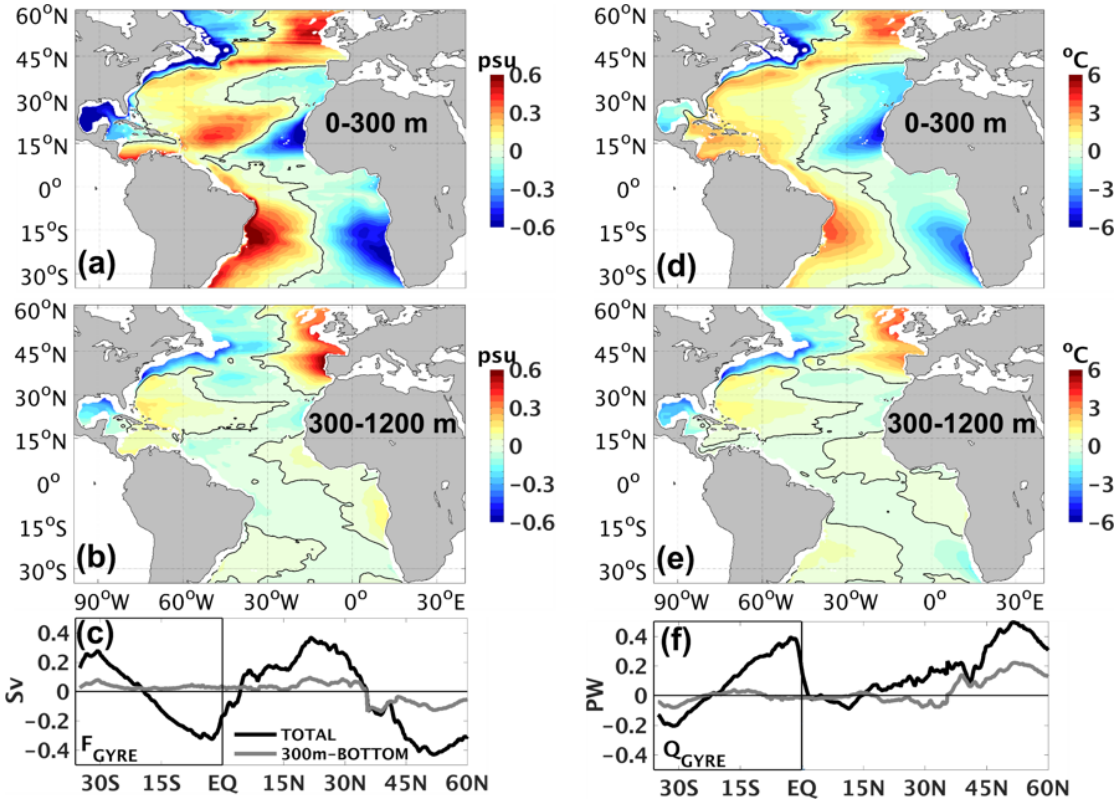

Figure 4.5: The ORA depth averaged S'' (a, b) and T'' (d, e) for 0-300 m and 300-1200 m, respectively. The black solid contour corresponds to 0 psu or 0°C. The ORA meridional gyre freshwater (Sv) and heat (PW) transports are displayed in (c) and (f), respectively, for the total depth (black) and 300 m-bottom (grey).

Although the gyre circulations are deeper, only the S'' and T'' in the top 300 m make a significant contribution to the gyre freshwater and heat transports south of 30°N (Fig. 4.5c, f), as the zonal salinity and temperature contrasts below 300 m are much smaller (Fig. 4.5b, e). North of ~30°N there are still relatively large zonal deviations in the 300-1200 m depth range due to contrasts caused by the Gulf Stream and, on the eastern side, by the injection of the MW outflow at mid-depths. This leads to more significant S'' and T'' contributions to the gyre transports below 300 m. Although not shown, very similar patterns can also be found in the FRMs.

The gyres in Fig. 4.5c lead to freshwater convergence at ~20°S and ~35°N, acting

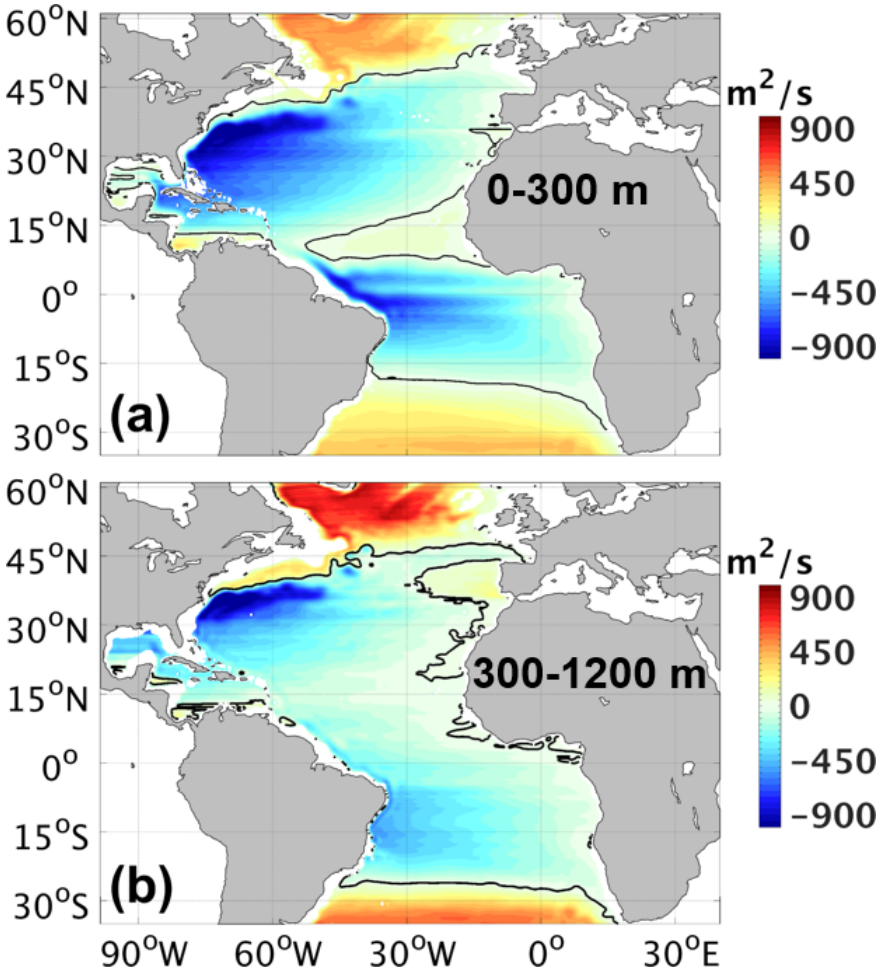

Figure 4.6: The ORA gyre stream function ($m^2\ s^{-1}$) for (a) 0-300 m and (b) 300-1200 m. The black solid contour represents 0 $m^2\ s^{-1}$.

to balance the positive evaporation minus precipitation (E-P) at these latitudes. The shallowness of the main F_{gyre} transports in most of the basin is required to compensate for this surface forcing (Fig. 4.7) which maintains the strong near surface salinity gradients in Fig. 4.4a. This is also consistent with the fact that F_{gyre} transports in the North Atlantic look quite similar in magnitude to those in the south, with an anti-symmetric pattern around the mean ITCZ location at ~5°N.

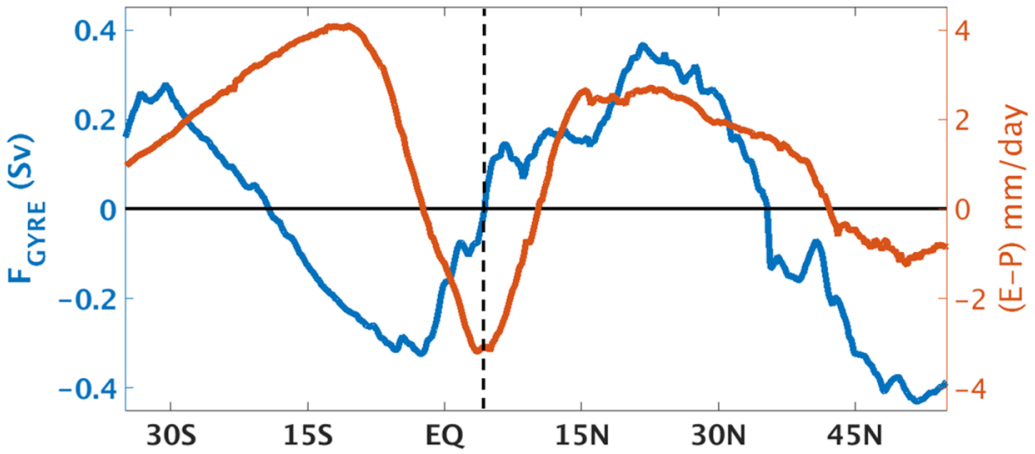

Figure 4.7: The ORA gyre freshwater transports (Sv) in blue plotted against the ORA E-P ($mm\ day^{-1}$) in orange for the period 1997-2010. The black dashed line represents the latitude where the freshwater gyre transport equals zero just north of the equator, matching the ITCZ negative E-P peak.

4.6 Discussion and Conclusions

The ocean transport components, particularly of freshwater, in both South and North Atlantic are investigated in two NEMO FRMs and four ORAs over 1997-2010. We show that variations in the strength of the freshwater overturning transport F_{ov} through the basin are largely explained by variations of the vertical salinity contrast ΔS_{1200m}, based on the separation between the upper and lower AMOC branches at ∼1200 m. South of ∼10°N, the very fresh AAIW limits the evaporation-driven high salinity layer to shallower depths. The average salinity through the top 1200 m is then almost the same as the salinity below 1200 m consisting mostly of NADW. As a consequence of this small ΔS_{1200m}, seen in the FRMs, ORAs and observations, the AMOC, despite transporting a substantial amount of heat at these latitudes, has only very small freshwater transports. Even the shallow wind-driven STCs, which contribute to the cross-equatorial heat transports, do not add significant freshwater transport to F_{ov} due to the small ΔS between the upper (0-150 m) and lower (150-300 m) STC branches near the equator. North of ∼10°N F_{ov} rapidly increases as the AAIW layer disappears allowing the development of a substantial vertical salinity contrast between the AMOC

branches, especially in the ORAs, and driving large southward freshwater transports in the NASG.

Since a realistic ΔS_{1200m} effectively shuts off, or greatly weakens, first order feedbacks between the AMOC changes and F_{ov} throughout the South Atlantic, the use of F_{ov} at 34°S (e.g. *Rahmstorf*, 1996) as an indicator of the AMOC bi-stability must be questioned. This feedback relies on F_{ov} changing with the AMOC strength and acting as the main feedback on the North Atlantic freshwater budget. Our results emphasise that F_{ov} at 34°S is not strongly coupled to the AMOC, nor is it likely to be a significant term in the freshwater budget, at least when compared to northern latitudes where F_{ov} is nearly an order of magnitude larger. Therefore, our findings suggest that the second feedback mechanism from box-models in Fig. 1.7 does not exist.

After correcting the salinity biases in the CMIP5 models, *Mecking et al.* (2017) found large changes in the correlation patterns between the basin-scale F_{ov} and the AMOC strength computed at 26.5°N. Correlations based on the modelled salinity fields, which were significantly positive south of ∼10°N, become very small after model salinities are corrected (e.g. essentially zero at 34°S). This also shows that with a realistic vertical salinity structure the wide range of AMOC strengths in CMIP5 models have basically no impact on the South Atlantic F_{ov}. This is consistent with our results: although the FRMs and ORAs show large AMOC discrepancies (e.g. up to ∼8 Sv; Fig. 3.1), they all give a consistently small F_{ov} throughout the South Atlantic. They all have a weak negative F_{ov} at 34°S, also seen in the bias corrected CMIP5 models, but significantly for the bi-stability argument, F_{ov} also varies in sign through the South Atlantic (Fig. 4.1b). As shown by our investigation, the decoupling between the AMOC and F_{ov} exists at all latitudes south of ∼10°N due to the negligible ΔS_{1200m}, ensuring the very small F_{ov} throughout the South Atlantic.

The Atlantic vertical salinity distributions, including the water mass formation regions, are unrealistic in many climate models due to poor freshwater flux fields from the atmosphere component. For example, in the majority of the CMIP5 models a fresh

surface bias in the AAIW formation region leads to a fresh, less dense and shallower AAIW layer throughout the South Atlantic (*Yin and Stouffer*, 2007; *Sallée et al.*, 2013; *Zhu et al.*, 2018). This fresh upper layer bias leads to a negative ΔS_{1200m}, explaining the spurious South Atlantic correlations between F_{ov} and AMOC strength in the uncorrected CMIP5 models (*Mecking et al.*, 2017). However, there is no reason why these correlated biases between different CMIP5 models would be relevant to stabilizing or destabilizing feedbacks on the AMOC when ΔS_{1200m} is $\sim$0 psu as in the real system, because there would be no direct mechanism by which an AMOC change could influence the AAIW water formation region and hence move ΔS_{1200m} away from $\sim$0 psu.

We also show that the freshwater gyre transport F_{gyre} mostly determines the South Atlantic total transport F_{mean}. At 34°S, F_{gyre} is consistently larger than F_{ov}, so that the total transport is actually northward and compensates for the net evaporation in the subtropical South Atlantic. These F_{gyre} transports exhibit a marked anti-symmetric pattern around the mean ITCZ location at $\sim$5°N, redistributing freshwater within a 0-300 m upper ocean layer in the subtropics of both hemispheres. In a freshwater hosing experiment with an eddy-permitting coupled model, *Mecking et al.* (2016) showed that the dominant response of F_{gyre} at $\sim$34°S is over twice as large as the changes in F_{ov}, despite the total AMOC collapsed. Changes in E-P induced by an AMOC collapse, such as an ITCZ shift, also support the large F_{gyre} changes found by *Mecking et al.* (2016) in the South Atlantic. Our analysis, combined with previous literature, suggests that feedbacks associated with F_{gyre} will likely dominate those associated with F_{ov} throughout the South Atlantic, and thus would be more relevant in any AMOC bi-stability scenario.

Yin and Stouffer (2007) and *Mecking et al.* (2016) instead suggest that a better bi-stability indicator might be to measure F_{ov} across the NASG where the salinity bias corrected CMIP5 models show the largest correlations between F_{ov} and AMOC strength (*Mecking et al.*, 2017). Our results identify the substantial ΔS_{1200m} in the

NASG, particularly in the ORAs, where DA helps to reduce salinity biases, e.g. possibly arising due to the excessive mixing of Mediterranean waters in the FRMs. However, applying the same reasoning as for F_{ov} at 34°S, one would conclude that all models are therefore unstable as they systematically simulate a large negative F_{ov} in the NASG (see Fig. 4.1b and *Mecking et al.*, 2017). As this does not appear to be the case, it is evident that other feedbacks, oceanic as well as atmospheric, would likely play a significant role in the instance of an AMOC weakening.

CHAPTER 5

SALT-ADVECTION FEEDBACK MECHANISMS WITHIN CMIP5 MODELS

5.1 Introduction

The salt-advection feedback and AMOC bi-stability in climate models are typically addressed by applying instantaneous freshwater perturbations (i.e. freshwater hosing) to the North Atlantic (e.g. *Huisman et al.*, 2010; *Jackson*, 2013; *Mecking et al.*, 2016). During and after the hosing is applied, the AMOC behavior is evaluated considering its relationship with F_{ov}, which has been shown to vary depending on the model complexity and intensity of the hosing. Some freshwater hosing experiments in coarse ocean-only and intermediate-complexity coupled models show that models with negative southern F_{ov} sustain a collapsed AMOC for longer times, and have a slower recovery than models with positive southern F_{ov} (e.g. *Rahmstorf et al.*, 2005). However, similar experiments in more complex climate models, including eddy-permitting ocean components, reveal a more diverse AMOC behavior, ranging from no evidence of an AMOC shutdown (e.g. *Stouffer et al.*, 2006) to a situation where a collapsed AMOC was maintained for 450 years (e.g. *Mecking et al.*, 2016).

In addition to the uncertainties of the AMOC bi-stability in complex coupled mod-

els, the strong response to large freshwater perturbations in hosing experiments also drives strong non-linearities in the evolution of the coupled system, making it difficult to separate the individual contributions of velocity and salinity perturbations. Assessing how the meridional velocity and salinity contribute to F_{ov} variability is of fundamental importance since the salt-advection feedback assumes that variability in F_{ov} is determined by the variability of AMOC rather than salinity throughout the basin, i.e. $dF_{ov} = \overline{\Delta S} \cdot d\psi$ (*Rahmstorf*, 1996).

Instead of running freshwater hosing experiments, here we take a different approach to study the salt-advection feedback. The internal variability of 10 centennial-scale CMIP5 simulations, with both positive and negative F_{ov} at 34°S, are used to investigate whether salt-advection feedback mechanisms in Fig. 1.7 can be detected on a range of timescales. Specifically, we seek for evidences in the variability of these models to clarify the following points: is the southern F_{ov} variability dominated by changes in the local circulation or salinities? What is the influence of the southern F_{ov} and F_{gyre} in contributing to freshwater content (FWC) changes throughout the basin? How far north is the southern F_{ov} correlated to the AMOC transports?

In order to answer the questions above, the chapter is organised as follows. The CMIP5 models and their main configurations are presented in Section 5.2. Section 5.3 provides the mathematical framework used for the investigation of the salt-advection feedback mechanisms in Fig. 1.7. To set the stage, Section 5.4 evaluates the mean state of the selected CMIP5 models, particularly focusing on the sensitivity of their mean F_{ov} to the vertical salinity distributions. Section 5.5 evaluates the F_{ov} time components, by calculating the contributions of meridional velocity and salinity variations to F_{ov} anomalies on a range of timescales and across different latitudes. Freshwater budgets are calculated in Section 5.6 to identify the main drivers of FWC changes throughout the Atlantic from interannual to multidecadal timescales. Section 5.7 investigates how far north the southern F_{ov} and the AMOC transports are correlated on different timescales. Finally, Section 5.8 ends the chapter with discussions and conclusions.

5.2 CMIP5 models

To examine whether salt-advection feedback mechanisms are detected in climate models, we have selected 10 CMIP5 pre-industrial control simulations conducted by different institutions and with distinct ocean and atmospheric models (see Tab. 5.1). In these simulations, the greenhouse gas emissions, volcanic and anthropogenic aerosols, as well as radiative forcing are held constant at pre-industrial levels, therefore removing from our analyses any influence of external climate forcing variations. The length of these pre-industrial runs varies according to each model in Tab. 5.1, ranging from 300 years in IPSL-MR to 1000 years in IPSL-LR. More details on the CMIP5 experiment design can be found in *Taylor et al.* (2012).

The 10 selected CMIP5 models are separated into two groups of 5 models, based on the sign of their mean F_{ov} at 34°S (hereafter F_{ov}^{34S}). The model choices were strategically made to be representative of different F_{ov}^{34S} values, including extreme cases of negative and positive F_{ov}^{34S}, which range from -0.17 Sv to 0.7 Sv. In Tab. 5.1, the ocean models employed are NEMO (*Madec*, 2008), the Parallel Ocean Program version 2 (POP2.0; *Smith*, 2010), the Modular Ocean Model version 4 (MOM4; *Griffies*, 2009) and the Generalized Ocean Layered Dynamics (GOLD; *Adcroft and Hallberg*, 2006). Similarly, the atmospheric models used are the fifth-generation of the ECMWF Hamburg atmospheric model (ECHAM5; *Roeckner*, 2003), the Community Atmosphere Model version 4 (CAM4; *Neale*, 2003), the atmospheric model of the Laboratoire de Météorologie Dynamique (LMDz; *Remaud et al.*, 2018) and the Atmospheric Model Version 2 (AM2; *Lin*, 2004). Some CMIP5 simulations, such as BCC-CSM1 and CSIRO-MK3, use atmospheric models from their own institutions, respectively, the BCC-AGCM2.1 (*Xin et al.*, 2013) and Mk3-AGCM2 (*Gordon et al.*, 2010). The average horizontal resolutions of the ocean and atmospheric components are also given by Tab. 5.1. All the ocean models employ z-level vertical coordinates, except for GFDL-ESM2G which has isopycnal coordinates but its data are stored on z-levels in

Table 5.1: List of selected CMIP5 products with the institution that conducted the simulations, the length of each simulation, the models and their horizontal resolutions, the F_{ov} at 34°S and its annual variability. The stars before the product names indicate models for which freshwater surface fluxes are available on their ocean grids in the CMIP5 database. CMIP5 models above and below the thick solid line have negative and positive F_{ov}^{34S}, respectively.

Products	**Institution**	**Years**	**Ocean model**	**Ocean resolution**	**Atm model**	**Atm resolution**	F_{ov} **34°S (mSv)**	**References**
*CMCC-CM	CMCC	330	NEMO	2.0° x 1.9°	ECHAM5	0.8° x 0.8°	-107 ± 37	*Scoccimarro et al.* (2011)
*CMCC-CMS	CMCC	500	NEMO	2.0° x 1.9°	ECHAM5	3.7° x 3.7°	-165 ± 40	*Scoccimarro et al.* (2011)
FIO-ESM	FIO	800	POP2.0	2.0° x 2.0°	CAM4	2.8° x 2.8°	-101 ± 27	*Qiao et al.* (2013)
*IPSL-LR	IPSL	1000	NEMO	2.0° x 1.9°	LMDz	1.9° x 3.7°	-56 ± 31	*Dufresne et al.* (2013)
*IPSL-MR	IPSL	300	NEMO	1.6° x 1.4°	LMDz	1.3° x 2.5°	-15 ± 23	*Dufresne et al.* (2013)
BCC-CSM1	BCC	400	MOM4	1.0° x 1.0°	BCC-AGCM2.1	2.8° x 2.8°	145 ± 30	*Xin et al.* (2013)
BNU-ESM	BNU	559	MOM4	1.0° x 1.0°	CAM4	2.8° x 2.8°	702 ± 72	*Ji et al.* (2014)
CCSM4	NCAR	500	POP2.0	1.1° x 0.6°	CAM4	1.2° x 1.0°	145 ± 13	*Danabasoglu et al.* (2012)
*CSIRO-Mk3	CSIRO-QCCE	500	MOM4	1.0° x 1.9°	Mk3-AGCM	1.9° x 1.9°	274 ± 48	*Gordon et al.* (2010)
*GFDL-ESM2G	NOAA GFDL	500	GOLD	0.5° x 1.0°	AM2	2.0° x 2.0°	220 ± 29	*Dunne et al.* (2012)

the CMIP5 database.

With respect to different CMIP5 simulations belonging to the same institution in Tab. 5.1, they basically differ because of the horizontal resolution employed. For example, CMCC-CM has a much higher atmospheric resolution of 0.8° when compared to 3.7° from CMCC-CMS. Similarly, IPSL-LR has low horizontal resolution in both atmospheric and ocean models, whereas IPSL-MR employs medium horizontal resolutions for both models. The detailed configurations of each individual CMIP5 model can also be found in the references of Tab. 5.1, including all the information about their land and sea-ice components as well.

5.3 Mathematical framework

F_{ov} and F_{gyre} (see Eq. 4.1) are calculated using the monthly mean model output, and the derived monthly fields are averaged over each year to produce annual-mean time series. Temporal variability in the annual-mean time series of F_{ov} is decomposed into contributions from meridional velocity and salinity using the following equations:

$$F_{ov}(y) = (v \cdot S) = (\overline{v} + v')(\overline{S} + S') = \overline{v}\,\overline{S} + \overline{v}S' + v'\overline{S} + v'S' \tag{5.1}$$

$$\overline{F_{ov}}(y) = \overline{v}\,\overline{S} + \overline{v'S'} \tag{5.2}$$

$$F_{ov}{}'(y) = F_{ov}(y) - \overline{F_{ov}}(y) = \overline{v}S' + v'\overline{S} + v'S' - \overline{v'S'} \tag{5.3}$$

where y corresponds to each latitude, the overbar represents the long-term mean, the prime $'$ represents deviations from the long-term mean, and the top-to-bottom integrals of v and $-\langle S\rangle/\hat{S}$ in Eq. 4.1 are simplified to v and S, respectively. Since the term $\overline{v'S'}$ has a negligible contribution in our analyses, the final equation can then be approximated to:

$$F_{ov}{}'(y) = F_{ov}(y) - \overline{F_{ov}}(y) = \overline{v}S' + v'\overline{S} + v'S' \tag{5.4}$$

The left-hand side of Eq. 5.4 is the $F_{ov}(y)$ anomaly with its long-term mean removed at each latitude. The first and second term on the right-hand side of Eq. 5.4 represent, respectively, the contributions from salinity and velocity anomalies from their long-term means, whereas the last term denotes the covariability between salinity and velocity anomalies.

Fields of FWC are also obtained on a monthly basis and then are averaged over each year, according to the equation:

$$FWC = -\int_{y1}^{y2}\int_{W}^{E}\int_{bot}^{sfc}\frac{S(y,x,z) - \hat{S}(y)}{\hat{S}(y)}dzdxdy \tag{5.5}$$

where salinity anomalies, relative to section averaged values ($\hat{S}$) at each latitude, are integrated from the surface to the bottom of the ocean and over a domain enclosed by two latitudes $y1$ and $y2$, and by the western (W) and eastern (E) boundaries.

The Atlantic freshwater budget is calculated for the models which have the freshwater surface fluxes already available on their ocean grids in the CMIP5 database. These models are the ones with a star before their names in Tab. 5.1. FWC changes are estimated as the difference between two successive months of January, following the same approach employed by *Deshayes et al.* (2014) in a CMIP5 model intercomparison of North Atlantic freshwater budgets. Changes in FWC can be attributed to combinations of surface fluxes, advective and diffusive fluxes of freshwater across all lateral boundaries of the budget domain. However, similarly to *Deshayes et al.* (2014), a budget residual term had to be considered due to missing components in the CMIP5 database: (i) diffusive fluxes are not available in the CMIP5 database for any chosen model in Tab. 5.1; and (ii) the parameterized contribution of resolved mesoscale processes to tracer advection, i.e. Gent-McWilliams (GM) parameterization (*Gent and McWilliams*, 1990), is also not available for these models. Even with these approxima-

tions, the Atlantic freshwater budgets are nearly closed on different timescales, with the residuals having a much smaller variability than the other budget terms, as discussed in Tab. 5.2. The freshwater budget equation is described as follows:

$$F^N - F^S = E - P + R + RES \tag{5.6}$$

where F^N and F^S respectively correspond to the total freshwater transports at the northern and southern boundaries, E-P+R represents the evaporation minus precipitation plus runoff, and RES is the residual term.

In order to evaluate the main drivers of FWC changes between any two latitudes in the Atlantic, the covariance of each budget term with FWC changes is normalised by the variance of FWC changes, as shown by the following equation:

$$\begin{aligned} &\frac{cov(F^S_{ov}, FWC)}{\sigma^2(FWC)} + \frac{cov(F^S_{gyre}, FWC)}{\sigma^2(FWC)} + \frac{cov(F^N_{ov}, FWC)}{\sigma^2(FWC)} + \frac{cov(F^N_{gyre}, FWC)}{\sigma^2(FWC)} + \\ &\frac{cov(E - P + R, FWC)}{\sigma^2(FWC)} + \frac{cov(RES, FWC)}{\sigma^2(FWC)} = \frac{cov(FWC, FWC)}{\sigma^2(FWC)} = 1 \end{aligned} \tag{5.7}$$

The sum of all the terms in Eq. 5.7 must be 1. It is also worth noting that all the analyses are performed on the original model grid and the time-series have their linear trends removed.

5.4 Mean state

Figure 5.1 shows the zonally averaged salinity biases relative to EN4.2.1 for the two CMIP5 groups based on F_{ov} sign at 34°S. The time interval chosen in EN4.2.1 is from 1900 to 1915 as this might represent more consistently pre-industrial conditions rather than longer time intervals. The CMIP5 salinity biases are quite uniform throughout the basin, but show different vertical distributions between the two groups. Models with positive F^{34S}_{ov} (Fig. 5.1a) have a notable near surface layer of negative S biases up

to -1.5 psu, which is counteracted by a much deeper layer of positive S biases, between 0.3 and 0.6 psu, extending to the ocean bottom. In contrast, models with negative F_{ov}^{34S} (Fig. 5.1b) show opposite vertical distributions, with negative S biases in the bottom layer being compensated by a layer above of predominantly positive S biases.

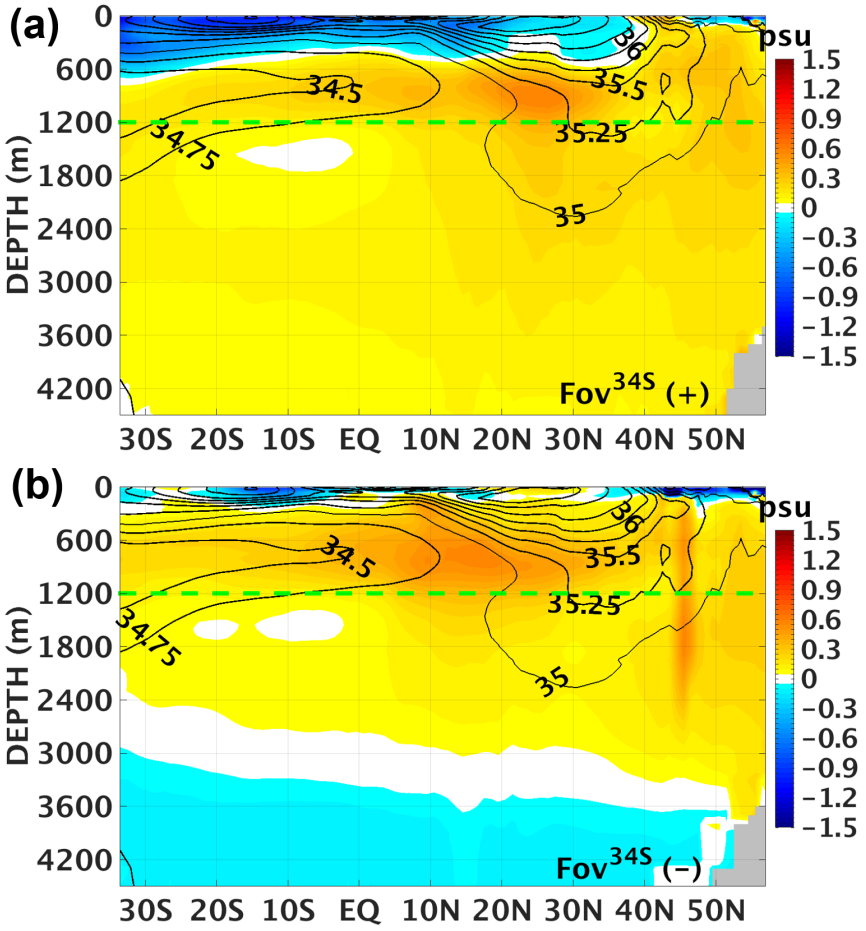

Figure 5.1: The zonally averaged salinity biases (psu) relative to the 1900-1915 EN4.2.1. Figures (a) and (b) represent the ensemble mean of CMIP5 models with positive and negative F_{ov} at 34°S, respectively. The black contours correspond to the zonally averaged salinities from EN4.2.1. The green dashed lines represent the depth of 1200 m.

The advection of large positive and negative S biases within different depth ranges may be associated with salinity discrepancies in the formation region of water masses (*Sallée et al.*, 2013; *Zhu et al.*, 2018). For example, according to Fig. 5.2a, all models

with positive F_{ov}^{34S} have their salinity minimum located between 300 m and 600 m, indicating a shallow AAIW. This upward displacement of the AAIW position is consistent with fresh waters near the surface in the South Atlantic, followed by salty waters below (Fig. 5.1a). Although models with negative F_{ov}^{34S} better reproduce the AAIW position and the upper salinity structure in the southern Atlantic, their AAIWs are still ~0.3 psu saltier than EN4.2.1 (Fig. 5.2b), consistent with the advection of positive S biases in the upper 1200 m (Fig. 5.1b).

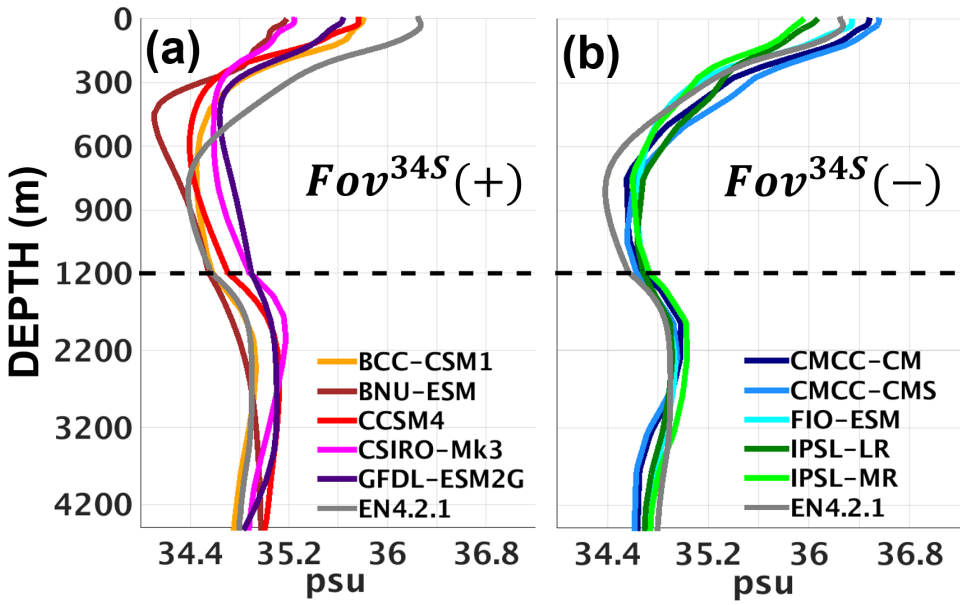

Figure 5.2: The zonally averaged salinity profiles between 34°S and 20°S for the 10 chosen CMIP5 models, divided into groups with (a) positive and (b) negative F_{ov}^{34S}. The 1900-1915 EN4.2.1 is also shown for comparison. Note the stretched vertical axis in (a) and (b) between 0-1200 m, compared to 1200-4500 m.

The contrasting salinity distributions, seen in Fig. 5.1a and Fig. 5.1b, result in opposite signs of ΔS_{1200m} between the two CMIP5 groups in the southern Atlantic (Fig. 5.3). In Fig. 5.2a, the 0-1200 m salinity branch is fresher than the deep branch, resulting in a negative ΔS_{1200m} and therefore in an import of freshwater into the basin by the AMOC (i.e. a positive F_{ov} at 34°S). Conversely, an upper branch saltier than the deep branch (Fig. 5.2b) develops a positive ΔS_{1200m} and a negative F_{ov} (Fig. 5.3).

In addition to F_{ov} sign, Fig. 5.3 shows that ΔS_{1200m} also controls the inter-model F_{ov} spread in the southern Atlantic, with a linear regression coefficient of 0.91 between both quantities. This is consistent with the role played by the vertical salinity contrasts in driving F_{ov}, as seen in Chapter 4, and explains the large sensitivity of the southern F_{ov} when salinity bias corrections are applied in the CMIP5 models (*Mecking et al.*, 2017).

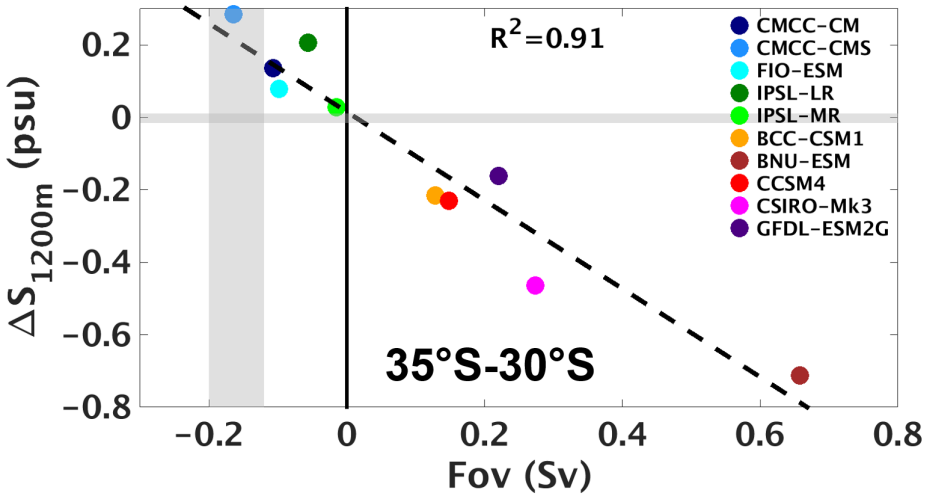

Figure 5.3: Scatter plot of mean ΔS_{1200m} and F_{ov} between 35°S and 30°S for the 10 chosen CMIP5 models. The vertical grey shading represents F_{ov} observational estimates in the southern Atlantic from *Garzoli et al.* (2013), whereas the horizontal grey shading corresponds to the annual range of 1900-1915 EN4.2.1 ΔS_{1200m}.

The ΔS_{1200m} influence over F_{ov} also extends throughout the basin (Fig. 5.4). The CMIP5 models with negative F_{ov}^{34S} show less spread in ΔS_{1200m} (Fig. 5.4b) than models with positive F_{ov}^{34S} (Fig. 5.4a), consistent with Fig. 5.2. As a result, the inter-model spread in F_{ov} is smaller in the former (Fig. 5.4d) than in the latter group (Fig. 5.4c). However, the inter-model spread of both CMIP5 groups is much larger than the inter-model spreads in ΔS_{1200m} and F_{ov} exhibited by the FRMs and ORAs from Tab. 2.1, which all have mean values close to zero in the South Atlantic. Obviously, one would expect salinity drifts to develop in such long spin-up CMIP5 runs, limiting these unconstrained models to properly represent the mean vertical salinity distributions and therefore the mean F_{ov} across the basin.

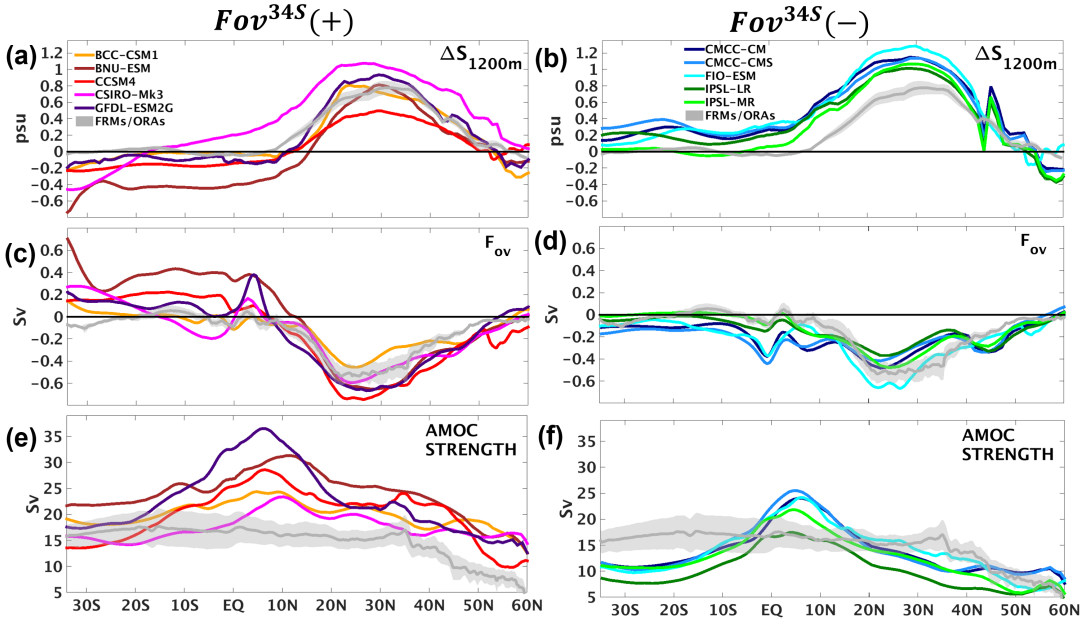

Figure 5.4: The mean (a, b) ΔS_{1200m} (psu), (b, c) F_{ov} (Sv) and (d, e) AMOC strength (Sv), divided into two CMIP5 groups of positive and negative F_{ov}^{34S}, respectively. The grey shading corresponds to the inter-model range from the ensemble of FRMs and ORAs (Tab. 2.1).

Despite the large ΔS_{1200m} differences relative to the FRMs and ORAs, those CMIP5 models with large cancellation of vertical salinity biases seen in Fig. 5.1 can still show a ΔS_{1200m} very close to zero in the South Atlantic, such as IPSL-MR (Fig. 5.4b). Consistent with the findings of Chapter 4, the negligible ΔS_{1200m} of IPSL-MR produces a very small South Atlantic F_{ov}. A very similar situation also occurs with the BCC-CSM1 model (Fig. 5.4a), particularly between 20°S and 10°N. Other models, such as CSIRO-Mk3 and BNU-ESM, show more extreme patterns of ΔS_{1200m} and therefore F_{ov} in the South Atlantic. CSIRO-Mk3 F_{ov} decreases almost linearly from ~0.3 Sv to -0.2 Sv throughout the South Atlantic, matching the almost linear increase of ΔS_{1200m} within the same latitudes. Due to its very fresh 0-1200 m branch (Fig. 5.2), BNU-ESM has the largest ΔS_{1200m} and F_{ov} magnitudes among these CMIP5 models in the South Atlantic, which is even comparable to their peaks in the subtropical North Atlantic.

In Fig. 5.4e-f models with positive F_{ov}^{34S} have larger AMOC strengths than models

with negative F_{ov}^{34S}. In fact, *Mecking et al.* (2017) show that there is an inter-model correlation of 0.73 between the AMOC strength at 26.5°N and F_{ov}^{34S}, which is driven by salinity biases in CMIP5 models. According to *Mecking et al.* (2017), CMIP5 models with stronger AMOCs lead to warmer SSTs and therefore more evaporation in the North Atlantic, which makes this region saltier. The salinification of the North Atlantic basin is then counteracted by a freshwater import by the AMOC in the near surface layers of the southern Atlantic, consistent with the vertical salinity biases (Fig. 5.1a) and the positive F_{ov}^{34S} (Fig. 5.4c) in this region. Conversely, models with weaker AMOCs would have less evaporation in the North Atlantic and less import of freshwater through the surface layers of the southern Atlantic, showing a vertical salinity bias structure (Fig. 5.1b) which favours a negative F_{ov}^{34S} (Fig. 5.4d).

Despite the large AMOC strength differences between the two groups of CMIP5 models, the interannual AMOC variability at 34°S and 26°N is insensitive to F_{ov} sign and magnitude at 34°S, with very small linear regression coefficients of 0.05 and 0.09, respectively (Fig. 5.5).

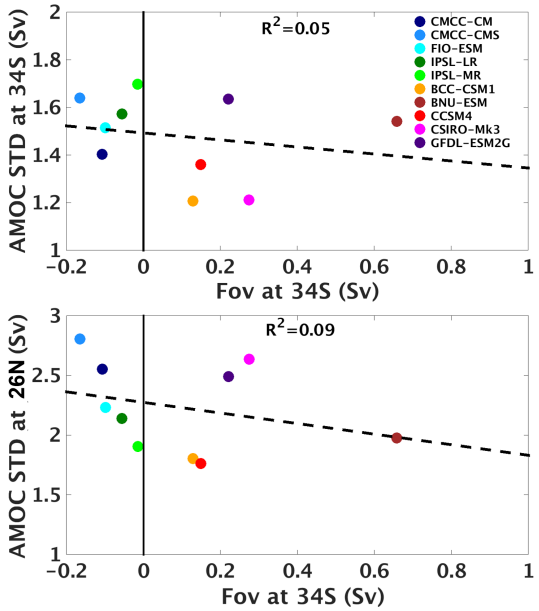

Figure 5.5: Scatter plot of interannual AMOC variability (Sv) at 34°S (top) and at 26°N (bottom) against F_{ov} (Sv) at 34°S for the 10 CMIP5 models.

5.5 F_{ov} time components

An implicit assumption of the salt-advection feedback proposed by box-models (Fig. 1.7) is that F_{ov} variability is primarily determined by the meridional velocity variability rather than by the salinity variability throughout the Atlantic (*Rahmstorf*, 1996). Fig. 5.6 shows the decadal F_{ov} variability in the southern Atlantic decomposed into salinity and velocity variations, together with the contributions due to their covariability (see Eq. 5.4). Regardless of F_{ov}^{34S} sign, 7 out of 10 CMIP5 models in Tab. 5.1 have a southern F_{ov} variability that is more correlated with local salinity variations than with local circulation changes. Specifically, in BCC-CSM1 and GFDL-ESM2G, $\overline{v}S'$ accounts for 93% and 96% of the southern F_{ov} variability, much larger than the contribution of 28% and 43% from $v'\overline{S}$, respectively. Although the relative contribution of meridional velocity anomalies are more relevant in CSIRO-Mk3, CCSM4, CMCC-CM, FIO-ESM and IPSL-MR, these models still show a greater dominance of $\overline{v}S'$ over $v'\overline{S}$ on decadal timescales.

Unlike the southern Atlantic, the region between 26°N and 40°N shows a clear dominance of the meridional velocity anomalies in determining F'_{ov} for all the 10 CMIP5 models (Fig. 5.7). The contributions of salinity anomalies to F'_{ov} largely decrease in this region, and for some models $\overline{v}S'$ has comparable contributions to $v'S'$, which is a very small term in both Fig. 5.6 and Fig. 5.7. Our findings are consistent with *Cheng et al.* (2018), which show that the decadal F_{ov} variability in two other CMIP5 models are mostly dominated by salinity variations, except in the subtropical North Atlantic (i.e. 20°N-40°N).

In order to investigate how meridional velocity and salinity anomalies contribute to F'_{ov} on different timescales, Fig. 5.8 and Fig. 5.9 display the R^2 coefficient of F'_{ov} with $\overline{v}S'$ and $v'\overline{S}$ in the South and North Atlantic, respectively, as a function of timescale. In the former region (Fig. 5.8), many CMIP5 models show a rapid increase (decrease) of $\overline{v}S'$ ($v'\overline{S}$) contributions with increasing timescale. In models belonging to

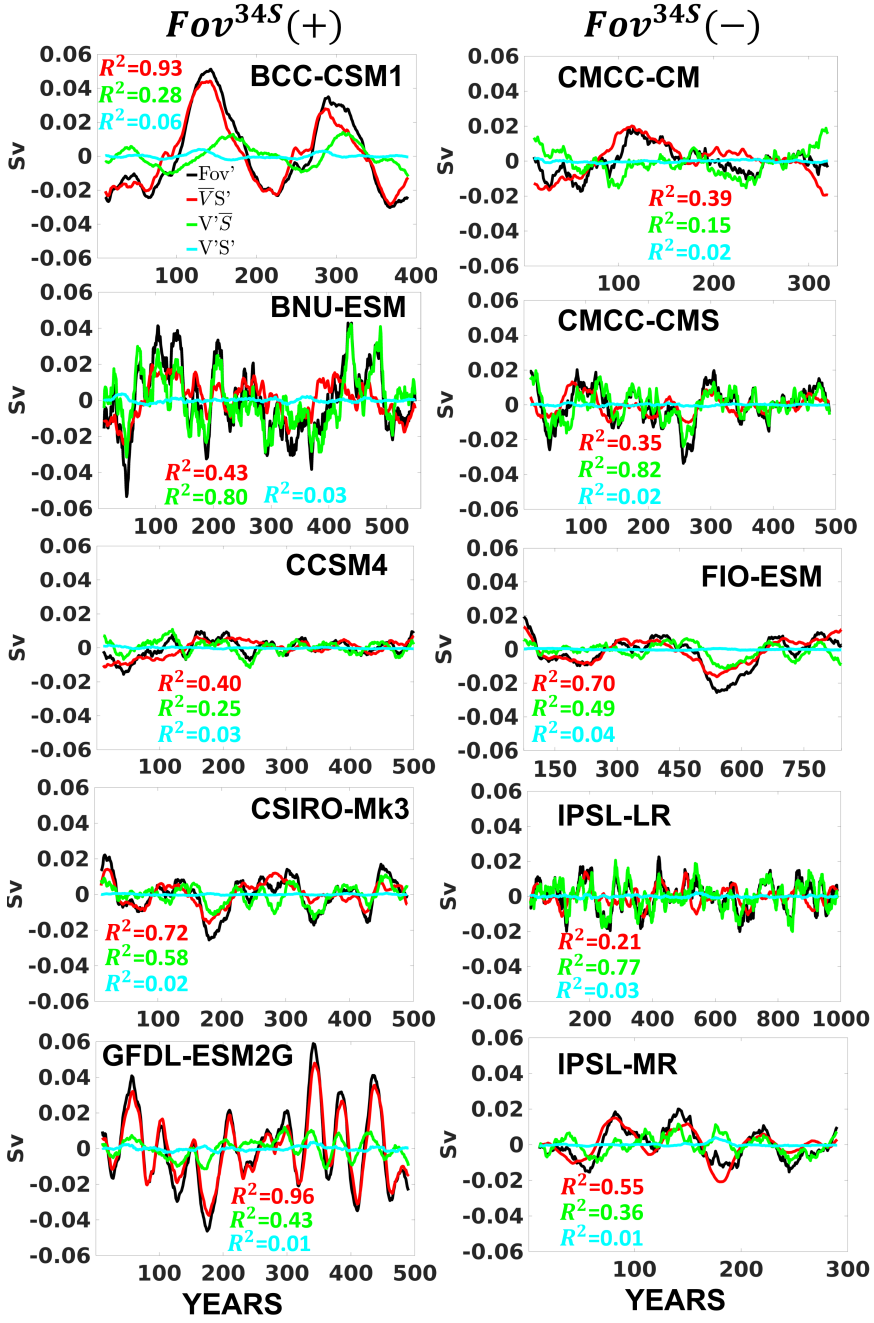

Figure 5.6: Eleven-point running averages of the annual-mean time series of F'_{ov} (black lines; Sv), with contributions from salinity (red line) and velocity (green line) variability, as well as from their covariability (cyan line) for the region between 34°S and 20°S. The R^2 values between F'_{ov} and its components are indicated by the respective colors. The CMIP5 groups with positive and negative F^{34S}_{ov} are displayed on the left and right panels, respectively. Note the different time intervals for each CMIP5 model.

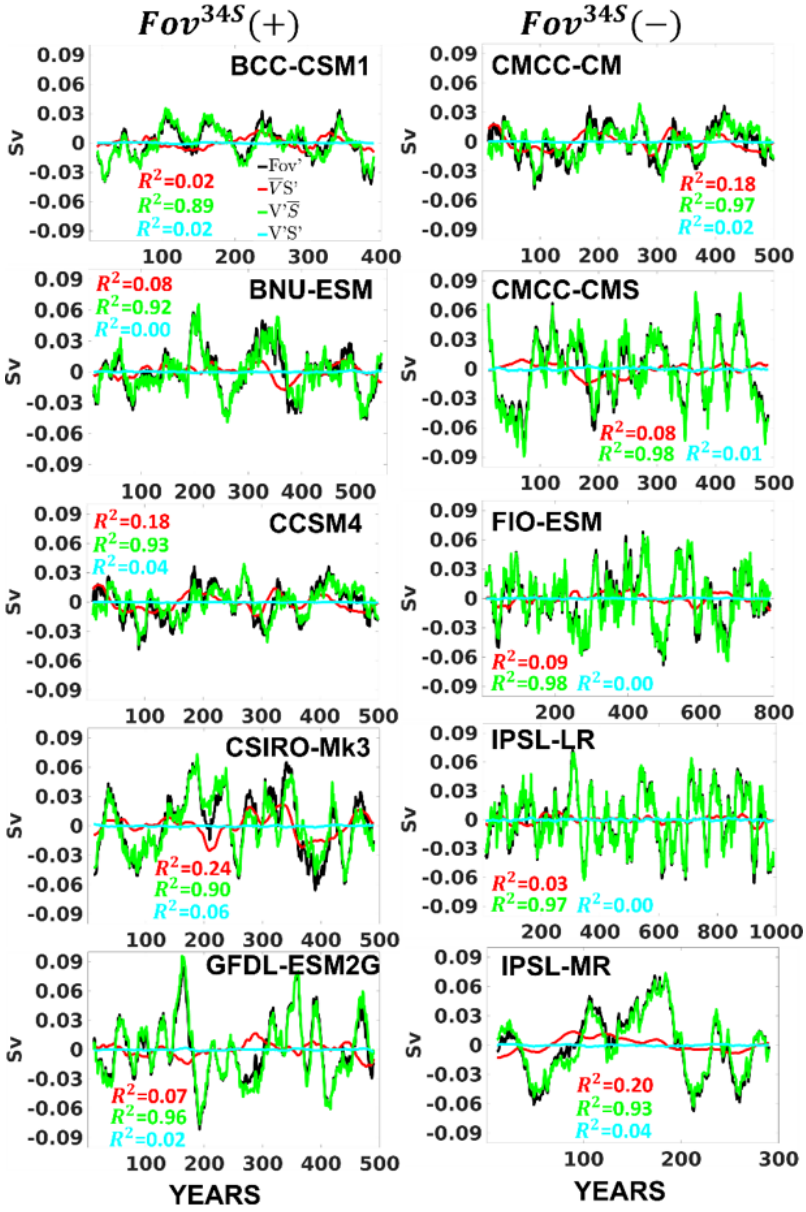

Figure 5.7: Eleven-point running averages of the annual-mean time series of F'_{ov} (black lines; Sv), with respective contributions from salinity (red line) and velocity (green line) variability, as well as from their covariability (cyan line) for the region between 26°N and 40°N. The R^2 values between F'_{ov} and its components are indicated by the respective colors. The CMIP5 groups with positive and negative F_{ov}^{34S} are displayed on the left and right panels, respectively. Note the different time intervals for each CMIP5 model.

both F_{ov}^{34S} groups, such as CCSM4, CSIRO-Mk3, CMCC-CM, FIO-ESM and IPSL-MR, $\overline{v}S'$ becomes larger than $v'\overline{S}$ contributions on timescales greater than approximately 5

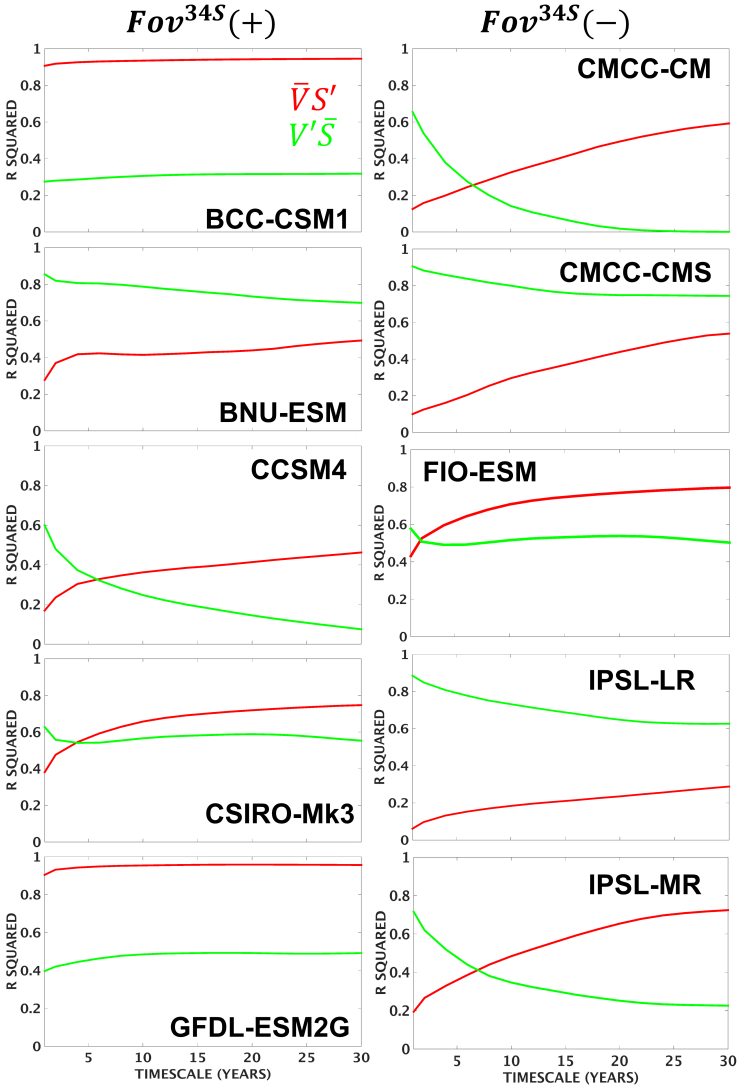

Figure 5.8: R^2 of F_{ov} anomalies with its contributions from salinity (red) and velocity (green) anomalies, as a function of timescale, considering the region from 34°S to 20°S. The CMIP5 models with positive and negative F_{ov}^{34S} are displayed on the left and right panels, respectively.

years in the southern Atlantic. In models with southern F_{ov} variability driven almost entirely by salinity variations, such as BCC-CSM1 and GFDL-ESM2G (Fig. 5.6), $\overline{v}S'$ dominates F'_{ov} contributions from interannual timescales. In the North Atlantic (between 26°N and 40°N), consistent with the large dominance of $v'\overline{S}$ in Fig. 5.7, the local circulation changes control F_{ov} variability on all timescales (Fig. 5.9).

A similar decomposition can also be done for ΔS_{1200m} anomalies. Fig. 5.10 dis-

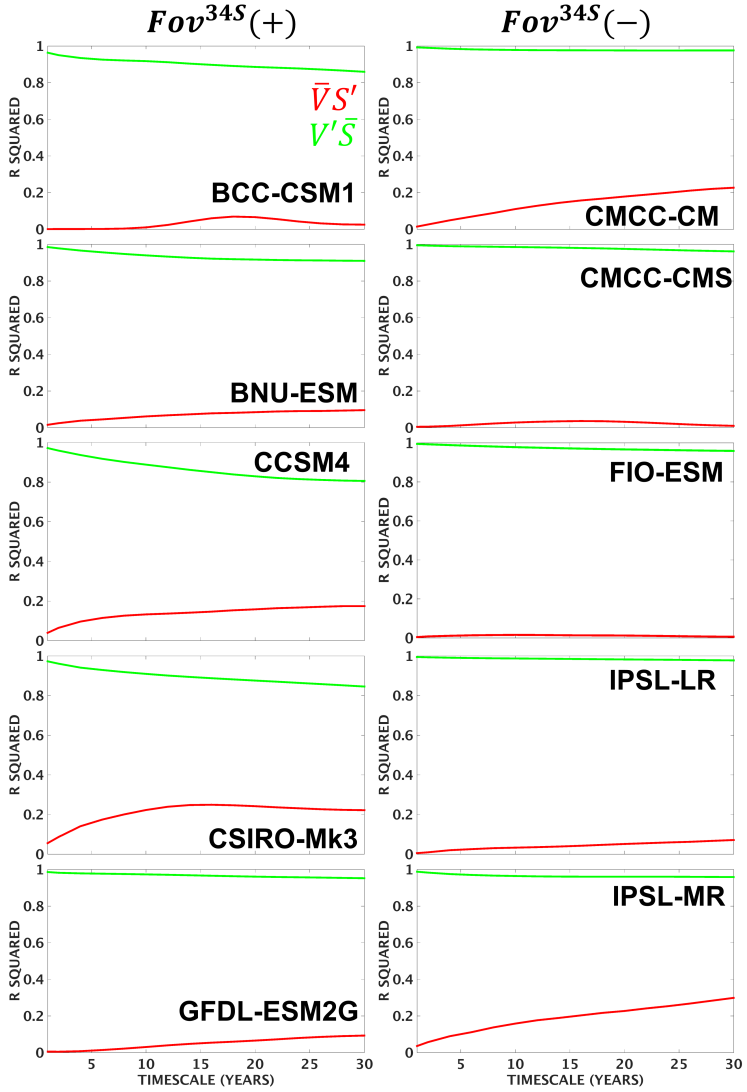

Figure 5.9: R^2 of F_{ov} anomalies with its contributions from salinity (red) and velocity (green) anomalies, as a function of timescale, considering the region from 26°N to 40°N. The CMIP5 models with positive and negative F_{ov}^{34S} are displayed on the left and right panels, respectively.

plays the annual-mean time series of ΔS_{1200m} anomalies throughout the Atlantic for each CMIP5 model, and contributions from the upper and lower S anomalies. In all models and in EN4.2.1, ΔS_{1200m} anomalies are primarily driven by 0-1200 m salinity variations. The deep salinity anomalies become larger north of ∼30°N only in a few models, showing a more meridionally coherent pattern and a much lower frequency variability when compared to the upper salinity anomalies.

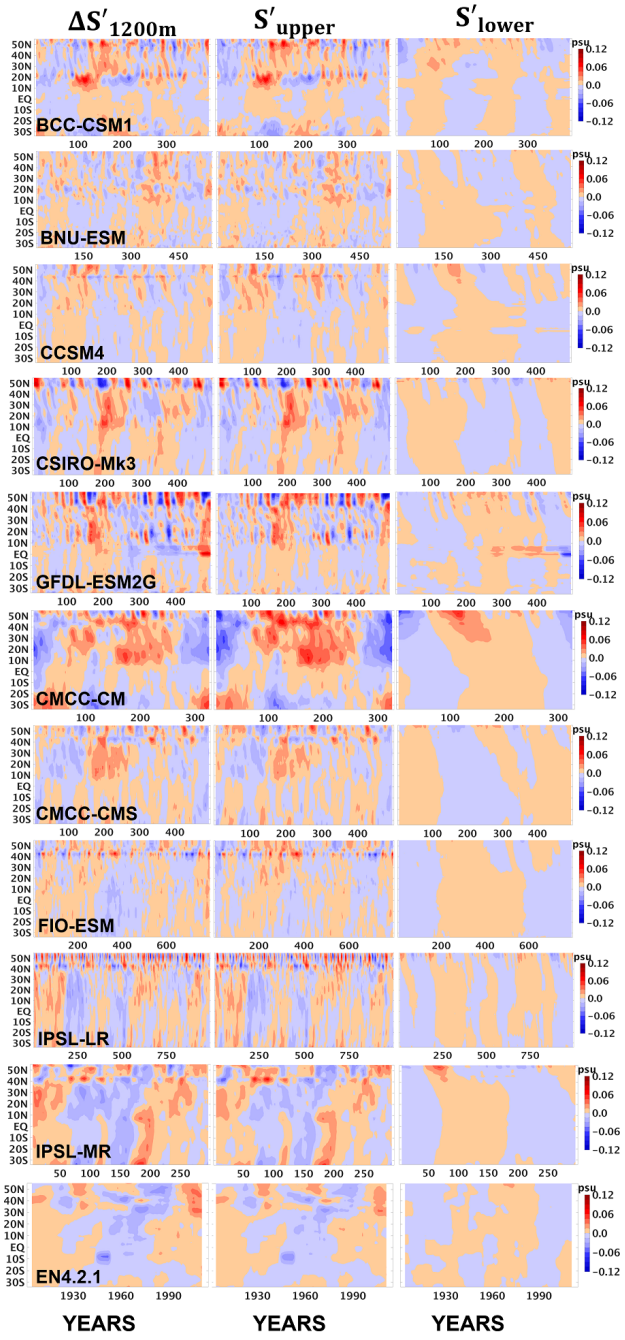

Figure 5.10: Eleven-point running averages of annual-mean ΔS_{1200m} anomalies (psu) decomposed into contributions from upper salinity anomalies (0-1200 m) and lower salinity anomalies (1200 m-bottom) for all the 10 CMIP5 models in Tab. 5.1. The bottom panel corresponds to 1900-1915 EN4.2.1 data. Note the different time intervals for each CMIP5 model.

Although upper salinity anomalies dominate ΔS_{1200m} variability, their amplitudes greatly vary between the CMIP5 models. Even within models, ΔS_{1200m} anomalies have different amplitudes throughout the basin. In several models, and in EN4.2.1, ΔS_{1200m} anomalies are larger in the northern rather than in the southern Atlantic. For instance, GFDL-ESM2G and CSIRO-Mk3 show ΔS_{1200m} anomalies mainly ranging from -0.01 to 0.01 psu south of ∼10°N, whereas north of ∼10°N they lie within a much greater range, i.e. from approximately -0.08 to 0.08 psu. These meridional differences, particularly in terms of FWC, are evaluated in the next section.

5.6 Changes in freshwater content

One of the key salt-advection feedback assumptions in box-models is that changes in the southern F_{ov} perturb the meridional density differences between the southern ocean and the northern Atlantic, and as such, they feedback on the northern AMOC (*Rahmstorf*, 1996; *Cheng et al.*, 2018). We follow the same domains as in *Cheng et al.* (2018) to evaluate the relative importance of the southern ocean (54°S-34°S) and the northern Atlantic (45°N-65°N) in determining the variability of top-to-bottom meridional FWC differences. As seen in Fig. 5.11 for all CMIP5 models and EN4.2.1, 45°N-65°N FWC changes explain much more of the north-south FWC differences than 54°S-34°S FWC changes, on decadal time scales. The dominance of the northern Atlantic FWC in setting the variability of north-south FWC gradients is reinforced by their large R^2, above 0.7 in almost all CMIP5 models, regardless of their F_{ov}^{34S} sign. This is also supported by the larger amplitudes of 0-1200 m salinity anomalies in the northern rather than in the southern Atlantic for several CMIP5 models in Fig. 5.10.

Freshwater budgets can also be a very useful approach to test whether F_{ov} at 34°S is the main driver of meridional FWC perturbations, seeking for complementary findings relative to the results in Fig. 5.11. Therefore, Tab. 5.2 shows the freshwater budget components between 34°S and 40°N on decadal timescales. This is done only

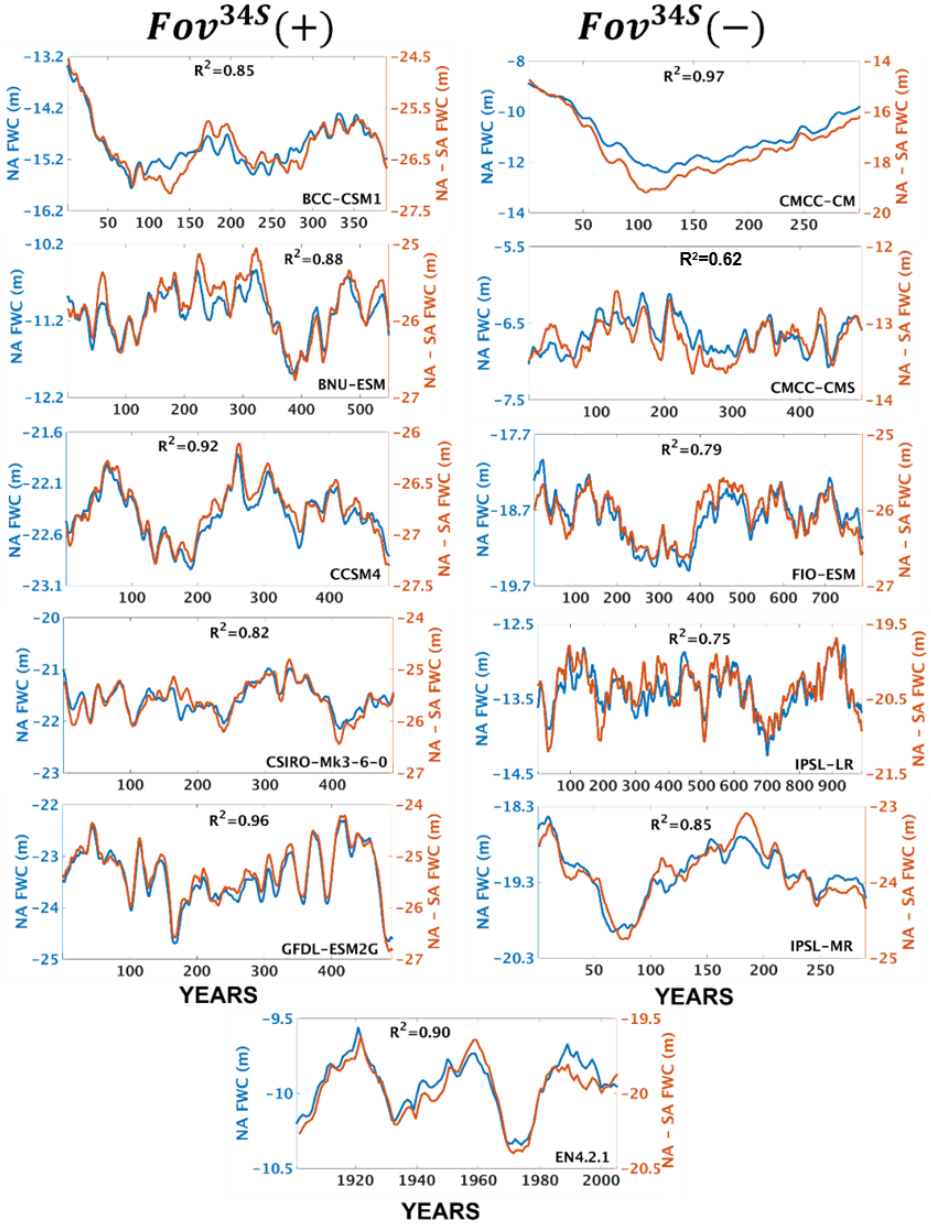

Figure 5.11: Eleven-point running means of the zonally averaged northern Atlantic FWC (m) in blue, plotted against the difference between the zonally averaged northern Atlantic and southern ocean FWC (m) in orange. The evaluated regions are 54°S-34°S and 45°N-65°N, respectively. The CMIP5 models are divided into groups with positive (left panel) and negative (right panel) F_{ov}^{34S}. The bottom centered figure corresponds to EN4.2.1. Note the different time intervals for each CMIP5 model and EN4.

for models in Tab. 5.1 which have the surface freshwater fluxes already available on their ocean grids in the CMIP5 database. It is worth noting that the budgets do not include lateral diffusion terms and the effects of GM parameterizations. Even with these approximations, the variability of the budget residuals is small when compared to other terms in Tab. 5.2. A budget residual term was also considered by *Deshayes et al.* (2014) in the North Atlantic freshwater budgets using several CMIP5 models. Only one model used by *Deshayes et al.* (2014) had available lateral diffusion and GM components, with these two terms contributing very little to the budget variability from interannual to multidecadal timescales.

Table 5.2: Decadal freshwater budget components (mSv) and their variability between 34°S and 40°N. The second and third columns represent the total freshwater transport at 34°S and 40°N, respectively, whereas the fourth column corresponds to the freshwater transport convergence into this region. CMIP5 models above and below the thick solid line have negative and positive F_{ov}^{34S}, respectively. The sign is positive when the flux is into the budget domain, and vice-versa.

Model	FWT 34°S (mSv)	FWT 40°N (mSv)	FWT conv. (mSv)	E-P+R (mSv)	FWC changes (mSv)	Residual (mSv)
CMCC-CM	263 ± 19	442 ± 38	705 ± 43	-817 ± 39	-5 ± 39	107 ± 8
CMCC-CMS	194 ± 29	477 ± 32	671 ± 39	-760 ± 44	-1 ± 35	88 ± 9
ISPL-LR	273 ± 22	489 ± 39	762 ± 44	-853 ± 28	0 ± 38	91 ± 11
IPSL-MR	361 ± 23	519 ± 30	880 ± 32	-996 ± 40	-3 ± 31	113 ± 6
CSIRO-Mk3	480 ± 19	441 ± 38	921 ± 45	-1012 ± 29	-9 ± 41	82 ± 8
GFDL-ESM2G	373 ± 32	518 ± 47	891 ± 58	-957 ± 40	0 ± 52	64 ± 13

The decadal variability of the freshwater transport convergence, i.e. the sum of freshwater transports at 34°S and 40°N, is dominated by its northern boundary transports in almost all models from Tab. 5.2. The total freshwater transport variability at 40°N can be double the transport variability at 34°S for some models, such as CMCC-CM and CSIRO-Mk3. The only exception is CMCC-CMS, which shows equivalent southern and northern transport variability, and CMCC-CMS is the only model with decadal FWC variability in the northern Atlantic explaining less than 70% of the north-south FWC differences (Fig. 5.11). Although most CMIP5 models in Tab. 5.2 agree

on the dominance of the northern over the southern transport variability, the resulting freshwater transport convergence does not necessarily represent the largest contribution to the decadal FWC budget changes between 34°S and 40°N. For instance, E-P+R shows slightly greater decadal variability than the freshwater transport convergence in CMCC-CMS and IPSL-MR.

Considering the mean states, models with positive F_{ov}^{34S} and therefore stronger AMOCs (Fig. 5.4), such as CSIRO-Mk3 and GFDL-ESM2G, do have larger negative values of E-P+R compared to most of the models with negative F_{ov}^{34S} in Tab. 5.2. This supports our previous discussion, based on *Mecking et al.* (2017), that models with stronger AMOCs lead to warmer SSTs, more evaporation and a saltier North Atlantic, which is then balanced by an import of freshwater into the basin by the AMOC, resulting in a positive F_{ov}^{34S}.

The contributions of the budget components in explaining FWC changes between 34°S and 40°N are evaluated on a range of timescales in Fig. 5.12. This is done by calculating the covariance of each budget term with FWC changes, normalised by the variance of FWC changes (see Eq. 5.7). Therefore, all the normalised covariances, including from the residuals, must sum to 1. In Fig. 5.12, the total freshwater transports are also decomposed into F_{ov} and F_{gyre} for a more detailed investigation of the budget contributions. The most important driver of 34°S-40°N FWC changes varies between E-P+R and the northern F_{ov}, depending on the CMIP5 model and the respective timescale. In general, there is a larger contribution of the advective fluxes, particularly the northern F_{ov}, with increasing timescale. However, it is worth noting that in some CMIP5 models, such as CMCC-CM, CMCC-CMS and IPSL-MR, the contribution of the southern F_{gyre} to 34°S-40°N FWC changes also increases with timescale, becoming the largest advective flux on multidecadal timescales.

The southern F_{ov} explains less than 12% of the total FWC changes in all models, regardless of the timescale, and its contribution to the freshwater budget between 34°S and 40°N is the smallest, apart from the residual term. Therefore, the normalised

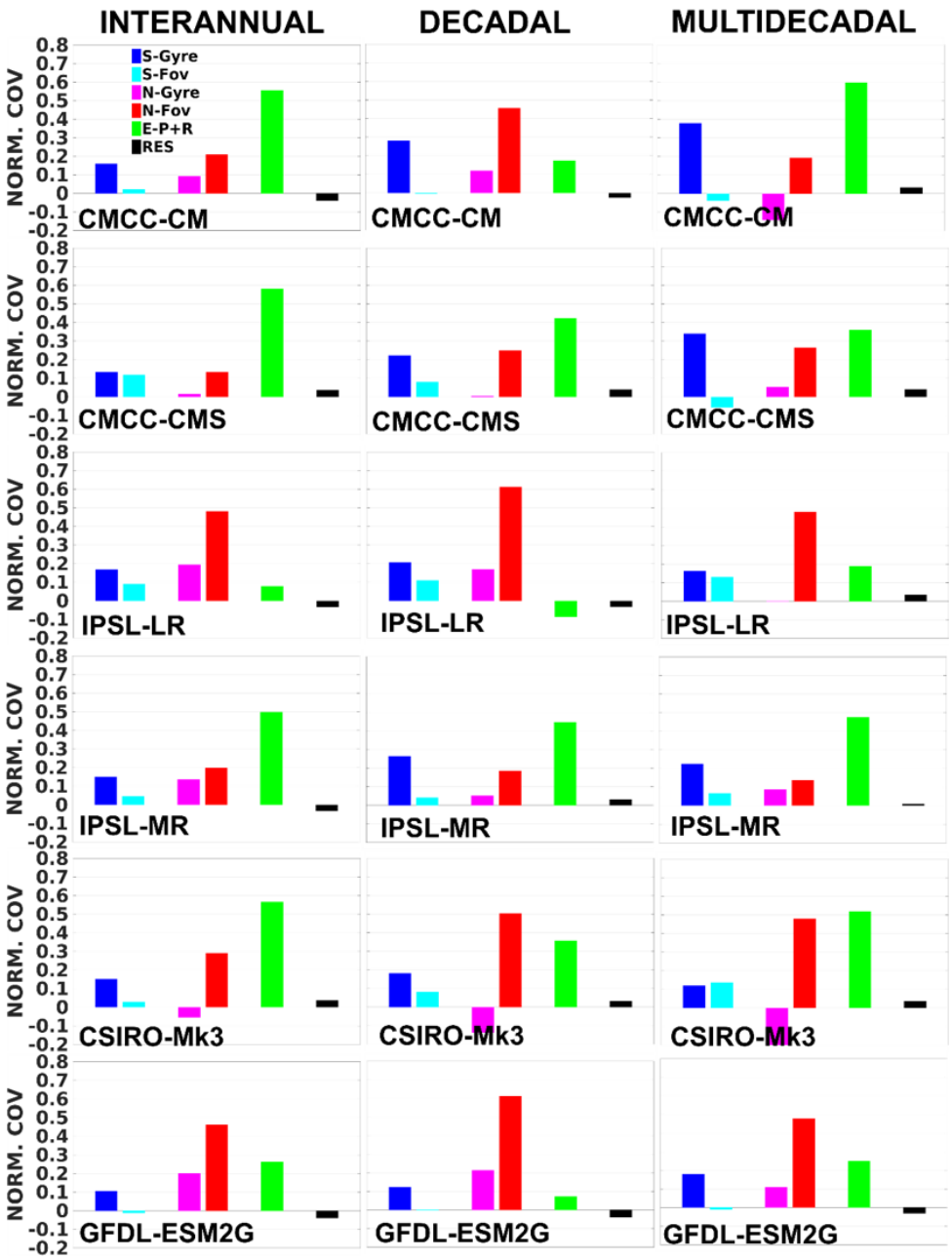

Figure 5.12: The covariance of each budget term with FWC changes normalised by the variance of FWC changes (Eq. 5.7, considering the region between 34°S and 40°N). The sum of all normalised covariances, including the one from the residual term, equals 1. The normalised covariances are evaluated on interannual, decadal and multidecadal timescales. The prefix ″S-″ and ″N-″ denote southern and northern transports, respectively.

covariance of the southern F_{gyre} with FWC changes is always equal, or more important, than for the southern F_{ov} in Fig. 5.12. These findings support previous studies, reinforcing the key role played by the southern F_{gyre} in contributing to the Atlantic freshwater budgets (e.g. *De Vries and Weber*, 2005; *Sijp*, 2012; *Ferreira et al.*, 2018).

In order to better investigate the spatio-temporal patterns of the Atlantic freshwater budgets, the normalised covariances of each budget term with FWC changes, as in Eq. 5.7, are calculated from interannual to multidecadal timescales from a fixed southern boundary at 34°S to a varying northern boundary, from 33°S up to 50°N. Figure 5.13 and Fig. 5.14 show these spatially-varying normalised covariances specifically for the southern and northern transport components, respectively, whereas Fig. 5.15 shows the total advective fluxes at the southern and northern boundaries along with E-P+R. The budget residuals are not shown since they always represent less than ∼20% of the total FWC changes in all regions and timescales in Fig. 5.15.

Therefore, Fig. 5.13 provides a complete view of how far north the southern F_{ov} and F_{gyre} influence FWC changes. Supporting the findings in Fig. 5.12, the contribution of F_{ov}^{34S} in driving FWC changes decreases rapidly moving north through the South Atlantic in all models, and is restricted to the region south of the equator. However, the influence of F_{gyre}^{34S} extends farther north in CMCC-CM, CMCC-CMS and IPSL-MR, particularly on longer timescales. In fact, the budget contributions from the total transports at 34°S are dominated by F_{gyre} rather than F_{ov}. This is true even for GFDL-ESM2G, which shows a strong compensation of the budget contributions from F_{gyre}^{34S} and F_{ov}^{34S} in the southern Atlantic. It is worth noting that F_{gyre}^{34S} mainly drives FWC changes (i.e. positive covariances) in all models, except for GFDL-ESM2G where F_{gyre}^{34S} acts to dampen FWC changes (i.e. negative covariances). Interestingly, GFDL-ESM2G is the only model with isopycnal coordinates from Tab. 5.1, whereas the other models are all based on z-levels. This very distinct behavior of GFDL-ESM2G budgets could be due to the isopycnal nature of the model, or perhaps could be associated with issues in the interpolation step from isopycnal coordinates to z-levels in the CMIP5 database.

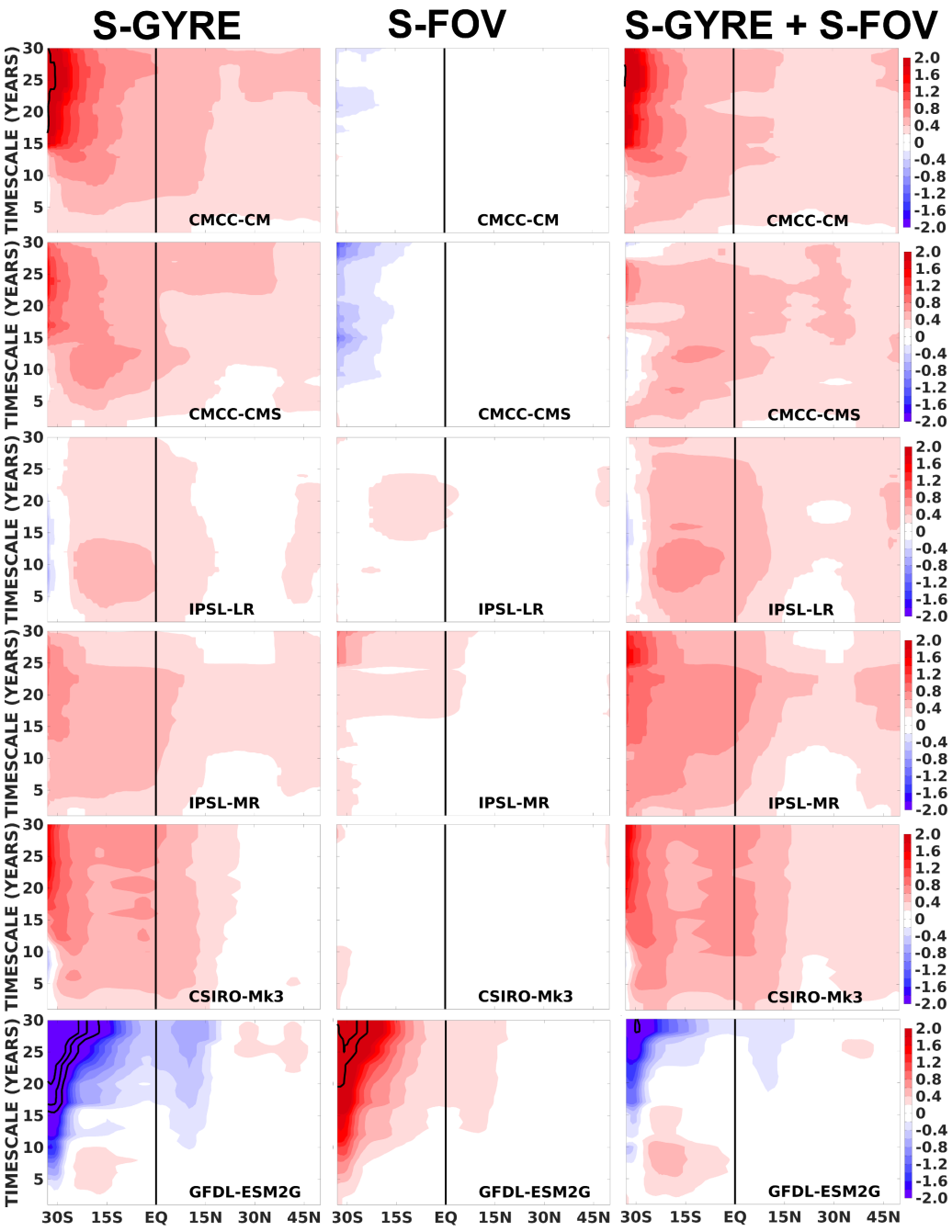

Figure 5.13: Normalised covariances of the southern F_{gyre}, F_{ov} and total transports with FWC changes as in Eq. 5.7, considering a fixed southern boundary at 34°S and a moving northern boundary from 33°S to 50°N. The spatially-varying normalised covariances are evaluated from interannual to multidecadal timescales. The black contours correspond to either negative or positive normalised covariance values of 3, 4 and 5.

F_{ov} and F_{gyre} at the northern, moving boundary usually have the same sign (Fig. 5.14) and play a role in dampening FWC changes south of ∼15°S, but this shifts to driving FWC changes north of the equator. Although they often agree on the covariance sign, when the northern boundary moves into the North Atlantic, F_{ov} becomes the dominant advective term driving FWC changes in regions further south, mostly being larger than the northern F_{gyre}. This is interesting as it reveals a change of roles between F_{gyre} and F_{ov} in the southern and northern boundaries: while F_{gyre}^{34S} is the dominant southern advection term in explaining South Atlantic FWC changes, F_{ov} becomes the dominant northern advection term in contributing to North Atlantic FWC changes. Therefore, F_{ov} is most likely to feedback with the AMOC in the North Atlantic, supporting the views of *Yin and Stouffer* (2007), *Mecking et al.* (2016) and the ORA results of Chapter 4.

E-P+R is also a strong component in both South and North Atlantic FWC variability, most of the times acting to balance the FWC changes induced by the northern freshwater transports. For example, in almost all models from Fig. 5.15, E-P+R drives long-term FWC changes south of ∼15°S, along with the southern F_{gyre}, with resultant FWC changes compensated by advective fluxes on the northern boundary. North of the equator, the balance between E-P+R and the northern advective fluxes also occurs for some models, although this is not true for all latitudes, such as for the budgets between 34°S and 40°N (see also Fig. 5.12), where both are involved in driving FWC changes.

Although there are common patterns in the budgets, such as the clear dominance of F_{gyre}^{34S} over F_{ov}^{34S} in contributing to FWC changes in the South Atlantic, it is evident that the budgets greatly vary among these CMIP5 models. Considering only the budget domain between 34°S and 40°N (Fig. 5.12), some models have E-P+R as the main driver of FWC changes, whereas other models have the advective fluxes, particularly the northern F_{ov}, as the main driver. These differences between the freshwater budgets in CMIP5 models can also be seen in Fig. 5.15, for example with GFDL-ESM2G

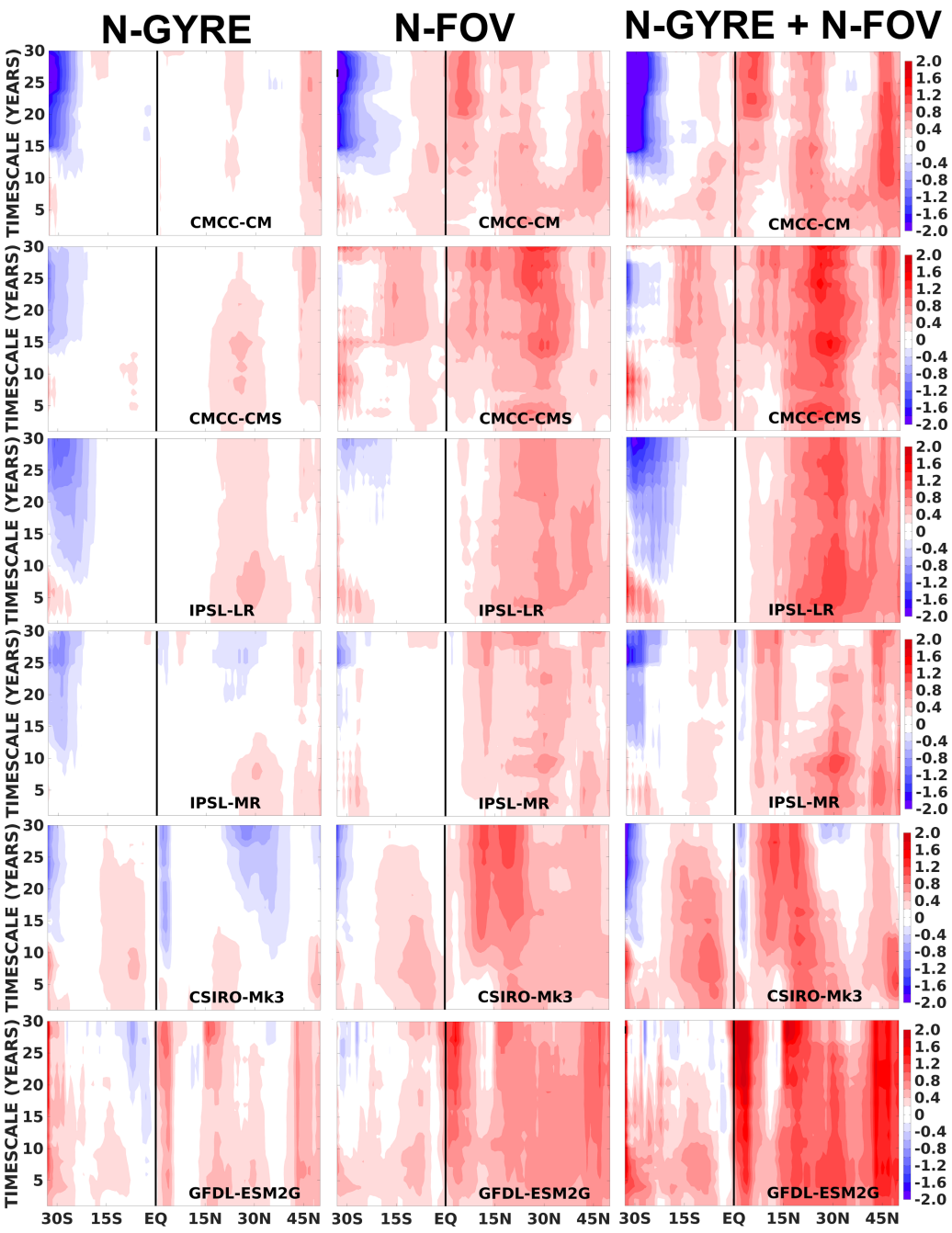

Figure 5.14: Normalised covariances of the northern F_{gyre}, F_{ov} and total transports with FWC changes as in Eq. 5.7, considering a fixed southern boundary at 34°S and a moving northern boundary from 33°S to 50°N. The spatially-varying normalised covariances are evaluated from interannual to multidecadal timescales. The black contours correspond to either negative or positive normalised covariance values of 3, 4 and 5.

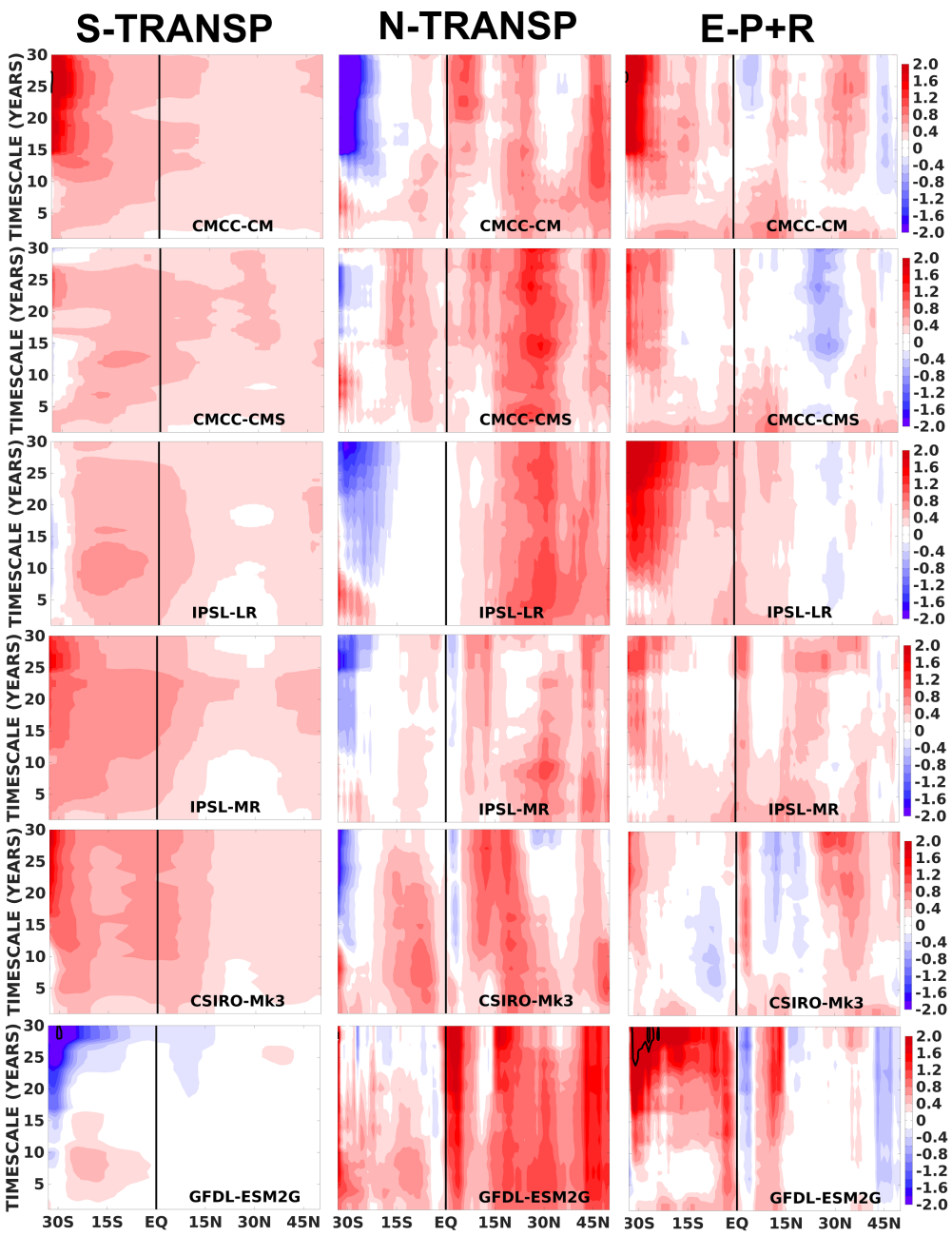

Figure 5.15: Normalised covariances of the total southern transports, total northern transports and E-P+R with FWC changes as in Eq. 5.7, considering a fixed southern boundary at 34°S and a moving northern boundary from 33°S to 50°N. The spatially-varying normalised covariances are evaluated from interannual to multidecadal timescales. The black contours correspond to either negative or positive normalised covariance values of 3, 4 and 5.

showing very different normalised covariances with FWC changes, especially in the South Atlantic, when compared to other CMIP5 models. Similar CMIP5 variations were also found by *Deshayes et al.* (2014) in the North Atlantic freshwater budgets, where the roles of surface fluxes and advection in governing FWC changes were seen to be model-dependent.

5.7 Southern F_{ov} correlations with the AMOC

In the last section, we have shown that the influence of F_{ov}^{34S} in contributing to FWC changes is restricted to the South Atlantic and is often very small. This result calls into question one of the salt-advection feedback assumptions, which states that F_{ov}^{34S} perturbs the north-south FWC gradients and therefore feeds back on the northern AMOC (*Stommel*, 1961; *Rahmstorf*, 1996). In order to better understand the relationship between F_{ov}^{34S} and the AMOC, Fig. 5.16 shows their correlations throughout the basin on a range of timescales. First, it is evident that the relationship between F_{ov}^{34S} and the AMOC is not meridionally coherent in the CMIP5 models from Tab. 5.1, with correlation values quickly approaching zero in the South Atlantic, regardless of the timescale. The only exception is CSIRO-Mk3 which shows larger correlations throughout the basin, particularly on longer timescales.

Even in the southern Atlantic, CCSM4, BCC-CSM1, GFDL-ESM2G and IPSL-MR show relatively small correlations between F_{ov}^{34S} and the AMOC, lying in the range between 0.2 and 0.5. In addition, one would expect that the correlations between F_{ov}^{34S} and the southern AMOC would increase with longer timescales, but the opposite occurs for many models in Fig. 5.16. This is explained by the increasing role of the salinity distributions in determining southern F_{ov} variations on longer timescales (Fig. 5.8). In BCC-CSM1 and GFDL-ESM2G, the salinity changes dominate the southern F_{ov} variability on interannual timescales, which is also consistent with the relatively low correlations between F_{ov}^{34S} and the southern AMOC in these models.

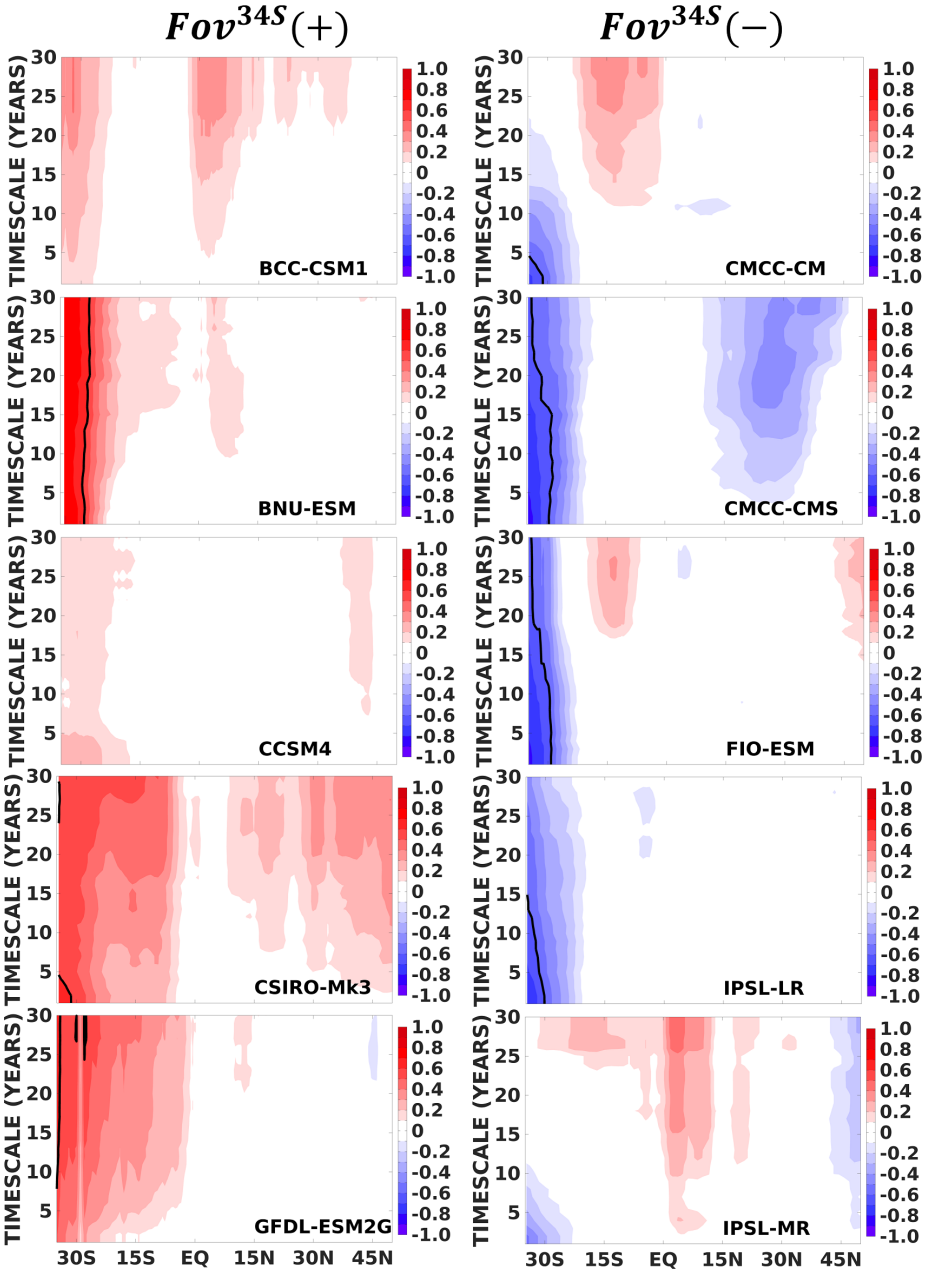

Figure 5.16: The Pearson correlation between F_{ov}^{34S} and the AMOC throughout the basin, calculated with significance level of 95% and considering from interannual to multidecadal timescales. The CMIP5 models are divided into groups with positive (left panel) and negative (right panel) F_{ov}^{34S}. The black contour corresponds to a correlation value of 0.7.

Finally, the sign of ΔS_{1200m} in the CMIP5 models determines the way F_{ov}^{34S} correlates with the AMOC in the southern Atlantic. In CMIP5 models with a positive

ΔS_{1200m}, and therefore a negative F_{ov}^{34S}, the AMOC exports freshwater out of the basin. This means that an AMOC increase results in a decrease of F_{ov}^{34S}. Conversely, in CMIP5 models with a negative ΔS_{1200m} and therefore positive F_{ov}^{34S}, an AMOC increase results in an increase of F_{ov}^{34S}. It is worth noting that ΔS_{1200m} in the southern Atlantic is close to zero in EN4.2.1, but is often biased one way or another in the CMIP5 models, ranging from approximately -0.8 psu to 0.3 psu (Fig. 5.3), and so distorting how F_{ov}^{34S} correlates with the AMOC between the two CMIP5 groups.

5.8 Discussion and Conclusions

The salt-advection feedback is characterized by a feedback loop between the AMOC, the meridional advection of salt, and the meridional density gradient, which was proposed to be triggered by changes in the southern Atlantic (Fig. 1.7). This basin-scale feedback has its origin in simple box models, but it is yet unclear how it applies to more complex climate systems. Here, we evaluate the internal variability of 10 pre-industrial CMIP5 simulations (Tab. 5.1) as an approach to investigate the robustness of the salt-advection feedback mechanisms and the timescales on which they operate. From these 10 centennial-scale simulations, two groups of five models are defined, based on the sign of F_{ov}^{34S}.

Supporting previous results of *Jackson* (2013) and *Mecking et al.* (2017), the sign of F_{ov}^{34S} in these CMIP5 models depends on their salinity biases and how these project on the salinity contrasts between the upper and lower AMOC branches (i.e. ΔS_{1200m}). Models with positive F_{ov}^{34S} have a very shallow AAIW layer, showing too fresh waters near the surface and too saline waters at depth in the South Atlantic (i.e. $\Delta S_{1200m} < 0$). Conversely, models with negative F_{ov}^{34S} have an opposite bias structure, being too saline near the surface and too fresh at deeper levels (i.e. $\Delta S_{1200m} > 0$). In addition to the sign, ΔS_{1200m} also controls the magnitude of the South Atlantic F_{ov}, explaining 90% of the inter-model spread in F_{ov}^{34S}. This reinforces the findings of Chapter 4 that F_{ov}

strength is primarily determined by the AMOC salinity contrasts, instead of by the AMOC strength throughout the South Atlantic.

The dominance of the salinity in determining the southern F_{ov} also extends to the time variability, particularly on 5-year and longer timescales. For instance, 7 out of 10 CMIP5 models have local salinity variations rather than local circulation changes determining decadal F_{ov} anomalies between 34°S and 20°S. In the northern subtropics (i.e. 26°N-40°N), however, it is the meridional velocity which clearly dominates F_{ov} variability in all models and on all timescales. Similar patterns are also noted by *Cheng et al.* (2018). They show that the long-term F_{ov} variability in two other CMIP5 simulations is governed by salinity rather than meridional velocity everywhere in the Atlantic outside of the northern subtropics. This evidence, built upon the variability of climate models, is not consistent with the box-model assumption that southern F_{ov} fluctuations are primarily dominated by local circulation rather than salinity changes, at least on 5-year and longer timescales.

The variability of the CMIP5 simulations is also used to identify how the southern F_{ov} perturbs the north-south FWC gradients, a key assumption upon which the salt-advection feedback relies (*Rahmstorf*, 1996). All CMIP5 models, and EN4.2.1, show that the meridional FWC variability on decadal time scales is primarily controlled by variability in the northern Atlantic (i.e. 45°N-65°N), rather than in the southern ocean (i.e. 54°S-34°S). This is also supported by the role of the North Atlantic in governing the long-term variability of the north-south density gradients (*Danabasoglu*, 2008; *de Boer et al.*, 2010; *Cheng et al.*, 2018).

The well determined freshwater budget variability, even neglecting GM and lateral diffusion terms, reveals that the F_{ov}^{34S} influence in explaining FWC changes is restricted to the South Atlantic and is always smaller than the influence of F_{gyre}^{34S}. This result demonstrates that the southern F_{gyre} cannot be neglected in AMOC bi-stability studies, as F_{ov}^{34S} alone cannot explain the southern transport contributions to the freshwater budgets (*De Vries and Weber*, 2005; *Mecking et al.*, 2016; *Ferreira et al.*, 2018). More

importantly, the contributions of E-P+R, driving FWC changes, and the northern transports, cancelling FWC changes, are similar or even greater than those of F_{gyre}^{34S} in the southern Atlantic freshwater budgets on multidecadal timescales. As the domain gets larger to include both the South and North Atlantic, the northern F_{ov} and its balance with E-P+R become the most important contributors to FWC changes, although F_{gyre}^{34S} contributions may also be relevant on 30-year timescales in some models. These conclusions about the budgets are underscored by the large differences across CMIP5 models. As in *Deshayes et al.* (2014), the roles of surface fluxes and advection in governing basin-wide FWC changes vary greatly depending on the specific CMIP5 model.

Consistent with the previous findings, the correlations between F_{ov}^{34S} and the AMOC are not meridionally coherent and are mostly confined to the southern Atlantic on all timescales. Even in this region, the correlations are relatively small in some models and usually decrease on longer timescales, due to the increasing role of salinity in determining the long-term F_{ov}^{34S} fluctuations. Therefore, all the evidence gathered by the internal variability of 10 centennial-scale simulations seem to refute the salt-advection feedback hypothesis from simple box-models, particularly the third assumption of Fig. 1.7 that F_{ov}^{34S} is the main driver of perturbations in the north-south density gradients. This seems to be consistent within the CMIP5 models from Tab. 5.1, regardless of their F_{ov}^{34S} sign. However, this is still a limited sample out of 44 CMIP5 models. In addition, targeted numerical experiments, where the system is forced to change more systematically than the natural variability in these control runs, may shed more light on other feedbacks and mechanisms controlling the AMOC behavior. This will be discussed as future work in Section 6.4.

CHAPTER 6

CONCLUSIONS AND FUTURE WORK

6.1 Overview

An important feature of present-day climate is that the heat transport in the Atlantic Ocean is northward in both hemispheres, rather than poleward as in the Indo-Pacific Ocean (*Ganachaud and Wunsch*, 2003) and in the atmosphere (*Trenberth and Caron*, 2001). This is due to the Atlantic Meridional Overturning Circulation (AMOC), transporting warm water northward throughout the Atlantic to compensate for the southward export of the cold North Atlantic Deep Water (NADW). The AMOC is a key contributor in the climate system. The mean ITCZ position north of the equator is argued to be the result of the northward cross-equatorial ocean heat transport achieved by the AMOC (*Frierson et al.*, 2013; *Marshall et al.*, 2013). The AMOC is also thought to be a key process by which anthropogenic heat and carbon can be transported from the surface to the deep ocean, moderating the trajectory of climate change (*Drijfhout et al.*, 2014; *Kostov et al.*, 2014). Finally, an AMOC weakening can culminate in large climate changes on both regional and global scales, including severe alterations in the surface air temperatures and precipitation patterns (*Vellinga and Wood*, 2002; *Zhang and Delworth*, 2005; *Broccoli et al.*, 2006; *Laurian et al.*, 2009; *Jackson et al.*, 2015).

Although the AMOC dynamics are extremely important for the Earth's climate, they are not yet fully understood. Several AMOC topics of research still lack a better understanding, such as: the AMOC transports and their modes of variability; the relationship between interior pathways, boundary currents and the AMOC; and the influence of meridional freshwater transports on the AMOC stability. Thus, improving our understanding of these topics has the potential to aid in making accurate climate projections, even on a global scale.

However, observing the AMOC is inherently challenging due its long timescales and large spatial extent. Trans-basin observing systems, such as the RAPID array, monitor AMOC changes at specific latitudes, but they are too sparse and only have 15 years of observational records so far. This requires the complementary use of time-evolving, three-dimensional model products to assess the ocean circulation. The aim of this thesis is to improve our understanding of the AMOC, particularly in the South Atlantic, focusing on its transport variability and feedbacks on the climate system from a variety of model products, which are: free-running models (FRMs) with distinct spatial resolutions, state-of-the art ocean reanalyses (ORAs) and coupled climate simulations.

Particularly, the use of data assimilation (DA) methods can constrain ocean models with historical observations, making the ORAs potentially useful products to assess the true strength of ocean currents, which are otherwise difficult to measure. Therefore, this thesis also explores the skills and limitations of the ORAs, by comparing them with FRMs. Intercomparisons between ORAs and FRMs give valuable insights into how ocean transports, which are not directly observed, are affected by DA (e.g. *Zuo et al.*, 2011; *Karspeck et al.*, 2015). These intercomparisons are of fundamental importance since ORAs are expected to provide transports for initialising the next generation of eddy-permitting climate models, aiming to improve decadal predictions of the AMOC and of climate (*Pohlmann et al.*, 2009; *Bellucci et al.*, 2013).

In this final Chapter, Section 6.2 provides a summary of major results achieved by this thesis, Section 6.3 addresses the research questions posed in Chapter 1, and finally

Section 6.4 discusses questions and areas of possible future investigations.

6.2 Summary of results

6.2.1 Validation of FRMs and ORAs in the South Atlantic

Five NEMO-based ORAs and two FRMs with eddy-permitting and eddy-resolving resolutions were validated with hydrographic measurements and observational studies in the South Atlantic. Two main regions were considered: (i) the southern Atlantic, where ORA and FRM transports were compared to XBT-AX18 lines at 35°S; (ii) and the NBC region in the tropical South Atlantic, where the model products were compared to western boundary velocity measurements from a moored array section at 11°S. The ORAs mainly differ by their initial conditions, their DA schemes and to some extent by the observations assimilated, as they share very similar ocean model configurations and all have the same atmospheric forcing. Key results are as follows:

- With the exception of GloSea5, the assimilation of observations systematically increases the ORA large-scale and western boundary transports relative to the FRMs in the South Atlantic. The ORA AMOC and NBC transports at 35°S and 11°S, respectively, are up to ∼6 and ∼9 Sv stronger than both FRMs with eddy-permitting and eddy-resolving resolutions, and are in closer agreement with hydrographic measurements.

- Most of the ORAs better reproduce the XBT-AX18 transport distributions of the AMOC upper branch between the western, interior and eastern boundaries at 35°S. This improved distribution of the ORA transports is consistent with their accurate positioning of the mean SSH fronts in the Brazil-Malvinas confluence with respect to AVISO SSHs. Unlike the ORAs, the Malvinas current in the FRMs, particularly in the high-resolution product, extends further north when compared to AVISO, misrepresenting the mean position of the confluence and

compromising their regional transport distributions at 35°S.

- Improvements in the ORA circulation are also seen in the South Atlantic equatorial currents, particularly in the South Equatorial Undercurrent (SEUC) and current branches (eSEC and cSEC). The ORAs show consistent SEUC, eSEC and cSEC magnitudes with respect to previous studies (e.g. *Molinari*, 1982; *Urbano et al.*, 2008), whereas in the FRMs these currents are nearly absent.

- The monthly DWBC variability at 11°S in all eddy-permitting model products is also only half of the observational estimates, since none of them reproduce DWBC flow reversals, which are associated with the breakdown of the DWBC into eddies. This is only achieved by the eddy-resolving model, suggesting that the horizontal resolution plays a role in the development of DWBC eddies.

- Although GloSea5 is considered a reference product for the North Atlantic circulation (*Jackson et al.*, 2015), our results show instead that this ORA has an anomalous circulation south of ∼20°N, misrepresenting by far the Brazil-Malvinas confluence position and the strengths of NBC, DWBC and equatorial currents. GloSea5 transports begin to drift in October 1992, precisely when the altimetry observations are introduced into the DA system.

6.2.2 South Atlantic Meridional heat and volume transports

After a detailed validation of the ORA and FRM transports at 35°S and 11°S, the benefits and limitations of DA in changing the South Atlantic meridional heat and volume transports are investigated by performing analyses to quantify relevant contributions to the inter-model transport spread. We look at how variations in temperature and meridional velocities, particularly at the western boundary compared with ocean interior, contribute to explain transport agreements and disagreements between the model products. Key results are as follows:

- The ORA basin interior circulations, in both subtropical and tropical South Atlantic, are consistently improved relative to the FRMs, with interior meridional transports converging as Argo data are introduced.

- Despite the improvements in the interior circulation, large ORA AMOC and MHT discrepancies, up to ∼8 Sv and ∼0.4 PW respectively, still remain between 35°S and the equator. These differences in the meridional transports are mainly attributed to differences in the narrow South Atlantic western boundary currents within 6° of the coast, which dominate the overturning component.

- Although DA consistently changes the upper western boundary transports in the same direction (e.g. increasing the northward NBC and decreasing the southward BC), they do not consistently constrain the boundary current transport magnitudes. The NBC explains ∼85% of the inter-product differences in the total MHTs, with compensating variations in the DWBC also close to the coast.

- The meridional velocity differences, rather than temperature differences, in the western boundary currents drive ∼83% of the MHT spread. Although much smaller, the temperature contribution to the inter-product spread in the MHT is evident right against the western boundary, where temperature differences are required to geostrophically explain the large western boundary velocity differences among products.

6.2.3 Decoupled Freshwater Transport and Meridional Overturning in the South Atlantic

In order to elucidate feedbacks between salinity distributions and the AMOC strength, the same FRMs and ORAs were used to investigate the role of vertical and horizontal salinity gradients in modulating the overturning and gyre freshwater transports, respectively. Key results are as follows:

- F_{ov} strength in the Atlantic is explained by spatial variation in the vertical salinity contrasts between the AMOC branches, i.e. ΔS_{1200m}.

- The Antarctic Intermediate Water (AAIW) layer eliminates salinity differences across the AMOC branches, i.e. ΔS_{1200m} is approximately zero, which decouples F_{ov} from the AMOC south of ~10°N. Therefore, the AMOC has very little freshwater transports in the South Atlantic, even though the AMOC itself is strong and varies greatly between the model products.

- As the AAIW disappears north of ~10°N, a large ΔS_{1200m} allows the AMOC to drive substantial southward F_{ov} in the subtropical North Atlantic.

- Total gyre freshwater transports are mainly controlled by the zonal salinity contrasts in the top 300 m, especially south of 30°N, although the gyre circulations extend deeper. These F_{gyre} transports exhibit a marked anti-symmetric pattern around the mean ITCZ location at ~5°N, redistributing freshwater within this 0-300 m ocean layer in the subtropics of both hemispheres.

- Since F_{ov} is very close to zero in the South Atlantic, F_{gyre} sets the total South Atlantic freshwater transport F_{mean}.

6.2.4 Salt-advection feedback mechanisms within CMIP5 models

The internal variability of 10 centennial-scale CMIP5 simulations, with both positive and negative F_{ov} at 34°S, were used to investigate whether salt-advection feedback mechanisms can be detected on a range of timescales. In these simulations, the greenhouse gas emissions, radiative forcing and volcanic and anthropogenic aerosols were held constant at pre-industrial levels. Key results are as follows:

- ΔS_{1200m} explains 90% of the inter-model spread in F_{ov} at 34°S, reinforcing that F_{ov} strength is primarily determined by the AMOC salinity contrasts, instead of by the AMOC strength in the southern Atlantic.

- 7 out of 10 CMIP5 models have a 34°S-20°S F_{ov} variability that is more correlated with local salinity variations than with local circulation changes on 5-year and longer timescales. In the northern subtropics (i.e. 26°N-40°N), it is the meridional velocity which clearly dominates F_{ov} variability in all models and on all timescales.

- The north-south FWC differences are primarily controlled by the variability in the northern Atlantic (i.e. 45°N-65°N) rather than in the southern ocean (i.e. 54°S-34°S) on decadal and longer timescales for all CMIP5 models and EN4.2.1.

- The freshwater budget variability reveals that the influence of F_{ov} at 34°S in explaining FWC changes is restricted to the South Atlantic and always smaller than the influence of F_{gyre} at 34°S. As the budget domain gets larger to include both the South and North Atlantic, the northern F_{ov} and its balance with E-P+R become the most important contributors to FWC changes.

- The correlations between F_{ov} at 34°S and the AMOC are mostly confined to the southern Atlantic on all timescales. Even in this region, some models actually show relatively small correlations, usually decreasing on longer timescales, due to the increasing role of salinity in controlling long-term fluctuations of the southern F_{ov}.

6.3 Conclusions and discussions of this thesis

This section addresses the research questions posed in Section 1.6 and discusses the implications of this work.

- **What are the benefits and limitations of DA in improving the simulations of the South Atlantic ocean circulations, which are otherwise difficult to measure? How sensitive are FRM and ORA heat transports with respect to variations in temperatures and meridional velocities in distinct oceanic regions?**

We show that the present ocean observation network and data assimilation schemes can be used to consistently constrain the ORA interior circulation in both structure and strength throughout the South Atlantic, which is improved with respect to the FRMs. All NEMO-based reanalyses show a great agreement in reproducing the interior transports in both subtropical and tropical South Atlantic, especially in the Argo period. As a result, both the freshwater and heat gyre components of the ORA circulations are very well constrained throughout the basin and different from the FRMs. This is in striking contrast with the large disagreement found in the ORA AMOCs and their respective MHTs, which is traced back to transport discrepancies in the western boundary currents within a few degrees of the coast. Although DA brings the transports closer to observational estimates and improves the positioning of ocean currents in the western boundary (e.g. Brazil-Malvinas confluence), they do not properly constrain the magnitude of the western boundary transports.

Despite the fact that differences in the western boundary velocities primarily dominate the inter-model spread in the MHTs, there is a small but evident contribution of the temperature differences right against the western boundary. This is geostrophically required to support the large velocity differences between the products, emphasising the large sensitivity of the western boundary currents, and therefore meridional transports, to small density changes on the western boundary slope (e.g. *Bingham and Hughes*, 2009). This may also help to understand why the MHTs of very similar NEMO-based ORA are so sensitive to DA schemes and their configurations near the western boundary. In the discussions of Chapter 3, we have argued two possible reasons for the ORA limitations in representing the western boundary transports: (i) the lack of near boundary observations, and/or (ii) the differences in DA error covariances when assimilating observations lying near to the western boundary. Both topics (i) and (ii) will be addressed as future work in Section 6.4 in order to better understand the ORA limitations.

In general lines, the message of this thesis is more encouraging than that of *Kar-*

speck et al. (2015) as it suggests that the assimilation of the current ocean observing system allows the reproduction of many aspects of the circulation in the ORAs. However, more work is required to understand how to better represent and constrain the critical western boundary currents where a lot of the climatically important heat and freshwater transport occurs. Therefore, this will still likely limit the effectiveness of ORA products for climate or decadal prediction studies, and the results of this thesis clearly indicate that improvements in the ORA western boundary transports should be quickly addressed by the climate research community.

- **What is the role of salinity in modulating freshwater transports across the Atlantic? How do FRM and ORA salinity distributions reveal climate feedbacks between F_{ov} transports and the AMOC?**

A key finding of this thesis is that, although the inter-model spread in Q_{ov} is governed by the spread in the AMOC strength, this is not the case for F_{ov}. The model products, particularly the ORAs, show a great consistency in reproducing F_{ov} throughout the Atlantic, even though they have very different AMOC strengths. This is because of the central role of the vertical salinity contrasts between the AMOC branches at ∼1200 m, ΔS_{1200m}, in determining the F_{ov} strength throughout the basin. The realistic representation of ΔS_{1200m} by the FRMs and ORAs was extremely important to clarify feedbacks between F_{ov} and the AMOC in the context of AMOC bi-stability. Using these model products with realistic salinities but quite different AMOCs, we clearly showed that the fresh AAIW layer eliminates salinity differences across the AMOC branches (i.e. ΔS_{1200m} ∼0), which decouples F_{ov} from the AMOC in the South Atlantic. This decoupling refutes the use of F_{ov} at 34°S as an indicator of the AMOC bi-stability (e.g. *Rahmstorf*, 1996), since a realistic ΔS_{1200m} effectively shuts off, or greatly weakens, first order feedbacks between the AMOC changes and F_{ov} throughout the South Atlantic. This then leaves indirect F_{gyre} feedbacks or F_{ov} in the north as more relevant factors for the AMOC bi-stability (see Fig. 6.1 for recommendations

on how to proceed understanding AMOC bi-stability). This thesis also represents a step forward relative to *Mecking et al.* (2017) since we clearly explained why F_{ov} is so dependent on the salinity biases, as noted by *Mecking et al.* (2017) when looking at CMIP5 models.

- **Can evidence for salt-advection feedback assumptions be detected in the internal variability of coupled climate simulations?**

All the evidence gathered by the internal variability of 10 centennial-scale CMIP5 simulations call into question the salt-advection feedback hypothesis from simple box-models, proposed to be triggered by changes in the southern Atlantic. We have not detected any clear evidence of the following mechanisms in the CMIP5 simulations, which *Rahmstorf* (1996)'s box-model is built upon: (i) AMOC strength influences F_{ov} at the Atlantic southern boundary, and (ii) F_{ov} at the Atlantic southern boundary then perturbs the meridional FWC difference and therefore feedback on the northern AMOC. We clearly demonstrated instead that the southern F_{ov} variability in most of the CMIP5 models is more dominated by local salinity changes rather than local circulation changes on 5-year and longer timescales, calling into question the robustness of the first box-model mechanism. The meridional FWC variability in all CMIP5 models has been shown to be primarily controlled by variability in the northern Atlantic rather than in the southern ocean, on decadal and longer timescales. Finally, the spatio-temporal variability of the Atlantic freshwater budgets revealed that the influence of F_{ov} at 34°S in explaining FWC changes is restricted to the South Atlantic and is always smaller than the influence of F_{gyre} at 34°S. Therefore, the budget analyses consistently refuted the box-model mechanism that F_{ov} at 34°S is the main driver of meridional FWC perturbations.

It should come as no surprise that coupled climate systems, containing feedbacks not captured by the box-models, are governed by different dynamics than the box-models (Fig. 6.1). This is clearly reinforced by the spatio-temporal analyses of the

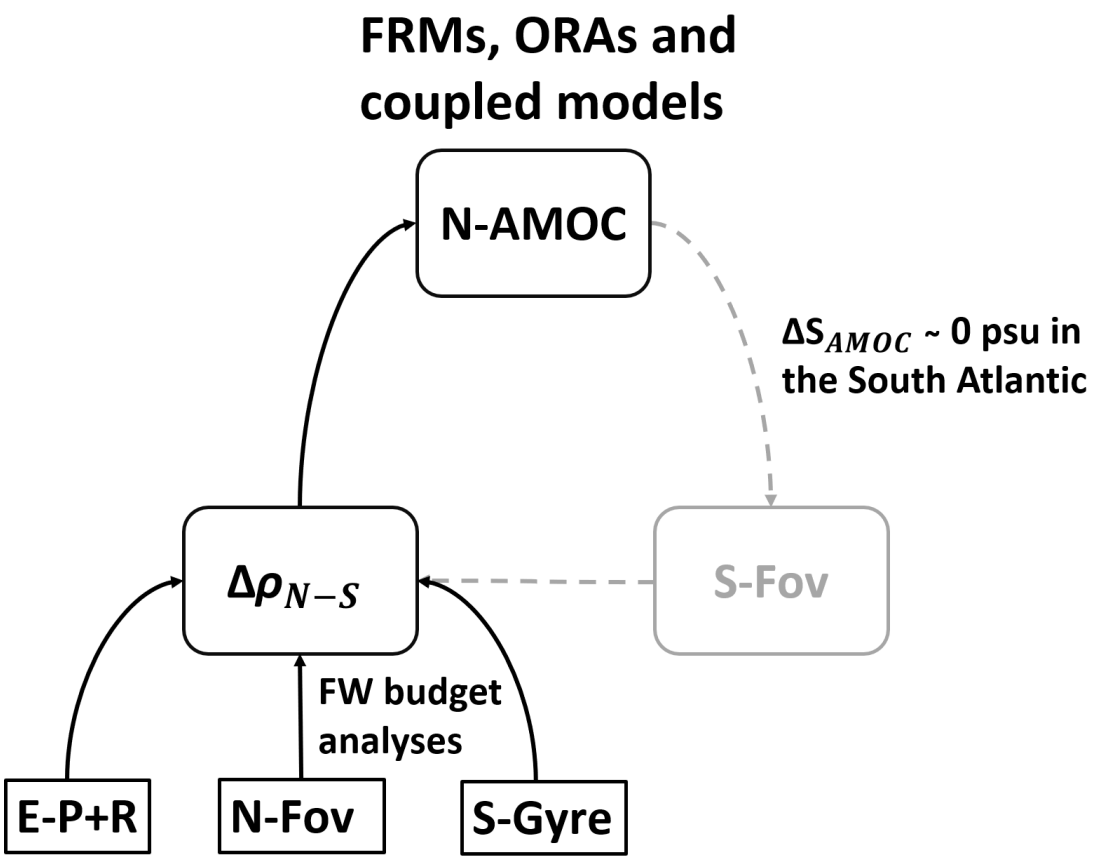

Figure 6.1: An updated schematic of Fig. 1.7 based on FRM, ORA and coupled model results, showing which salt-advection feedback assumptions in box-models have been invalidated and which new mechanisms should be considered for AMOC-bistability from now on. The grey dashed arrows and grey box represent obsolete salt-advection feedback mechanisms. The prefix ″S-″ and ″N-″ denote southern and northern Atlantic, respectively.

freshwater budget variability in CMIP5 simulations. The complete picture provided by the budget analyses represents a step forward with respect to *Cheng et al.* (2018). *Cheng et al.* (2018) also found missing links in the salt-advection feedback mechanisms within two CMIP5 simulations, but they only focused on F_{ov} and the AMOC variability, particularly on the meridional coherence and propagation properties of the signal. Here, the spatio-temporal variability of the freshwater budgets showed key contributions of F_{gyre} and E-P+R to FWC changes, even within the southern Atlantic region. The budgets also consistently revealed a change of roles between F_{gyre} and F_{ov} throughout

the basin: while F_{gyre} is the dominant advection term in explaining South Atlantic FWC changes, F_{ov} becomes the dominant advection term in contributing to North Atlantic FWC changes. Therefore, the findings of this thesis are clear with respect that the southern F_{gyre} cannot be neglected in AMOC bi-stability studies, as F_{ov} alone cannot explain the southern transport contributions to the freshwater budgets. These results also suggest that the second and third box-model mechanisms in Fig. 1.7 are no longer relevant, implying that revisions to box-models should be made to include the gyre component of the circulation (see the updated schematic in Fig. 6.1 considering new mechanisms for the AMOC bi-stability).

6.4 Potential for future work

The main results of this thesis are documented throughout this chapter, and the previous section in particular. These findings represent a substantial step in improving the understanding of the AMOC stability and the different model products used to study the ocean circulation. Nevertheless, several questions are still open and new ones have arisen from this study. Some areas of possible future investigation are briefly described below.

- **Sensitivity experiments changing DA configurations**

As noted in this thesis, the ORA spread in the AMOC strength throughout the South Atlantic narrows down to discrepancies in the western boundary currents within a few degrees of the coast. Previous studies, such as *Balmaseda et al.* (2013a) and *Stepanov et al.* (2012), showed that AMOC transports are very sensitive to the parameterization of observational errors and prescribed horizontal scales of DA error covariances near to the boundaries, respectively. As *Stepanov et al.* (2012) noted when assimilating the RAPID array into a NEMO model, even the shape of the DA error covariances (e.g. boundary-focused versus isotropic covariances) results in different AMOC transports at 26.5°N. ORA sensitivity experiments in the South Atlantic

could be better explored for future work, changing DA parameters near to the western boundary. This approach would be useful to understand how the western boundary and AMOC transports respond to changes in DA configurations near the boundaries, and could be an interesting starting point to explain why such similar ORAs still show large discrepancies in the South Atlantic meridional transports.

- **Twin-experiments for assimilating data near to the western boundary**

Another reason for the ORA transport discrepancies along the western boundary could be the lack of near boundary observations, which limits DA in constraining the ocean model in such dynamical regions. An idealised approach to test whether more near boundary observational data would better constrain the transports is to perform twin-experiments. In twin-experiments, fields from a model control run, such as SST, SSS, SSH and T/S profiles, are used to assimilate data into the same model, but in another run with different initial conditions. The purpose of twin-experiments is to assess how the assimilation run converges to the ″truth″, which in this case is the control run. For example, different amounts of model data from the control run could be assimilated near to the western boundary, in order to investigate how the transports of the assimilation run converge to the transports of the control run as more data are assimilated in the western boundary region.

- **Comparisons with eddy-resolving ORAs**

An interesting comparison for future work could be with eddy-resolving ORAs. For example, a version of GLORYS reanalysis at 1/12° horizontal resolution (GLORYS2V12) has already been released. Results of this thesis showed that the eddy-resolving FRM better captures the DWBC dynamics and variability in the tropical South Atlantic compared to eddy-permitting products, although its AMOC strength and MHT are quite low with respect to the ORAs and observational estimates. Therefore, the combination of DA with a high-resolution model could improve the ORA

representation of the western boundary transports. This could be evaluated by comparing GLORYS2V4 and GLORYS2V12.

- **Correcting DA issues in GloSea5**

GloSea5 transports start to drift in the South Atlantic when altimetry data assimilation is introduced into the DA system, more precisely in October 1992. We suspect this is related to inconsistencies in MDT bias corrections prior to SLA assimilation in GloSea5, particularly south of 20°N. We raised this suspicion because GloSea5 misrepresents by far the position and intensity of the mean flows in the South Atlantic. Investigations of the altimetry assimilation code, including its MDT bias correction, could be done for future work. GloSea5 experiments modifying the altimetry bias correction technique could also be performed to understand and therefore correct DA issues with this ORA.

- **Assessing CMIP5 historical runs and warming scenarios**

We have evaluated the internal variability of CMIP5 simulations with greenhouse gas emissions, radiative forcing and volcanic and anthropogenic aerosols held constant at pre-industrial levels. In order to shed more light on other feedbacks and mechanisms controlling the AMOC behavior, it would be interesting to know how the spatio-temporal variability of the freshwater budgets would behave in CMIP5 experiments, where the system is forced to change more systematically than the natural variability in the pre-industrial runs. We could use the historical runs and even warming scenarios to evaluate how this could impact the freshwater budget variability with respect to pre-industrial runs. More CMIP5 or even new CMIP6 models could also be added to the work in order to make the budget analyses more comprehensive and robust.

- **Atlantic freshwater budgets at subpolar latitudes**

In Chapter 5 the freshwater budgets were evaluated between 34°S and any other latitude up to 50°N. More work can be done with the freshwater budget variability in

CMIP5 models, focusing on a smaller but key area in the subpolar Atlantic (e.g. from 45°N to 65°N), where the OSNAP array is located (*Lozier et al.*, 2019). Understanding the contributions of each budget component to FWC changes in the subpolar Atlantic could be extremely important to better understand the AMOC variability, since FWC changes in this region can affect the deep water formation regions and therefore the North Atlantic MOC strength much more quickly than those in the southern Atlantic.

Freshwater budgets from FRMs and ORAs could also be calculated and compared to freshwater budgets from CMIP5 runs at subpolar latitudes. This would give more insights about the dominant physical processes and how they vary between the different products in this key region.

- **Simplified ocean model to study the Atlantic freshwater budgets**

In order to better understand the role of each freshwater budget component, a simplified ocean model could also be used to specify individual components (e.g. E-P+R, salinity distributions at 34°S, F_{ov} and F_{gyre}) and therefore study the sensitivity of the AMOC by allowing variation in one component at a time. A similar experimental approach published by *Zika et al.* (2018) to partition drivers of changing salinity could be employed for studying the freshwater budgets in a simplified model.

- **Investigating heat budgets**

A similar work can also be done for the heat budgets, which would complement the freshwater budget analyses. It would be useful to investigate which are the dominant components of the heat budget variability and how they vary throughout the Atlantic on a range of timescales. In Chapter 5 we have seen that the freshwater gyre component is the dominant advection term in explaining South Atlantic FWC changes, whereas the freshwater overturning component becomes the dominant advection term in contributing to North Atlantic FWC changes. Analysing the heat budget variability, we could also evaluate the role of heat gyre and overturning components in driving heat content changes throughout the basin.

- **Density difference between AAIW and NADW formation regions**

A different view of AMOC stability indicators is also given by *Saenko et al.* (2003). By applying freshwater perturbations only in the AAIW formation regions, they clearly showed that the transition between the ″on″ and ″off″ states occurs when the densities in the AAIW and NADW formation regions become comparable to each other. This seems an interesting approach to investigate AMOC bi-stability, although *Saenko et al.* (2003) have looked at only one coupled model. For future work, we could run freshwater hosing experiments in the AAIW formation region in different coupled models to investigate whether they show similar responses to the one used by *Saenko et al.* (2003). We could also look at the CMIP5 experiments and evaluate how the temporal evolution of density differences between AAIW and NADW influences the AMOC strength under different warming scenarios.

REFERENCES

Adcroft, A., and R. Hallberg (2006), On methods for solving the oceanic equations of motion in generalized vertical coordinates, *Ocean Modelling*, *11*, 224–233.

Adcroft, A., C. Hill, and J. Marshall (1997), Representation of topography by shaved cells in a height coordinate ocean model, *Monthly Weather Review*, *125*, 2293–2315.

Ansorge, I. J., M. O. Baringer, E. J. D. Campos, S. Dong, R. A. Fine, S. L. Garzoli, G. Goni, C. S. Meinen, R. C. Perez, A. R. Piola, M. J. Roberts, S. Speich, J. Sprintall, T. Terre, and M. A. Van den Berg (2014), Basin-Wide Oceanographic Array Bridges the South Atlantic, *Earth and Space Science News*, *95*, 53–54.

Backeberg, B. C., F. Counillon, J. A. Johannessen, and M.-I. Pujol (2014), Assimilating along-track SLA data using the EnOI in an eddy resolving model of the Agulhas system, Ocean, *Ocean Dynamics*, *64*, 1121–1136, doi:10.1007/s10236-014-0717-6.

Baehr, J., J. Hirschi, J.-O. Beismann, and J. Marotzke (2004), Monitoring the meridional overturning circulation in the North Atlantic: A model-based array design study, *Journal of Marine Research*, *62*, 283–312.

Balmaseda, M. A., K. Mogensen, and A. T. Weaver (2013a), Evaluation of the ECMWF

ocean reanalysis system ORAS4, *Quarterly Journal of the Royal Meteorological Society*, *139*, 1132–1161.

Balmaseda, M. A., K. E. Trenberth, and E. Kallene (2013b), Distinctive Climate Signals in Reanalysis of Global Ocean Heat Content, *Geophysical Research Letters*, *40*, 1754–1759, doi:10.1002/grl.50382.

Balmaseda, M. A., F. Hernandez, A. Storto, M. D. Palmer, O. Alves, L. Shi, G. C. Smith, T. Toyoda, M. Valdivieso, B. Barnier, D. Behringer, T. Boyer, Y.-S. Chang, G. A. Chepurin, N. Ferry, G. Forget, Y. Fujii, S. Good, S. Guinehut, K. Haines, Y. Ishikawa, S. Keeley, A. Kohl, T. Lee, M. J. Martin, S. Masina, S. Masuda, B. Meyssignac, K. Mogensen, L. Parent, K. A. Peterson, Y. M. Tang, Y. Yin, G. Vernieres, X. Wang, J. Waters, R. Wedd, O. Wang, Y. Xue, M. Chevallier, J.-F. Lemieux, F. Dupont, T. Kuragano, M. Kamachi, T. Awaji, A. Caltabiano, K. Wilmer-Becker, and F. Gaillard (2015), The Ocean Reanalyses Intercomparison Project (ORA-IP), *Journal of Operational Oceanography*, *8*, 80–97.

Barnier, B., G. Madec, T. Penduff, J. M. Molines, A. M. Treguier, J. Le Sommer, A. Beckmann, A. Biastoch, C. Boning, J. Dengg, J. Derval, E. Durand, S. Gulev, E. Remy, C. Talandier, S. Theetten, M. Maltrud, J. McClean, and B. de Cuevas (2006), Impact of partial steps and momentum advection schemes in a global ocean circulation model at eddy-permitting resolution, *Ocean Dynamics*, *56*, 543–567, doi:10.1007/s10236-006-0082.

Bellucci, A., S. Gualdi, S. Masina, S. Storto, E. Scoccimarro, C. Cagnazzo, P. Fogli, E. Manzini, and A. Navarra (2013), Decadal climate predictions with a coupled AOGCM initialized with oceanic reanalyses, *Climate Dynamics*, *40*, 1483–1497.

Biastoch, A., C. W. Böning, and J. R. E. Lutjeharms (2008a), Agulhas leakage dynamics affects decadal variability in Atlantic overturning circulation, *Nature*, *456*, 489–492, doi:10.1038/nature07426.

Biastoch, A., C. W. Böning, J. Getzlaff, J.-M. Molines, and G. Madec (2008b), Causes of interannual-decadal variability in the meridional overturning circulation of the midlatitude North Atlantic Ocean, *Journal of Climate*, *21*, 6599–6615, doi:10.1175/2008JCLI2404.1.

Bingham, R. J., and C. W. Hughes (2009), Geostrophic dynamics of meridional transport variability in the subpolar North Atlantic, *Journal of Geophysical Research*, *114*, doi:10.1029/2009JC005492.

Blanke, B., M. Arhan, and S. Speich (2006), Salinity changes along the upper limb of the Atlantic thermohaline circulation, *Geophysical Research Letters*, *33*, doi:10.1029/2005GL024938.

Blockley, E. W., M. J. Martin, A. J. McLaren, A. G. Ryan, J. Waters, D. J. Lea, I. Mirouze, K. A. Peterson, and A. Sellar (2014), Recent development of the Met Office operational ocean forecasting, *Geoscientific Model Development*, *7*, 2613–2638, doi:10.5194/gmd-7-2613-2014.

Böning, C. W., M. Scheinert, J. Dengg, A. Biastoch, and A. Funk (2006), Decadal variability of subpolar gyre transport and its reverberation in the North Atlantic overturning, *Geophysical Research Letters*, *33*, doi:10.1029/2006GL026906.

Broccoli, A. J., K. A. Dahl, and R. J. Stouffer (2006), Response of the ITCZ to Northern Hemisphere cooling, *Geophysical Research Letters*, *33*, doi:10.1029/2005GL024546.

Brodeau, L., B. Barnier, A.-M. Treguier, T. Penduff, and S. Gulev (2010), An ERA40-based atmospheric forcing for global ocean circulation models, *Ocean Modelling*, *31*, 88–104.

Broecker, W. S. (1998), Paleocean circulation during the last deglaciation: A bipolar seesaw?, *Paleoceanography*, *13*, 119–121.

Broecker, W. S. (2003), Does the trigger for abrupt climate change reside in the ocean or in the atmosphere?, *Science*, *300*, 1519–1522.

Bryden, H. L., and S. Imawaki (2001), *Ocean heat transport*, 455-474 pp., Academic Press, London.

Bryden, H. L., A. Mujahid, S. A. Cunningham, and T. Kanzow (2009), Adjustment of the basin-scale circulation at 26°N to variations in Gulf Stream, deep western boundary current and Ekman transports as observed by the RAPID array, *Ocean Science*, *5*, 421–433, doi:10.5194/os-5-421-2009.

Buckley, M. W., and J. Marshall (2016), Observations, inferences, and mechanisms of Atlantic Meridional Overturning Circulation variability: A review, *Reviews of Geophysics*, *54*, 5–63, doi:110.1002/2015RG000493.

Buckley, M. W., D. Ferreira, J.-M. Campin, J. Marshall, and R. Tulloch (2012), On the relationship between decadal buoyancy anomalies and variability of the Atlantic Meridional Overturning Circulation, *Journal of Climate*, *25*, 8009–8030, doi:10.1175/JCLI-D-11-00505.1.

Buckley, M. W., R. M. Ponte, G. Forget, and P. Heimbach (2014), Low-frequency SST and upper-ocean heat content variability in the North Atlantic, *Journal of Climate*, *27*, 4996–5018, doi:10.1175/JCLI-D-13-00316.1.

Cabanes, C., T. Lee, and L.-L. Fu (2008), Mechanisms of interannual variations of the Meridional Overturning Circulation of the North Atlantic Ocean, *Journal of Physical Oceanography*, *38*, 467–480, doi:10.1175/2007JPO3726.1.

Castellanos, P., E. J. D. Campos, J. Piera, O. T. Sato, and M. A. F. Silva-Dias (2017), Impacts of Agulhas Leakage on the Tropical Atlantic Western Boundary Systems, *Journal of Climate*, *30*, 6645–6659.

Chen, X., and K. K. Tung (2014), Varying Planetary Heat Sink Led to Global-Warming Slowdown and Acceleration, *Science*, *345*, 897–903.

Cheng, W., W. Weijer, W. M. Kim, G. Danabasoglu, S. G. Yeager, P. R. Gent, D. Zhang, J. C. H. Chiang, and J. Zhang (2018), Can the Salt-Advection Feedback Be Detected in Internal Variability of the Atlantic Meridional Overturning Circulation?, *Journal of Climate*, *31*, 6649–6667, doi:10.1175/JCLI-D-17-0825.1.

Clarke, A., J. Church, and J. Gould (2001), *Ocean Processes and Climate Phenomena*, 11-30 pp., Academic Press, London.

Cunningham, S. A., T. Kanzow, D. Rayner, M. O. Baringer, W. E. Johns, J. Marotzke, H. R. Longworth, E. M. Grant, J. J.-M. Hirschi, L. M. Beal, C. S. Meinen, and H. L. Bryden (2007), Temporal Variability of the Atlantic Meridional Overturning Circulation at 26.5°N, *Science*, *317*, 935–937.

Danabasoglu, G. (2008), On multidecadal variability of the Atlantic Meridional Overturning Circulation in the Community Climate System Model version 3, *Journal of Climate*, *21*, 5524–5544, doi:10.1175/2008JCLI2019.1.

Danabasoglu, G., S. Yeager, Y.-O. Kwon, J. Tribbia, A. Phillips, and J. Hurrell (2012), Variability of the Atlantic Meridional Overturning Circulation in CCSM4, *Journal of Climate*, *25*, 5153–5172, doi:10.1175/JCLI-D-11-00463.1.

de Boer, A. M., A. Gnanadesikan, N. R. Edwards, and A. J. Watson (2010), Meridional density gradients do not control the Atlantic overturning circulation, *Journal of Physical Oceanography*, *40*, 368–380.

De Vries, P., and S. L. Weber (2005), The Atlantic freshwater budget as a diagnostic for the existence of a stable shut down of the meridional overturning circulation, *Geophysical Research Letters*, *32*, doi:10.1029/2004GL021450.

Delworth, T. L., R. Zhang, and M. Mann (2007), *Decadal to centennial variability of the Atlantic from observations and models*, 131-148 pp., AGU, Washington D. C.

Dengler, M., F. A. Schott, C. Eden, P. Brandt, J. Fischer, and R. J. Zantopp (2004), Break-up of the Atlantic deep western boundary current into eddies at 8°S, *Nature*, *432*, 1018–1020, doi:10.1002/2013JC009228.

Deshayes, J., R. Curry, and R. Msadek (2014), CMIP5 Model Intercomparison of Freshwater Budget and Circulation in the North Atlantic, *Journal of Climate*, *27*, 3298–3317.

Dong, S., S. Garzoli, M. Baringer, C. Meinen, and G. Goni (2009), Interannual variations in the Atlantic meridional overturning circulation and its relationship with the net northward heat transport in the South Atlantic, *Geophysical Research Letters*, *36*, doi:10.1029/2009GL039356.

Dong, S., M. Baringer, G. Goni, C. Meinen, and S. Garzoli (2011a), Importance of the assimilation of Argo float measurements on the Meridional Overturning Circulation in the South Atlantic, *Geophysical Research Letters*, *38*, doi:10.1029/2011GL048982.

Dong, S., S. Garzoli, and M. Baringer (2011b), The Role of Interocean Exchanges on Decadal Variations of the Meridional Heat Transport in the South Atlantic, *Journal of Physical Oceanography*, *41*, 1498–1511.

Dong, S., M. Baringer, G. Goni, C. Meinen, and S. Garzoli (2014), Seasonal variations in the South Alantic Meridional Overturning Circulation from observations and numerical models, *Geophysical Research Letters*, *41*, 4611–4618, doi:10.1002/2014GL060428.

Dong, S., G. Goni, and F. Bringas (2015), Temporal variability of the South Atlantic Meridional Overturning Circulation between 20°S and 35°S, *Geophysical Research Letters*, *42*, 7655–7662, doi:10.1002/2015GL065603.

Donners, J., S. S. Drijfhout, and W. Hazeleger (2005), Water Mass Transformation and Subduction in the South Atlantic, *Journal of Physical Oceanography*, *35*, 1841–1860.

Drijfhout, S. S., S. L. Weber, and E. van der Swaluw (2011), The stability of the MOC as diagnosed from model projections for pre-industrial, present and future climates, *Climate Dynamics*, *37*, 1575–1586, doi:10.1007/s00382-010-0930-z.

Drijfhout, S. S., T. Blakera, S. A. Josey, A. J. G. Nurser, B. Sinha, and M. A. Balmaseda (2014), Warming Hiatus Caused by Increased Heat Uptake across Multiple Ocean Basins, *Geophysical Research Letters*, *41*, 7868–7874.

Dufresne, J., M. Foujols, S. Denvil, A. Caubel, O. Marti, O. Aumont, Y. Balkanski, S. Bekki, H. Bellenger, R. Benshila, S. Bony, L. Bopp, P. Braconnot, P. Brockmann, and P. Cadule (2013), Climate change projections using the IPSL-CM5 Earth System Model: from CMIP3 to CMIP5, *Climate Dynamics*, *40*, 2123–2165.

Dunne, J. P., J. John, E. Shevliakova, R. J. Stouffer, J. P. Krasting, S. L. Malyshev, P. C. Milly, L. T. Sentman, A. J. Adcroft, and S. M. Griffies (2012), GFDL ESM2 Global Coupled ClimateCarbon Earth System Models. Part II: Carbon System Formulation and Baseline Simulation Characteristics, *Journal of Climate*, *25*, 6646–6665.

Ekman, V. W. (1905), On the influence of the earth's rotation on ocean currents, *Arch. Math. Astron. Phys.*, *2*, 1–52.

England, M. H., S. McGregor, P. Spence, G. A. Meehl, A. Timmermann, W. Cai, A. Sen Gupta, M. J. McPhaden, A. Purich, and A. Santoso (2014), Recent Intensification of Wind-Driven Circulation in the Pacific and the Ongoing Warming Hiatus, *Nature Climate Change*, *4*, 222–227.

Ferreira, D., P. Cessi, H. K. Coxall, A. de Boer, H. A. Dijkstra, S. S. Drijfhout, T. Eldevik, N. Harnik, J. McManus, D. P. Marshall, J. Nilsson, F. Roquet, T. Schneider, and

R. C. Wills (2018), Atlantic-Pacific Asymmetry in Deep Water Formation, *Annual Review of Earth and Planetary Sciences*, *46*, 327–352.

Feulner, G., S. Rahmstorf, A. Levermann, and S. Volkwardt (2013), On the origin of the surface air temperature difference between the hemispheres in Earths present-day climate, *Journal of Climate*, *26*, 7136–7150, doi:10.1175/JCLI-D-12-00636.1.

Fratantoni, D. M., W. E. Johns, and T. L. Townsend (1995), Rings of the North Brazil Current: Their structure and behavior inferred from observations and a numerical simulation, *Journal of Geophysical Research*, *100*, 633–654.

Frierson, D. M. W., Y.-T. Hwang, N. S. Fuckar, R. Seager, S. M. Kang, A. Donohoe, E. A. Maroon, X. Liu, and S. Battisti (2013), Contribution of ocean overturning circulation to tropical rainfall peak in the Northern Hemisphere, *Nature Geosciences*, *6*, 940–944, doi:10.1038/ngeo1987.

Ganachaud, A., and C. Wunsch (2003), Large scale ocean heat and freshwater transports during the World Ocean Circulation Experiment, *Journal of Climate*, *16*, 695–705.

Garzoli, S. L. (1993), Geostrophic velocity and transport variability in the Brazil-Malvinas confluence, *Deep-Sea Research Part I*, *40*, 1379–1403.

Garzoli, S. L., and M. O. Baringer (2007), Meridional heat transport determined with expandable bathythermographs - Part II, *Deep-Sea Research Part I*, *54*, 1402–1420.

Garzoli, S. L., and R. Matano (2011), The South Atlantic and the Atlantic Meridional Overturning Circulation, *Deep-Sea Research Part II*, *58*, 1837–1847.

Garzoli, S. L., M. O. Baringer, S. Dong, R. Perez, and Q. Yao (2013), South Atlantic Meridional Fluxes, *Deep-Sea Research Part I*, *71*, 21–32.

Garzoli, S. L., S. Dong, R. Fine, C. Meinen, R. C. Perez, C. Schmid, E. Sebille, and

Q. Yao (2015), The fate of the Deep Western Boundary Current in the South Atlantic, *Deep-Sea Research Part I*, *103*, 125–136, doi:10.1016/j.dsr.2015.05.008.

Gent, P. R. (2018), A commentary on the Atlantic meridional overturning circulation stability in climate models, *Ocean Modelling*, *122*, 57–66.

Gent, P. R., and J. C. McWilliams (1990), Isopycnal mixing in ocean circulation models, *Journal of Physical Oceanography*, *20*, 150–155.

Gill, A. E. (1982), *How the Ocean-Atmosphere System is Driven*, 1-15 pp., Academic Press, London.

Gnanadesikan, A. (1999), A simple predictive model of the structure of the oceanic pycnocline, *Science*, *283*, 2077–2081.

Goes, M., M. Baringer, and G. Goni (2015a), The impact of historical biases on the XBT-derived meridional overturning circulation estimates at 34°S, *Geophysical Research Letters*, *42*, 1848–1855, doi:10.1002/2014GL061802.

Goes, M., G. Goni, and S. Dong (2015b), An optimal XBT-based monitoring system for the South Atlantic meridional overturning circulation at 34°S, *Journal of Geophysical Research: Oceans*, *120*, 161–181, doi:10.1002/2014JC010202.

Goni, G., S. Kamholz, S. Garzoli, and D. Olson (1996), Dynamics of the Brazil-Malvinas Confluence based on inverted echo sounders and altimetry, *Journal of Geophysical Research*, *101*, 273–289.

Good, S. A., M. J. Martin, and N. A. Rayner (2013), EN4: quality controlled ocean temperature and salinity profiles and monthly objective analyses with uncertainty estimates, *Journal of Geophysical Research*, *118*, 6704–6716, doi:10.1002/2013JC009067.

Gordon, H. B., S. P. Farrell, M. A. Collier, M. R. Dix, L. D. Rotstayn, E. A. Kowalczyk, A. C. Hirst, and I. G. Watterson (2010), The csiro mk3.5 climate model, cawcr technical report, *Tech. rep.*, CSIRO-QCCE.

Griesel, A., and M. A. M. Maqueda (2006), The relation of meridional pressure gradients to North Atlantic deep water volume transport in an ocean general circulation model, *Climate Dynamics*, *26*, 781–799, doi:10.1007/s00382-006-0122-z.

Griffies, S. M. (2009), Elements of mom4p1, gfdl ocean group technical report, *Tech. rep.*, Geophysical Fluid Dynamics Laboratory.

Haines, K., M. Valdivieso, H. Zuo, and V. N. Stepanov (2012), Transports and budgets in a 1/4° global ocean reanalysis 1989-2010, *Ocean Science*, *8*, 333–344, doi:10.5194/os-8-333-2012.

Hawkins, E., R. S. Smith, L. C. Allison, J. M. Gregory, T. J. Woolings, H. Pohlmann, and B. de Cuevas (2011), Bistability of the Atlantic overturning circulation in a global climate model and links to ocean freshwater transport, *Geophysical Research Letters*, *38*, doi:10.1029/2011GL047208.

Hirschi, J., J. Baehr, J. Marotzke, J. Stark, S. Cunningham, and J.-O. Beismann (2003), A monitoring design for the Atlantic meridional overturning circulation, *Geophysical Research Letters*, *30*, doi:10.1029/2002GL016776.

Hirschi, J., P. Killworth, and J. Blundel (2007), Subannual, seasonal, and interannual variability of the North Atlantic Meridional Overturning Circulation, *Journal of Physical Oceanography*, *37*, 1246–1265.

Holliday, N. P. (2003), Air-sea interaction and circulation changes in the northeast Atlantic, *Journal of Geophysical Research*, *108*, doi:10.1029/2002JC001344.

Huisman, S. E., M. den Toom, H. A. Dijkstra, and S. S. Drijfhout (2010), An indicator of the multiple equilibria regime of the Atlantic meridional overturning circulation, *Journal of Physical Oceanography*, *40*, 551–567, doi:10.1175/2009JPO4215.1.

Hummels, R., P. Brandt, M. Dengler, J. Fischer, M. Araujo, D. Veleda, and J. V.

Durgadoo (2015), Interannual to decadal changes in the western boundary circulation in the Atlantic at 11°S, *Geophysical Research Letters*, *42*, doi:10.1002/2015GL065254.

Hunke, E. C., and W. H. Lipscomb (2010), CICE: the Los Alamos sea ice model. Documentation and software users manual, Version 4.1, *Tech. rep.*, Los Alamos National Laboratory, Los Alamos.

Jackson, L. C. (2013), Shutdown and recovery of the AMOC in a coupled global climate model: the role of the advective feedback, *Geophysical Research Letters*, *40*, 1182–1188.

Jackson, L. C., R. Kahana, T. Graham, M. A. Ringer, T. Woollings, J. V. Mecking, and R. A. Wood (2015), Global and European climate impacts of a slowdown of the AMOC in a high resolution GCM, *Climate Dynamics*, *45*, 3299–3316, doi:10.1007/s00382-015-2540-2.

Jackson, L. C., K. A. Peterson, C. D. Roberts, and R. A. Wood (2016), Recent slowing of Atlantic overturning circulation as a recovery from earlier strengthening, *Nature Geoscience*, *9*, 518–522, doi:10.1038/NGEO2715.

Jackson, L. C., C. Dubois, G. Forget, K. Haines, M. Harrison, D. Iovino, A. Kohl, D. Mignac, S. Masina, K. A. Peterson, C. G. Piecuch, C. Roberts, J. Robson, A. Storto, T. Toyoda, M. Valdivieso, C. Wilson, Y. Wang, and H. Zuo (2019), North Atlantic circulation: a perspective from ocean reanalyses, *Submitted to Journal of Geophysical Research: Oceans*.

Janssen, P., O. Breivik, K. Mogensen, F. Vitart, M. Balmaseda, J.-R. Bidlot, S. Keeley, M. Leutbecher, L. Magnusson, and F. Molteni (2013), Air-sea interaction and surface waves, ECMWF Technical Report 712, *Tech. rep.*, ECMWF.

Ji, D., L. Wang, J. Feng, Q. Wu, H. Cheng, Q. Zhang, J. Yang, W. Dong, Y. Dai, D. Gong, R. Zhang, X. Wang, J. Liu, J. Moore, D. Chen, and M. Zhou (2014),

Description and basic evaluation of Beijing Normal University Earth System Model (BNU-ESM) version 1, *Geoscience Model Development*, *7*, 2039–2064.

Jia, Y. (2000), Formation of an Azores Current due to the Mediterranean overflow in a modeling study of the North Atlantic, *Journal of Physical Oceanography*, *30*, 2342–2358.

Jia, Y., A. C. Coward, B. A. De Cuevas, and D. J. Webb (2007), A model analysis of the behavior of the Mediterranean Water in the North Atlantic, *Journal of Physical Oceanography*, *37*, 764–786.

Jochumsen, K., M. Rhein, S. Hüttl-Kabus, and C. W. Böning (2010), On the propagation and decay of North Brazil Current rings, *Journal of Geophysical Research*, *115*, 103–120, doi:10.1029/2009JC006042.

Johns, W. E., T. N. Lee, F. A. Schott, R. J. Zantopp, and R. H. Evans (1990), The North Brazil Current Retroflection: Seasonal Structure and Eddy Variability, *Journal of Geophysical Research*, *95*, 103–120.

Johnson, H. L., and D. P. Marshall (2002), Localization of abrupt change in the North Atlantic thermohaline circulation, *Geophysical Research Letters*, *29*, 1083–1086, doi:10.1029/2001GL014140.

Joyce, T. M., and R. Zhang (2015), On the path of the Gulf Stream and the Atlantic Meridional Overturning Circulation, *Journal of Climate*, *23*, 3146–3154, doi:10.1175/2010JCLI3310.1.

Kang, S. M., R. Seager, D. M. W. Frierson, and X. Liu (2014), Croll revisited: Why is the northern hemisphere warmer than the southern hemisphere?, *Climate Dynamics*, *44*, 1457–1472, doi:10.1007/s00382-014-2147-z.

Karspeck, A. R., D. Stammer, A. Kohl, G. Danabasoglu, M. Balmaseda, D. M. Smith, Y. Fujii, S. Zhang, B. Giese, H. Tsujino, and A. Rosati (2015), Comparison of the

Atlantic meridional overturning circulation between 1960 and 2007 in six ocean reanalysis products, *Climate Dynamics*, *49*, 957–982, doi:10.1007/s00382-015-2787-7.

Kiehl, J. T., and K. E. Trenberth (1997), Earth's Annual Global Mean Energy Budget, *Bulletin of the American Meteorological Society*, *78*, 197–208.

Knight, J. R., R. J. Allan, C. K. Folland, M. Vellinga, and M. E. Mann (2005), A signature of persistent natural thermohaline circulation cycles in observed climate, *Journal of Geophysical Research Letters*, *32*, 5846–5862, doi:10.1029/2005GL024233.

Kostov, Y., K. C. Armour, and J. Marhsall (2014), Impact of the Atlantic meridional overturning circulation on ocean heat storage and transient climate change, *Geophysical Research Letters*, *41*, 2108–2116, doi:10.1002/2013GL05899.

Kuhlbrodt, T., A. Griesel, M. Montoya, A. Levermann, M. Hofmann, and S. Rahmstorf (2007), On the driving processes of the Atlantic meridional overturning circulation, *Reviews of Geophysics*, *45*, doi:10.1029/2004RG000166.

Large, W. G., and S. G. Yeager (2004), Diurnal to decadal global forcing for ocean and sea-ice models: The data sets and flux climatologies, technical report tn-460+str, *Tech. rep.*, NCAR.

Large, W. G., and S. G. Yeager (2009), The global climatology of an interannually varying air-sea flux data set, *Climate Dynamics*, *33*, 341–364, doi:10.1007/s00382-008-0441-3.

Latif, M., E. Roeckner, M. Botzet, M. Esch, H. Haak, S. Hagemann, J. Jungclaus, S. Legutke, S. Marsland, U. Mikolajewicz, and J. Mitchell (2003), Reconstructing, Monitoring, and Predicting Multidecadal-Scale Changes in the North Atlantic Thermohaline Circulation with Sea Surface Temperature, *Journal of Climate*, *17*, 1605–1614.

Laurian, A., S. S. Drijfhout, W. Hazeleger, and B. Hurk (2009), Response of the Western European climate to a collapse of the thermohaline circulation, *Climate Dynamics*, *34*, 689–697.

Lee, S.-K., R. Lumpkin, M. O. Baringer, C. S. Meinen, M. Goes, S. Dong, H. Lopez, and S. G. Yeager (2019), Global meridional overturning circulation inferred from a data-constrained ocean and sea-ice model, *Geophysical Research Letters*, *46*, 1521–1530, doi:10.1029/2018GL080940.

Legg, S., B. Briegleb, Y. Chang, E. P. Chassignet, G. Danabasoglu, T. Ezer, A. L. Gordon, S. Griffies, R. Hallberg, L. Jackson, W. Large, T. M. zgkmen, H. Peters, J. Price, U. Riemenschneider, W. Wu, X. Xu, and J. Yang (2009), Improving Oceanic overflow representation in climate models: The Gravity Current Entrainment Climate Process Team, *Bulletin of the American Meteorological Society*, *31*, 657–670.

Lellouche, J.-M., O. Le Galloudec, M. Drevillon, C. Regnier, E. Greiner, G. Garric, N. Ferry, C. Desportes, C.-E. Testut, C. Bricaud, R. Bourdalle-Badie, B. Tranchant, M. Benkiran, Y. Drillet, A. Daudin, and C. De Nicola (2013), Evaluation of global monitoring and forecasting systems at Mercator Ocean, *Ocean Science*, *9*, 57–81.

Levitus, S., T. P. Boyer, M. E. Conkright, T. OBrien, J. Antonov, C. Stephens, L. Stathoplos, D. Johnson, and R. Gelfeld (1998), *NOAA Atlas NESDIS 18, World Ocean Database 1998*, U.S Gov. Printing Office, Washington D.C.

Lin, S. J. (2004), A "vertically Lagrangian" finite-volume dynamical core for global models, *Monthly Weather Review*, *132*, 2293–2307.

Liu, C., R. P. Allan, P. Berrisford, M. Mayer, P. Hyder, N. Loeb, D. Smith, and J. M. Edwards (2015), Combining satellite observations and reanalysis energy transports to estimate global net surface energy fluxes 1985-2012, *Journal of Geophysical Research: Atmospheres*, *120*, 9374–9389, doi:10.1002/2015JDO23264.

Liu, W., and Z. Liu (2013), A diagnostic indicator of the stability of the Atlantic meridional overturning circulation in CCSM3, *Journal of Climate*, *26*, 1926–1938, doi:10.1175/JCLI-D-11-00681.1.

Liu, W., S.-P. Xie, Z. Liu, and J. Zhu (2017), Overlooked possibility of a collapsed Atlantic Meridional Overturning Circulation in warming climate, *Science Advances*, *3*, doi:10.1126/sciadv.1601666.

Locarnini, R. A., A. Mishonov, J. Antonov, T. Boyer, H. Garcia, O. Baranova, M. Zweng, and D. Johnson (2010), *World Ocean Atlas 2009, volume 1: Temperature*, U.S Gov. Printing Office, Washington D.C.

Locarnini, R. A., A. V. Mishonov, J. I. Antonov, T. P. Boyer, H. E. Garcia, O. K. Baranova, M. M. Zweng, C. R. Paver, J. R. Reagan, D. R. Johnson, M. Hamilton, and D. Seidov (2013), *World Ocean Atlas 2013, volume 1: Temperature*, U.S Gov. Printing Office, Washington D.C.

Lopez, H., S. Dong, S. Lee, and G. Goni (2016), Decadal Modulations of Interhemispheric Global Atmospheric Circulations and Monsoons by the South Atlantic Meridional Overturning Circulation, *Journal of Climate*, *29*, 1831–1851.

Lozier, M. S. (2010), Deconstructing the Conveyor Belt, *Science*, *328*, 1507–1511.

Lozier, M. S., F. Li, S. Bacon, F. Bahr, A. S. Bower, S. A. Cunningham, M. F. de Jong, L. de Steur, B. deYoung, J. Fischer, F. Gary, B. J. W. Greenan, N. P. Holliday, A. Houk, L. Houpert, M. E. Inall, W. E. Johns, H. L. Johnson, C. Johnson, J. Karstensen, G. Koman, I. A. Le Bras, X. Lin, N. Mackay, D. P. Marshall, H. Mercier, M. Oltmanns, R. S. Pickart, A. L. Ramsey, D. Rayner, F. Straneo, V. Thierry, D. J. Torres, R. G. Williams, C. Wilson, J. Yang, I. Yashayaev, and J. Zhao (2019), A sea change in our view of overturning in the subpolar North Atlantic, *Science*, *363*, 516–521.

Macdonald, A. M., and M. O. Baringer (2013), *Ocean heat transport*, 759-786 pp., Academic Press, London.

Madec, G. (2008), NEMO ocean engine, Note du Pole de modlisation, *Tech. rep.*, Institut Pierre-Simon Laplace (IPSL), France.

Madec, G., and M. Imbard (1996), A global ocean mesh to overcome the North Pole singularity, *Climate Dynamics*, *12*, 381–388.

Majumder, S., C. Schmid, and G. Halliwell (2016), An observations and model-based analysis of meridional transports in the South Atlantic, *Journal of Geophysical Research: Oceans*, *121*, 5622–5638, doi:10.1002/2016JC011693.

Manabe, S., and R. J. Stouffer (1993), Century-scale effects of increased atmospheric CO2 on the ocean-atmosphere system, *Nature*, *364*, 215–218.

Marotzke, J., R. Giering, K. Q. Zhang, D. Stammer, C. Hill, and T. Lee (1999), Construction of the adjoint MIT ocean general circulation model and application to Atlantic heat transport sensitivity, *Journal of Geophysical Research*, *104*, 529–547.

Marshall, J., and F. Schott (1999), Openocean convection: Observations, theory, and models, *Reviews of Geophysics*, *37*, 1–64.

Marshall, J., and K. Speer (2012), Closure of the meridional overturning circulation through Southern Ocean upwelling, *Nature Geosciences*, *5*, 171–180, doi:10.1038/ngeo1391.

Marshall, J., A. Donohoe, D. Ferreira, and D. McGee (2013), The ocean′s role in setting the mean position of the Inter-Tropical Convergence Zone, *Climate Dynamics*, *42*, 1967–1979.

Marzocchi, A., J. J.-M. Hirschi, N. P. Holliday, S. A. Cunningham, A. T. Blaker, and A. C. Coward (2015), The North Atlantic subpolar circulation in an eddy-resolving global ocean model, *Journal of Marine Systems*, *142*, 126–143.

Masina, S., A. Storto, N. Ferry, M. Valdivieso, K. Haines, M. Balmaseda, H. Zuo, M. Drevillon, and L. Parent (2015), An ensemble of eddy-permitting global ocean reanalyses from the MyOcean project, *Climate Dynamics*, *49*, 813–841, doi:10.1007/s00382-015-2728-5.

McDonagh, E. L., P. McLeod, B. A. King, H. L. Bryden, and S. T. Valdés (2010), Circulation, heat, and freshwater transport at 36°N in the Atlantic, *Journal of Physical Oceanography*, *40*, 2661–2678, doi:10.1175/2010JPO4176.1.

McDonagh, E. L., B. A. King, H. L. Bryden, P. Courtois, Z. Szuts, M. Baringer, S. A. Cunningham, C. Atkinson, and G. McCarthy (2015), Continuous estimate of Atlantic oceanic freshwater flux at 26.5°N, *Journal of Climate*, *28*, 8888–8906, doi:10.1175/JCLI-D-14-00519.1.

Mecking, J. V., S. S. Drijfhout, L. C. Jackson, and T. Graham (2016), Stable AMOC off state in an eddy-permitting coupled climate model, *Climate Dynamics*, *47*, 2455–2470.

Mecking, J. V., S. S. Drijfhout, L. C. Jackson, and M. B. Andrews (2017), The effect of model bias on Atlantic freshwater transport and implications for AMOC bi-stability, *Tellus A*, *69*, 1–14.

Meinen, C. S., R. C. Speich, R. C. Perez, S. Dong, A. R. Piola, S. L. Garzoli, M. O. Baringer, S. Gladyshev, and E. J. D. Campos (2013), Temporal variability of the Meridional Overturning Circulation at 34.5°S: Results from two pilot boundary arrays in the South Atlantic, *Journal of Geophysical Research: Oceans*, *118*, 6461–6478, doi:10.1002/2013JC009228.

Mémery, L., M. Arhan, X. A. Alvarez-Salgado, M.-J. Messias, H. Mercier, C. G. Castro, and A. F. Rios (2000), The water masses along the western boundary of the south and equatorial Atlantic, *Progress in Oceanography*, *47*, 69–98.

Mignac, D., D. Ferreira, and K. Haines (2018), South Atlantic meridional transports from NEMO-based simulations and reanalyses, *Ocean Science*, *14*, 53–68, doi:10 .5194/os-14-53-2018.

Mignac, D., D. Ferreira, and K. Haines (2019), Decoupled freshwater transport and meridional overturning in the South Atlantic, *Geophysical Research Letters*, *46*, 2178–2186, doi:10.1029/2018GL081328.

Mogensen, K., M. A. Balmaseda, and A. Weaver (2012), The NEMOVAR ocean data assimilation system as implemented in the ECMWF ocean analysis for system 4, Technical Report 668, *Tech. rep.*, ECMWF.

Molinari, R. L. (1982), Observations of Eastward Currents in the Tropical South Atlantic Ocean: 1978-1980, *Journal of Geophysical Research*, *87*, 9707–9714.

Msadek, R., and C. Frankignoul (2009), Atlantic multidecadal oceanic variability and its influence on the atmosphere in a climate model, *Climate Dynamics*, *33*, 45–62, doi:10.1007/s00382-008-0452-0.

Neale, R. B. (2003), Description of the ncar community atmosphere model (cam 5.0), ncar tech. note tn-486, *Tech. rep.*, National Center for Atmospheric Research.

Palmer, M. D., C. D. Roberts, M. Balmaseda, Y.-S. Chang, G. Chepurin, N. Ferry, Y. Fujii, S. A. Good, S. Guinehut, K. Haines, F. Hernandez, A. Khl, T. Lee, M. J. Martin, S. Masina, S. Masuda, K. A. Peterson, A. Storto, T. Toyoda, M. Valdivieso, G. Vernieres, O. Wang, and Y. Xue (2015), Ocean heat content variability and change in an ensemble of ocean reanalyses, *Climate Dynamics*, *47*, 909–930, doi:10.1007/s00382-015-2801-0.

Pedro, J. B., T. D. van Ommen, S. O. Rasmussen, V. I. Morgan, J. Chappellaz, A. D. Moy, V. Masson-Delmotte, and M. Delmotte (2011), The last deglaciation: Timing the bipolar seesaw, *Climate of the Past*, *7*, 671–683.

Penduff, T., M. Juza, L. Brodeau, G. C. Smith, B. Barnier, J.-M. Molines, A.-M. Treguier, and G. Madec (2010), Impact of global ocean model resolution on sea-level variability with emphasis on interannual time scales, *Ocean Science*, *6*, 269–284, doi:10.5194/os-6-269-2010.

Perez, R. C., S. L. Garzoli, C. S. Meinen, and R. P. Matano (2011), Geostrophic Velocity Measurement Techniques for the Meridional Overturning Circulation and Meridional Heat Transport in the South Atlantic, *Journal of Atmospheric and Ocean Technology*, *28*, 1504–1520.

Peterson, R. G., and L. Stramma (1991), Upper-level circulation in the South Atlantic Ocean, *Progress in Oceanography*, *26*, 1–73.

Pham, D. T., J. Verron, and M. C. Roubaud (1998), A singular evolutive extended Kalman filter for data assimilation in oceanography, *Journal of Marine Systems*, *16*, 323–340.

Pohlmann, H., J. H. Jungclaus, A. Köhl, D. Stammer, and J. Marotzke (2009), Initializing decadal climate predictions with the GECCO oceanic synthesis: effects on the North Atlantic, *Journal of Climate*, *22*, 3926–3938.

Qiao, F., Z. Song, Y. Bao, Y. Song, Q. Shu, C. Huang, and W. Zhao (2013), Development and evaluation of an Earth System Model with surface gravity waves, *Journal of Geophysical Research: Oceans*, *118*, 4514–4524.

Rabe, B., F. A. Schott, and A. Khl (2008), Mean circulation and variability of the tropical Atlantic during 1952-2001 in the GECCO assimilation fields, *Journal of Physical Oceanography*, *38*, 177–192.

Rahmstorf, S. (1996), On the freshwater forcing and transport of the Atlantic thermohaline circulation, *Climate Dynamics*, *12*, 799–811.

Rahmstorf, S., M. Crucifix, A. Ganapolski, H. Goosse, I. Kamenkovich, R. Knutti, G. Lohmann, R. Marsh, A. Lawrence, M. Z. Wang, and A. J. Weaver (2005), Thermohaline circulation hysteresis: a model intercomparison, *Geophysical Research Letters*, *32*, doi:10.1029/2005GL023655.

Rayner, D., J. M. Hirschi, T. Kanzow, W. E. Johns, P. G. Wright, E. Frajka-Williams, H. L. Bryden, C. S. Meinen, M. O. Baringer, J. Marotzke, L. M. Beal, and S. A. Cunningham (2011), Monitoring the Atlantic meridional overturning circulation, *Deep-Sea Research Part II*, *58*, 1744–1753.

Remaud, M., F. Chevallier, A. Cozic, X. Lin, and P. Bousquet (2018), On the impact of recent developments of the LMDz atmospheric general circulation model on the simulation of CO2 transport, *Geoscience Model Development*, *11*, 4489–4513.

Roberts, C. D., J. Waters, K. A. Peterson, M. D. Palmer, G. D. McCarthy, E. Frajka-Williams, K. Haines, D. J. Lea, M. J. Martin, D. Storkey, E. W. Blockley, and H. Zuo (2013), Atmosphere drives recent interannual variability of the Atlantic meridional overturning circulation at 26.5°N, *Geophysical Research Letters*, *40*, 5164–5170, doi:10.1002/grl.50930.

Robson, J., R. Sutton, K. Lohmann, D. Smith, and M. D. Palmer (2012), Causes of the rapid warming of the North Atlantic Ocean in the mid-1990s, *Journal of Climate*, *25*, 4116–4134, doi:10.1175/JCLI-D-11-00443.1.

Rodrigues, R. R., L. W. Rothstein, and M. Wimbush (2006), South Equatorial Current Bifurcation in the Atlantic Ocean: A Numerical Study, *Journal of Physical Oceanography*, *37*, 16–30.

Roeckner, E. (2003), The atmospheric general circulation model echam5. part i: Model description, mpi report 349, *Tech. rep.*, Max Planck Institute for Meteorology.

Rühs, S., K. Getzlaff, J. V. Durgadoo, A. Biastoch, and C. W. Böning (2015), On the suitability of North Brazil Current transport estimates for monitoring basin-

scale AMOC changes, *Geophysical Research Letters*, *42*, 8072–8080, doi:10.1002/2015GL065695.

Saenko, O. A., A. J. Weaver, and J. M. Gregory (2003), On the link between the two modes of the ocean thermohaline circulation and the formation of global-scale water masses, *Journal of Climate*, *16*, 2797–2801.

Sallée, J. B., E. Shuckburgh, N. Bruneau, A. Meijers, Z. Wang, and T. Bracegirdle (2013), Assessment of Southern Ocean water mass circulation in CMIP5 models: historical bias and forcing response, *Journal of Geophysical Research*, *118*, 1830–1844.

Schott, F. A., M. Dengler, R. Zantopp, L. Stramma, J. Fischer, and P. Brandt (2005), The shallow and deep western boundary circulation of the South Atlantic at 5°S-11°S, *Journal of Physical Oceanography*, *35*, 2031–2053.

Scoccimarro, E., S. Gualdi, A. Bellucci, A. Sanna, P. Fogli, E. Manzini, M. Vichi, P. Oddo, and A. Navarra (2011), Effects of tropical cyclones on ocean heat transport in a high resolution coupled general circulation model, *Journal of Climate*, *24*, 4368–4384.

Sebille, E. V., L. M. Beal, and W. E. Johns (2011), Advective Time Scales of Agulhas Leakage to the North Atlantic in Surface Drifter Observations and the 3D OFES Model, *Journal of Physical Oceanography*, *41*, 1026–1034.

Sijp, W. P. (2012), Characterising meridional overturning bistability using a minimal set of state variables, *Climate Dynamics*, *39*, 2127–2142, doi:10.1007/s00382-011-1249-0.

Silveira, I. C. A., L. B. Miranda, and W. S. Brown (1994), On the origins of the North Brazil Current, *Journal of Geophysical Research*, *99*, 501–512.

Simmons, A., S. Uppala, D. Dee, and S. Kobayashi (2007), ERA-Interim: New ECMWF reanalysis products from 1989 onwards, *ECMWF Newsletter*, *110*, 25–35.

Sitz, L. E., R. Farneti, and S. M. Griffies (2015), Simulated South Atlantic transports and their variability during 1958-2007, *Ocean Modelling*, *91*, 70–90.

Sloyan, B. M., and S. R. Rintoul (2001), The Southern Ocean limb of the global deep overturning circulation, *Journal of Physical Oceanography*, *31*, 143–173.

Smith, G. C., and K. Haines (2009), Evaluation of the S(T) assimilation method with the Argo dataset, *Quarterly Journal of the Royal Meteorological Society*, *135*, 739–756.

Smith, R. D. (2010), The parallel ocean program (pop) reference manual, ocean component of the community climate system model (ccsm), tech. rep. laur-10-01853, *Tech. rep.*, Los Alamos National Laboratory.

Soutelino, R. G., A. Gangopadhyay, and I. C. A. da Silveira (2013), The roles of vertical shear and topography on the eddy formation near the site of origin of the Brazil Current, *Continental Shelf Research*, *70*, 46–60.

Spadone, A., and C. Provost (2009), Variations in the Malvinas Current volume transport since 1992, *Journal of Geophysical Research*, *114*, doi:10.1029/2008JC004882.

Stepanov, V., and K. Haines (2014), Mechanisms for AMOC variability simulated by the NEMO model, *Ocean Science*, *10*, 645–656, doi:10.5194/os-10-645-2014.

Stepanov, V., K. Haines, and G. C. Smith (2012), Assimilation of Rapid Array data into an ocean model, *Quarterly Journal of the Royal Meteorological Society*, *138*, 2105–2117.

Stepanov, V., D. Iovino, S. Masina, A. Storto, and A. Cipollone (2016), The impact of horizontal resolution of density field on the calculation of the Atlantic meridional

overturning circulation at 34°S, *Journal of Geophysical Research: Oceans*, *121*, 4323–4340, doi:10.1002/2015JC011505.

Stommel, H. M. (1961), Thermohaline convection with two stable regimes of flow, *Tellus*, *13*, 224–230.

Storkey, D., E. W. Blockley, R. Furner, C. Guiavarc′h, D. Lea, M. J. Martin, R. M. Barciela, A. Hines, P. Hyder, and J. R. Siddorn (2010), Forecasting the ocean state using NEMO: The new FOAM system, *Journal of Operational Oceanography*, *3*, 3–15.

Storto, A., and S. Masina (2016), C-GLORSv5: an improved multipurpose global ocean eddy-permitting physical reanalysis, *Journal of Earth System Science*, *8*, 679–696.

Storto, A., S. Dobricic, S. Masina, and P. Di Pietro (2011), Assimilating along-track altimetric observations through local hydro static adjustments in a global ocean reanalysis system, *Monthly Weather Review*, *139*, 738–754.

Stouffer, R. J., J. Yin, J. Gregory, K. Dixon, M. Spelman, W. Hurlin, A. J. Weaver, M. Eby, G. M. Flato, H. Hasumi, A. Hu, H. Jungclaus, I. V. Kamenkovich, A. Levermann, A. Montoya, S. Murakami, S. Nawrath, A. Oka, W. R. Peltier, D. Y. Robitaille, A. Sokolov, G. Vettoretti, and S. L. Weber (2006), Investigating the causes of the response of the thermohaline circulation to past and future climate changes, *Journal of Climate*, *19*, 1365–1387, doi:10.1175/JCLI3689.1.

Stramma, L., and M. England (1999), On the water masses and mean circulation of the South Atlantic Ocean, *Journal of Geophysical Research: Oceans*, *104*, 863–883.

Stramma, L., and F. Schott (1999), The mean flow field of the tropical Atlantic Ocean, *Deep-Sea Research Part II*, *46*, 279–303.

Straneo, F. (2006), On the Connection between Dense Water Formation, Overturning,

and Poleward Heat Transport in a Convective Basin, *Journal of Physical Oceanography*, *36*, 1822–1840.

Sverdrup, H. U. (1947), Wind-Driven Currents in a Baroclinic Ocean; with Application to the Equatorial Currents of the Eastern Pacific, *Proceedings of the National Academy of Science*, *33*, 318–326.

Talley, L. D. (2003), Shallow, intermediate and deep overturning components of the global heat budget, *Journal of Physical Oceanography*, *33*, 530–560.

Taylor, K. E., R. J. Stouffer, and G. A. Meehl (2012), An overview of CMIP5 and the experiment design, *Bulletin of the American Meteorological Society*, *93*, 485–498, doi:110.1002/2015RG000493.

Timmermann, R., H. Goosse, G. Madec, T. Fichefet, C. Ethe, and V. Duliere (2005), On the representation of high latitude processes in the ORCA-LIM global coupled sea ice-ocean model, *Ocean Modelling*, *8*, 175–201.

Treguier, A. M., J. Deshayes, J. Le Sommer, C. Lique, G. Madec, T. Penduff, J.-M. Molines, B. Barnier, R. Bourdalle-Badie, and C. Talandier (2014), Meridional transport of salt in the global ocean from an eddy-resolving model, *Ocean Science*, *10*, 243–255.

Trenberth, K. E., and J. M. Caron (2001), Estimates of meridional atmosphere and ocean heat transports, *Journal of Climate*, *14*, 3433–3443.

Uotila, P., H. Goosse, K. Haines, M. Chevallier, A. Barthélemy, C. Bricaud, J. Carton, N. Fuckar, G. Garric, D. Iovino, F. Kauker, M. Korhonen, V. S. Lien, M. Marnela, F. Massonnet, D. Mignac, K. A. Peterson, R. Sadikni, L. Shi, S. Tietsche, T. Toyoad, X. J., and Z. Zhang (2019), An assessment of ten ocean reanalyses in the polar regions, *Climate Dynamics*, *52*, 1613–1650, doi:10.1007/s00382-018-4242-z.

Urbano, D. F., R. A. F. De Almeida, and P. Nobre (2008), Equatorial Undercurrent and North Equatorial Countercurrent at 38W: A new perspective from direct velocity data, *Journal of Geophysical Research*, *113*, doi:10.1029/2007JC004215.

Valdivieso, M., K. Haines, H. Zuo, and D. Lea (2014), Freshwater and heat transports from global ocean synthesis, *Journal of Geophysical Research: Oceans*, *119*, 394–409.

Vellinga, M., and R. Wood (2002), Global Climate Impacts of a Collapse of the Atlantic Thermohaline Circulation, *Climate Change*, *54*, 251–267.

Vivier, F., C. Provost, and M. Meredith (2001), Remote and local wind forcing in the Brazil/Malvinas region, *Journal of Physical Oceanography*, *31*, 892–913.

Voigt, A., B. Stevens, J. Bader, and T. Mauritsen (2013), The observed hemispheric symmetry in reflected shortwave irradiance, *Journal of Climate*, *26*, 468–477, doi: 10.1029/2018GL081328.

Warren, B. (1983), Why is no deep water formed in the North Pacific?, *Journal of Marine Research*, *41*, 327–347.

Waters, J., M. Bell, M. J. Martin, and D. J. Lea (2017), Reducing ocean model imbalances in the equatorial region caused by data assimilation, *Quarterly Journal of the Royal Meteorological Society*, *143*, 195–208, doi:10.1002/qj.2912.

Weijer, W., W. P. M. de Ruijter, A. Sterl, and S. S. Drijfhout (2002), Response of the Atlantic overturning circulation to South Atlantic sources of buoyancy, *Global and Planetary Change*, *34*, 293–311.

Wijffels, S. E., R. W. Schmitt, H. L. Bryden, and A. Stigebrandt (1992), Transport of freshwater by the oceans, *Journal of Physical Oceanography*, *22*, 155–162, doi: 10.1175/2009JPO4215.1.

Wolfe, C. L., and P. Cessi (2010), What sets the strength of the mid-depth stratifi-

cation and overturning circulation in eddying ocean models?, *Journal of Physical Oceanography*, *40*, 1520–1538.

Wunsch, C., and P. Heimbach (2013), Two decades of the Atlantic Meridional Overturning Circulation: Anatomy, variations, extremes, prediction, and overcoming its limitations, *Journal of Climate*, *26*, 7167–7186, doi:10.1175/JCLI-D-12-00478.1.

Xin, X. G., T. W. Wu, J. L. Li, Z. Wang, W. Li, and F. Wu (2013), How well does BCC-CSM1.1 reproduce the 20th century climate change over China, *Atmospheric and Oceanic Science Letters*, *1*, 21–26.

Yeager, S., and G. Danabasoglu (2014), The origins of late-twentieth-century variations in the large-scale North Atlantic circulation, *Journal of Climate*, *27*, 3222–3247, doi:10.1175/JCLI-D-13-00125.1.

Yin, J., and R. J. Stouffer (2007), Comparison of the stability of the Atlantic thermohaline circulation in two coupled atmosphere-ocean general circulation models, *Journal of Climate*, *20*, 4293–4315.

Zappa, G., L. C. Shaffrey, K. I. Hodges, P. G. Sansom, and D. B. Stephenson (2013), A Multimodel Assessment of Future Projections of North Atlantic and European Extratropical Cyclones in the CMIP5 Climate Models, *Journal of Climate*, *26*, 5846–5862.

Zhang, D., and M. J. McPhaden (2006), Decadal variability of the shallow Pacific meridional overturning circulation: Relation to tropical sea surface temperatures in observations and climate change models, *Ocean Modelling*, *15*, 250–273.

Zhang, D., M. J. McPhaden, and W. E. Johns (2003), Observational evidence for flow between the subtropical and tropical Atlantic: The Atlantic tropical cells, *Journal of Physical Oceanography*, *33*, 1783–1797.

Zhang, D., R. Msadek, J. Michael, M. J. McPhaden, and T. Delworth (2011), Multidecadal variability of the North Brazil Current and its connection to the Atlantic meridional overturning circulation, *Journal of Geophysical Research*, *116*, doi:10.1029/2010JC006812.

Zhang, R. (2010), Latitudinal dependence of Atlantic Meridional Overturning Circulation (AMOC) variations, *Geophysical Research Letters*, *37*, doi:10.1029/2010GL044474.

Zhang, R., and T. L. Delworth (2005), Simulated tropical response to a substantial weakening of the Atlantic thermohaline circulation, *Journal of Climate*, *18*, 1853–1860.

Zhu, C., Z. Liu, and S. Gu (2018), Model bias for South Atlantic Antarctic intermediate water in CMIP5, *Climate Dynamics*, *50*, 3613–3624.

Zika, J., N. Skliris, A. T. Blaker, R. Marsh, A. J. G. Nurser, and S. A. Josey (2018), Improved estimates of water cycle change from ocean salinity: The key role of ocean warming, *Environmental Research Letters*, *13*.

Zuo, H., R. I. Mugford, K. Haines, and G. C. Smith (2011), Assimilation impacts on Arctic Ocean circulation, heat and freshwater, *Ocean Modelling*, *40*, 147–163, doi:10.1016/j.ocemod.2011.08.008.

Zuo, H., M. A. Balmaseda, and K. Mogensen (2015), The new eddy-permitting ORAP5 ocean reanalysis: description, evaluation and uncertainties in climate signals, *Climate Dynamics*, *49*, 791–811, doi:10.1007/s00382-015-2675-1.